
INTERACTION OF
LIGHT WITH IMPURITIES IN
LITHIUM NIOBATE CRYSTALS

Dissertation

zur
Erlangung des Doktorgrades (Dr. rer. nat.)
der
Mathematisch-Naturwissenschaftlichen Fakultät
der
Rheinischen Friedrich-Wilhelms-Universität Bonn

vorgelegt von
Judith Renate Marie-Luise Schwesyg
aus
Rheinfelden

Bonn 2011

Angefertigt mit Genehmigung der Mathematisch-Naturwissenschaftlichen Fakultät
der Rheinischen Friedrich-Wilhelms-Universität Bonn

1. Gutachter: Prof. Dr. Karsten Buse
2. Gutachter: Prof. Dr. Karl Maier

Tag der Promotion: 06.06.2011
Erscheinungsjahr: 2011

Contents

Abstract	v
1 Introduction	1
2 Fundamentals	3
2.1 Interaction of light with matter	3
2.1.1 Optical absorption	4
2.1.2 Nonlinear-optical processes	5
2.2 Lithium niobate crystals	8
2.2.1 Crystal growth and stoichiometry	9
2.2.2 Intrinsic defects - lattice defects and polarons	10
2.2.3 Extrinsic defects – impurities and dopants	12
2.2.4 Overview – Optical transitions	15
2.3 Implications of optical absorption – Light-induced refractive index changes .	17
2.3.1 Photorefractive effect in bulk-photovoltaic media	17
2.3.2 Thermo-optic effect and thermal lensing	20
2.4 Thesis overview	22
3 Absorption in congruent LiNbO_3 and $\text{LiNbO}_3\text{:MgO}$ between 350 and 2000 nm	23
3.1 Methods	24
3.2 Crystals	26
3.2.1 Undoped congruent LiNbO_3 crystals	26

3.2.2	MgO-doped LiNbO ₃ crystals	28
3.2.3	LiNbO ₃ :MgO crystals codoped with a transition metal	29
3.3	Results and discussion: Congruent LiNbO ₃ crystals	31
3.3.1	Results	31
3.3.2	Discussion	35
3.4	Results and discussion: MgO-doped LiNbO ₃ crystals	39
3.4.1	Results	39
3.4.2	Discussion	46
3.5	Comparison: Congruent LiNbO ₃ vs. MgO-doped LiNbO ₃	49
3.6	Outlook and conclusion	50
4	Suppression of mid-IR absorption in congruent LiNbO₃ and LiNbO₃:MgO	53
4.1	Crystals and measurement method	55
4.1.1	Crystals	55
4.1.2	Measurement method	56
4.2	Experimental results	57
4.2.1	Infrared absorption spectra of MgO-doped LiNbO ₃ crystals	57
4.2.2	Infrared absorption spectra of congruent LiNbO ₃ crystals	60
4.3	Discussion	63
4.4	First OPO experiments – Operation of a 1550-nm-pumped singly-resonant continuous-wave OPO	66
4.5	Outlook and conclusion	67
5	Pyroelectrically-induced photorefractive damage in LiNbO₃:MgO	69
5.1	Introduction	69
5.1.1	Photorefractive damage due to an externally applied electric field	70
5.1.2	Pyroelectrically-induced photorefractive damage	71
5.2	Theory	72
5.2.1	Steady-state photorefractive effect – one-dimensional case	72
5.2.2	Time-dependence of pyroelectrically-induced photorefractive damage – one-dimensional case	73

5.2.3	Time-dependence of pyroelectrically-induced photorefractive damage – two-dimensional case	75
5.2.4	Impact on applications	77
5.3	Experimental setups and results	86
5.3.1	Beam distortion	86
5.3.2	Interferometry	89
5.3.3	Determination of the specific photoconductivity and the bulk- photovoltaic coefficient	94
5.4	Discussion	99
5.5	Outlook and conclusion	101
6	Summary	103
	Bibliography	105

Abstract

Congruent lithium niobate (LiNbO_3) and 5-mol% MgO-doped LiNbO_3 (MgO:LN) crystals are widely used as nonlinear-optical crystals in frequency-conversion devices due to their large nonlinear-optic coefficients. These devices usually require high optical pump powers, but absorption of photons by impurities limits their usability due to heat accumulation that leads to thermo-optic refractive index changes. These refractive index changes distort the beam shape and disturb the phase-matching condition. Furthermore pyroelectric fields can build up.

In this thesis the residual optical absorption in congruent LiNbO_3 (CLN) and MgO:LN crystals is studied. Absorption spectra of CLN and MgO:LN crystals between 400 – 2000 nm reveal a residual absorption up to 0.04 cm^{-1} . This absorption is mainly caused by transition metal impurities. Between 2300 – 2800 nm unknown hydrogen absorption bands in CLN and MgO:LN are revealed on the order of 0.001 cm^{-1} . High-temperature annealing is applied to the CLN and MgO:LN crystals, which decreases optical absorption by up to one order of magnitude. As an application, the operation of a 1550-nm pumped singly-resonant CW optical parametric oscillator, resonant around 2600 nm, using a low-loss, periodically-poled, annealed CLN crystal is demonstrated.

Another issue that affects CLN is photorefractive damage (PRD), i.e. light-induced refractive index changes. In contrast, MgO:LN crystals do not suffer from PRD even at high optical intensities. However, it is shown in this thesis that PRD can occur within seconds in MgO:LN, using green laser light at light intensity levels as low as 100 mW/cm^2 , if the crystal is heated by several degrees Celsius during or before illumination. Photorefractive damage does not occur in CLN crystals under the same conditions. We show that the pyroelectric effect together with an elevated photoconductivity compared to that of CLN causes this beam distortion and that this effect also influences frequency conversion experiments in the infrared due to beam self-heating.

ABSTRACT

Chapter 1

Introduction

The sun is a source of an enormous amount of energy. Life on earth would not be possible without using this energy source. The physical mechanism that enables the use of this energy source is photon absorption, also often referred to as optical absorption. Photon absorption can be found almost everywhere in nature, science and technology. For instance, photon absorption by the earth's surface and atmosphere enables the conversion of solar energy into heat [1]. A prominent example, in which solar energy is converted into chemical energy, is photosynthesis, i.e. organisms synthesize organic chemical compounds, most importantly carbohydrates such as glucose (sugar), from mainly carbon dioxide and water with the help of absorbed light [2, 3]. An important field in science and technology, which is based on photon absorption, is the field of photovoltaics, i.e. conversion of solar energy into electrical energy [4].

However, there are also fields in science and technology where photon absorption is detrimental, e.g. in high-power laser applications. One of the most exciting very recent experiments where optical absorption can be a serious obstacle is conducted at the National Ignition Facility (NIF) at the Lawrence Livermore National Laboratory, USA. In the experiment 192 laser beams at the wavelength 351 nm are focused to a single spot with a total energy of about 1.8 MJ to initiate nuclear fusion of a deuterium-tritium pellet [5]. Due to the enormous laser power the optical components have to exhibit very low optical absorption, but residual absorption, which is mostly caused by impurity centers [5, 6], is still present. Hence cool-down times between subsequent laser pulses are about eight hours so far, the aim is to fire one pulse every four hours [7]. One important step on this path is to gain control over the absorption in every optical component in the beam lines.

This shows that with the development of more powerful lasers photon absorption also becomes more important. This can especially be seen in the field of nonlinear optics where optical absorption limits the performance of devices. One of the most promis-

ing nonlinear-optical materials are lithium niobate crystals (LiNbO_3) doped with 5 mol% magnesium oxide (MgO). These 5-mol% MgO-doped LiNbO_3 (MgO:LN) crystals are robust and relatively inexpensive, and they exhibit various technologically relevant physical properties, e.g. they are ferroelectric, electro-optic, and they have high nonlinear-optical coefficients [8–10]. Because of these outstanding properties MgO:LN crystals are widely used for high-power frequency conversion applications, e.g. frequency-doubling into the blue-green spectral range in the 1 – 5 W output power regime has been reported [11, 12]. However, for higher laser powers optical absorption limits the achievable output power, e.g. absorption leads to heat accumulation and thus changes the refractive index, limiting the conversion efficiency of frequency-conversion devices [13, 14]. As laser technology advances, more powerful pump-laser systems are developed, e.g. there exist pump lasers at 1123 nm emitting continuous-wave optical powers of more than 100 W [15]. MgO:LN crystals, however, cannot be used with such high-power lasers. If the residual optical absorption is reduced, MgO:LN may become the material of choice for future high-power nonlinear-optical applications, not only because of its outstanding physical properties, but also because of its commercial availability, low cost, high quality, robustness, and long-term stability, which is important for industrial applications.

So far little is known about the origin of optical absorption in MgO:LN crystals, e.g. it is unknown if the optical absorption is dominated by photon-absorbing impurities, so-called extrinsic defects, or if the absorption is caused by intrinsic defects. In this dissertation optical absorption centers in MgO:LN are identified. Additionally, optical absorption in undoped congruent LiNbO_3 , which is an important material for nonlinear-optical applications in the infrared spectral range, is also studied. Furthermore it is explored how optical absorption can be reduced by post-growth processing. Finally it is investigated theoretically and experimentally under which experimental conditions unwanted light-induced refractive index changes can occur in MgO:LN although this material is commonly believed not to suffer from such effects.

Chapter 2

Fundamentals

2.1 Interaction of light with matter

The major focus of this work is on the interaction of light with LiNbO₃ crystals. Hence, in this chapter a short introduction to interaction of light with matter with special focus on nonlinear optics is given followed by a detailed overview over the physical properties and characteristics of LiNbO₃, one of the most prominent nonlinear-optical crystals.

The analysis for any interaction of light with matter is based on Maxwell's equations [16]:

$$\nabla \cdot \mathbf{D} = \rho \quad (2.1)$$

$$\nabla \cdot \mathbf{B} = 0 \quad (2.2)$$

$$\nabla \times \mathbf{E} = -\frac{\partial \mathbf{B}}{\partial t} \quad (2.3)$$

$$\nabla \times \mathbf{H} = \mathbf{j} + \frac{\partial \mathbf{D}}{\partial t}, \quad (2.4)$$

where \mathbf{E} and \mathbf{B} are the electric and magnetic fields and \mathbf{D} and \mathbf{H} are the electric displacement and the auxiliary magnetic fields. Furthermore, ρ and \mathbf{j} are the charge and current density respectively, and t is the time. Furthermore the material equations are described by

$$\mathbf{D} = \epsilon_0 \mathbf{E} + \mathbf{P} \quad (2.5)$$

$$\mathbf{B} = \mu_0 \mathbf{H} + \mathbf{M}, \quad (2.6)$$

where \mathbf{P} and \mathbf{M} are the electric polarization and magnetization densities and ϵ_0 and μ_0 are the vacuum permittivity and vacuum permeability. Furthermore, it is

$$\mathbf{P} = \epsilon_0 \hat{\chi} \mathbf{E}, \quad (2.7)$$

where $\hat{\chi}$ is the electric susceptibility tensor (second-rank tensor). The dielectric tensor $\hat{\epsilon}$, which also is a second-rank tensor, is given by $\hat{\epsilon} = 1 + \hat{\chi}$, hence, with Eq. 2.9, it is $\mathbf{D} = \epsilon_0 \epsilon \mathbf{E}$ for isotropic media.

Any interaction of light with matter in classical electrodynamics can be described as a solution of Maxwell's equations.

2.1.1 Optical absorption

Optical absorption can be observed when a light beam of initial light intensity I_0 is transmitted through a medium of length L and the intensity I of the transmitted beam is measured. If the energy of a photon is taken up by the material, e.g. electrons, the light intensity I after the medium will be smaller than the initial light intensity I_0 , i.e. light is "absorbed" by the medium. Thus a measure for optical absorption is the transmission $T = I/I_0$. Another important measure is the optical density OD (also often called absorbance) which is defined as

$$OD = \log_{10} \frac{I_0}{I} = \log_{10} \frac{1}{T} . \quad (2.8)$$

The attenuation of the intensity of a plane light wave propagating in z -direction inside an optical material can be described by

$$dI(\lambda) = c_x \sigma^{\text{abs}}(\lambda) I(\lambda) dz , \quad (2.9)$$

where dz is the infinitesimal increment in z -direction, λ is the wavelength, c_x is the concentration of the absorbing species X , and $\sigma^{\text{abs}}(\lambda)$ is the absorption cross section [17]. Consider an optical plate of thickness L . Then the light intensity of the beam after passing the plate is

$$I(\lambda, L) = I_0 \exp \left(-c_x \sigma^{\text{abs}}(\lambda) L \right) . \quad (2.10)$$

The absorption coefficient $\alpha(\lambda)$ is defined as

$$\alpha(\lambda) = c_x \sigma^{\text{abs}}(\lambda) . \quad (2.11)$$

Thus Eq. 2.9 can be simplified to

$$I(\lambda, L) = I_0 \exp (-\alpha(\lambda) L) . \quad (2.12)$$

The absorption coefficient α is an accurate measure for describing intensity losses due to optical absorption and light scattering, e.g. at refractive index inhomogeneities. In most technologically useful optical media scattering can be neglected due to high material quality, hence α is a measure for optical absorption. The absorption coefficient α

can be derived from the measured transmission T and the Fresnel reflection coefficient $R = [n(\lambda) - 1]^2/[n(\lambda) + 1]^2$ where $n(\lambda)$ is the refractive index of the material [18]:

$$\alpha = -\frac{1}{L} \ln \left(-b + \sqrt{b^2 + \frac{1}{R^2}} \right) \text{ with } b = \frac{(1 - R)^2}{2TR^2} . \quad (2.13)$$

Note that the dispersion relation $n(\lambda)$ is given by the Sellmeier equation which is an empirical relationship describing the dispersion relation for a particular transparent medium [17]. If an optical material is anisotropic the phase velocity v of light traveling through this material, and thus the refractive index n , becomes polarization and direction dependent. This phenomenon is called birefringence. Note that in uniaxial, birefringent materials there is a direction in which a transmitted light beam does not experience birefringence, this direction is called optic axis. In the following we will focus on the special case that the beam is entering the crystal perpendicular to the crystal surface, and the optic axis is also perpendicular to the beam. Due to the perpendicular incidence there is no beam splitting or walk-off, however the phase velocity, i.e. the refractive index, depends on the light polarization: The refractive index for light that is polarized perpendicular to the optic axis (o -wave light) is the ordinary refractive index n_o , the refractive index for light that is polarized in parallel with the optic axis (e -wave light) is the extraordinary refractive index. Thus, in order to determine the absorption coefficient in an uniaxial crystal from transmission data (Eq. 2.13), the Fresnel correction has to take light polarization into account.

2.1.2 Nonlinear-optical processes

In the simplest case the dependence between polarization \mathbf{P} and electric field \mathbf{E} in dielectric media is linear (Eq. 2.7), however in nonlinear dielectric media \mathbf{P} depends nonlinearly on \mathbf{E} [19], i.e.

$$P(E) = \epsilon_0 \left(\chi^{(1)} E + \chi^{(2)} E^2 + \chi^{(3)} E^3 + \dots \right) = P^{(1)} + P^{\text{NL}} , \quad (2.14)$$

where $\chi^{(1)}$ is the linear susceptibility, $\chi^{(2)}$, $\chi^{(3)}$,... are higher-order susceptibilities, and P^{NL} is the nonlinear polarization. For simplicity we have taken \mathbf{P} , \mathbf{E} , and the tensors $\hat{\chi}^{(1)}$, $\hat{\chi}^{(2)}$,... to be scalar quantities. Note that, in the cases where the frequencies of the optical waves are much lower than the lowest resonance frequency of the material, $\hat{\chi}$ is weakly frequency dependent and often the notation $2d_{ijk} = \chi_{ijk}^{(2)}$ is used, where d_{ijk} is called nonlinear-optical coefficient [19]. Details about how to treat the vector nature of P and E can be found in [19].

In order to understand the nonlinear effects, assume a laser beam whose electric field is given by

$$E(t) = E_0 e^{i\omega t} + \text{c.c.} , \quad (2.15)$$

where E_0 is the field amplitude, ω is the frequency, and t is the time. Combining Eq. 2.15 with Eq. 2.14 one obtains

$$P(t) = \epsilon_0 \left(\chi^{(1)} E_0 e^{i\omega t} + \chi^{(2)} E_0^2 e^{2i\omega t} + \dots \right) . \quad (2.16)$$

As can be seen from Eq. 2.16 there is a term with frequency 2ω . This term is responsible for the generation of light with frequency 2ω . This process is called "second-harmonic generation" (SHG) or frequency doubling. However, due to dispersion, the fundamental wave and the newly generated wave travel with different velocities. That causes destructive interference of the frequency-doubled light generated at different crystal positions. The distance over which the phase-mismatch between the two waves becomes π is called the "coherence length" l_C . Thus efficient energy transfer to the frequency-doubled light wave is only possible if the nonlinear oscillations of all dipoles in the material are properly phase matched. Other nonlinear-optical processes than SHG are also feasible, e.g. in the case the incident optical field consists of two frequencies ω_1 and ω_2 , the nonlinear polarization contains frequency components $2\omega_{1,2}$, $\omega_1 \pm \omega_2$, and a DC term. The corresponding frequency-conversion processes are second harmonic generation, sum and difference frequency mixing, and optical rectification respectively.

An often used process is "optical parametric oscillation": A nonlinear optical crystal pumped with light of frequency ω_p is placed in an optical resonator with, e.g. high reflectivity mirrors for light with frequency ω_s , the signal wave [19]. If $\omega_s < \omega_p$ a so-called "idler field" with frequency $\omega_i = \omega_p - \omega_s$ is generated and coupled out of the resonator, and the resonating signal wave ω_s builds up to high amplitude inside the resonator. Such a setup is called "optical parametric oscillator" (OPO). The major advantage of OPOs is their tunability over a wide frequency range, because for any frequency $\omega_s < \omega_p$ meeting the resonance condition a frequency ω_i can be found obeying $\omega_p = \omega_s + \omega_i$. Note also that, as is the case for SHG, or any other nonlinear frequency-generation process, phase matching has to be maintained for efficient parametric amplification and oscillation. In Fig. 2.1 the processes of SHG and OPO are shown schematically.

Quasi-phase-matching There are several phase-matching techniques, e.g. birefringent phase matching [19] uses the birefringence of the nonlinear-optical material to obtain equal refractive indices for different light polarizations and different frequencies, however limited tuning capabilities make birefringent phase matching challenging. Another possibility is so-called "quasi-phase-matching" (QPM) [20, 21] for which ferroelectric media often are employed. This process is less effective, but independent of birefringence. In the following quasi-phase-matching is explained for the case of SHG as an example:

Ferroelectric media possess a permanent spontaneous polarization \mathbf{P}_S whose direction can be flipped by application of an external electric field. This process is called "electric-field

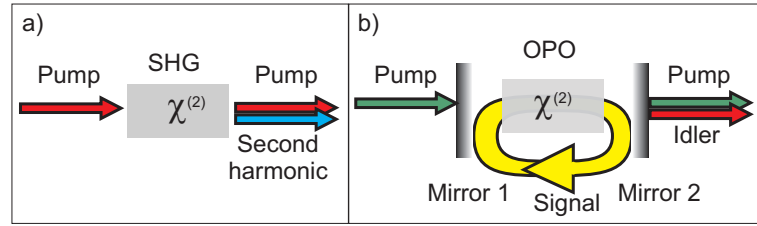


Figure 2.1: a) Schematic of second harmonic generation and b) signal-resonant optical parametric oscillation in a linear cavity. Mirror 1 is highly-transmissive (HT) for the pump wave and highly reflective (HR) for the signal wave, mirror 2 is HR for the signal wave and HT for the signal and idler waves; $\chi^{(2)}$ denotes the nonlinear-optical material.

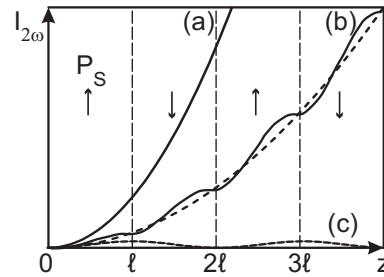


Figure 2.2: Schematic diagram for phase matching in the case of SHG (redrawn from [21]). Intensity $I_{2\omega}$ of the frequency-doubled light vs. light propagation distance z inside the crystal. The drawn periodic inversion of the spontaneous polarization P_S for every coherence length ℓ only applies for graph (b). Graph (a) shows perfect phase matching. Graph (b) shows the case of quasi-phase matching and (c) the case of no phase matching.

poling" [22]. The term ferroelectricity is used in analogy to ferromagnetism in materials which have a permanent magnetic moment. The region where \mathbf{P}_S is constant is called "domain". Let us assume that a pump laser beam is transmitted through a periodically poled crystal in which the domain width is chosen to be one coherence length ℓ and the direction of \mathbf{P}_S changes by 180° for every domain, then a phase-shift of π is induced every coherence length ℓ . Hence the phase mismatch between the fundamental and the SHG wave is reset to 0 every coherence length l_C of light propagation and destructive interference of SHG light generated at different positions in the crystal can be avoided. Constructive interference helps to build up intensity of generated light over distances much longer than the coherence length. Note that the periodic domain flip is called "periodic poling". The efficiencies of birefringent phase matching and QPM are schematically depicted in Fig. 2.2. In the following, lithium niobate, one of the most prominent nonlinear-optical, ferroelectric materials suited for QPM, is introduced.

2.2 Lithium niobate crystals

Lithium niobate (LiNbO_3 , LN) belongs to the group of ABO_3 -type ferroelectrics. Due to its ferroelectricity, LiNbO_3 is a non-centrosymmetric crystal below the Curie temperature $T_C = 1165\text{ }^\circ\text{C}$ [23,24]. The crystal structure is depicted in Fig. 2.3 [25].

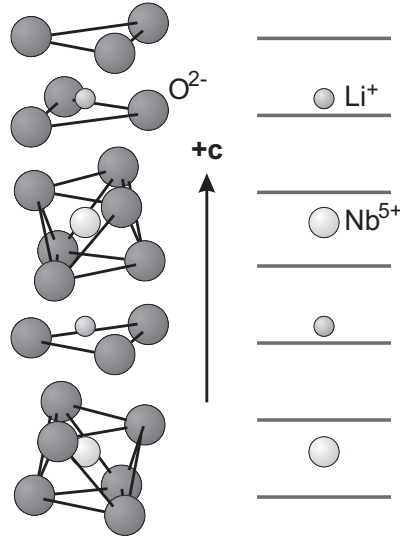


Figure 2.3: *Crystal structure of LiNbO_3 redrawn from [25].*

Below T_C the orientation of the crystal's \mathbf{c} -axis is given by the position of the lithium (Li) and niobium (Nb) cations and the empty sites between the oxygen atom planes. The alternation of cation sites may be schematically depicted as a chain $\dots\text{Li-Nb-}\diamond\text{-Li-Nb-}\diamond\dots$, where \diamond denotes the empty octahedron [24]. This leads to the spontaneous polarization \mathbf{P}_S of the crystal with $\mathbf{P}_S = 10\text{ }\mu\text{C}/\text{cm}^2$ at room temperature.

Lithium niobate belongs to the rhombohedral (trigonal) space group $R3c$ with point group $3m$, which means it is an uniaxial crystal with the crystallographic \mathbf{c} -axis being the 3-fold rotational symmetric axis. Any turn by 120° around this axis leads to an identical image [25]. This is different from crystals with the perovskite structure, which is face-centered cubic.

Due to their non-centrosymmetric crystal structure LiNbO_3 crystals possess several outstanding crystal properties. LiNbO_3 crystals are not only ferroelectric, but also piezoelectric and birefringent. Furthermore, LiNbO_3 possesses high nonlinear-optical coefficients [26,27], and due to the fact that \mathbf{P}_S in LiNbO_3 can be changed by applying an elec-

tric field, LiNbO_3 can be periodically poled so that it can be used for QPM devices [28,29]. Periodically poled LiNbO_3 will be denoted PPLN in the further chapters.

Pyroelectricity Due to their ferroelectricity, LiNbO_3 crystals also exhibit pyroelectricity. The pyroelectric effect is the change in spontaneous polarization \mathbf{P}_S of the crystal resulting from a change in temperature T . The pyroelectric coefficient p_3 for LiNbO_3 at room temperature is [30]

$$p_3 = \left(\frac{d\mathbf{P}_S}{dT} \right)_z = -6.4 \times 10^{-5} \text{ CK}^{-1}\text{m}^{-2}, \quad (2.17)$$

where $(d\mathbf{P}_S/dT)_z$ denotes the z -component.

2.2.1 Crystal growth and stoichiometry

There are several LiNbO_3 growth techniques, e.g. Bridgman, Verneuil, flux methods, etc., but the most widely used industrial growth method is the Czochralski growth method [31]. First, the starting material for the melt is prepared: Lithium carbonate (Li_2CO_3) and niobium pentoxide (Nb_2O_5) powders are mixed, and the powder mixture is annealed at $700 - 800$ °C for up to 12 hours in order to dry and calcinate the carbonate. Then a sintering process follows at about 1050 °C for 2-4 hours and, back at room temperature, the sintered mixture is ground [32]. The powder is then melted in a platinum crucible. A rotating crystal seed is lowered into the melt until a tip of the seed touches the melt. The melt temperature is slightly above the melting point, thus crystal growth starts when the seed rod is slowly pulled out of the melt. The new crystal grows on the crystal seed and along the crystallographic axes provided by the seed. The diameter of the growing crystal boule is influenced by the crucible temperature, e.g. the closer the temperature of the crucible is to the melting point of LiNbO_3 , the faster crystallization becomes. The melt composition must be controlled very precisely. Control of impurities, thermal gradients, exact weighing of the powders, and control of moisture by drying of the starting powders and many other parameters are crucial for obtaining high quality crystals [8]. The melt fraction converted into crystal material, that is typically used for high optical quality and compositional homogeneity, is 50 %.

Lithium niobate is usually grown in ambient air, hence no special atmosphere is needed. In order to grow homogeneous LiNbO_3 crystals the ideal melt composition is at the congruency point which means that the crystal has the same composition as the liquid melt. The phase diagram for LiNbO_3 is depicted in Fig. 2.4. A congruently melting LiNbO_3 crystal (CLN crystal) is grown if the corresponding oxide concentrations are $c_{\text{Li}_2\text{O}}/(c_{\text{Li}_2\text{O}} + c_{\text{Nb}_2\text{O}_5}) = 48.34$ mol% and $c_{\text{Nb}_2\text{O}_5}/(c_{\text{Li}_2\text{O}} + c_{\text{Nb}_2\text{O}_5}) = 51.66$ mol% and

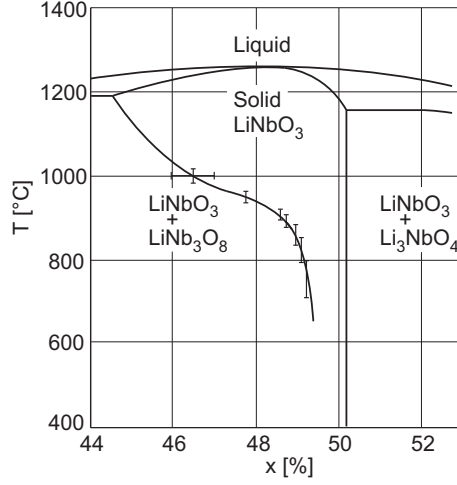


Figure 2.4: Phase diagram of $\text{Li}_2\text{O}-\text{Nb}_2\text{O}_5$ near the congruent and stoichiometric composition of LiNbO_3 . The variable x denotes the ratio $c_{\text{Li}}/(c_{\text{Li}} + c_{\text{Nb}})$ where c_{Li} is the concentration of Li ions and c_{Nb} is the concentration of Nb ions [24].

$c_{\text{Li}}/c_{\text{Nb}} = 0.94$ [24]. This composition is where the liquidus and solidus curves intersect with each other in Fig. 2.4. Stoichiometric LiNbO_3 crystals (SLN), i.e. oxide concentrations are $c_{\text{Li}_2\text{O}}/(c_{\text{Li}_2\text{O}} + c_{\text{Nb}_2\text{O}_5}) = c_{\text{LiNb}_2\text{O}_5}/(c_{\text{Li}_2\text{O}} + c_{\text{Nb}_2\text{O}_5}) = 50 \text{ mol}\%$, are complicated to grow because they melt incongruently like many complex oxides. Even though it is possible to obtain near-stoichiometric LiNbO_3 , either by special growth techniques such as the double-crucible Czochralski method or post-growth processes such as vapor transport equilibration (VTE), commercial CLN crystals still exhibit the best optical quality among all compositions of LiNbO_3 so far [24], although the non-stoichiometry implies a high density of intrinsic crystal defects.

2.2.2 Intrinsic defects - lattice defects and polarons

CLN crystals contain about 6 mol% empty Li sites (V_{Li}) because $c_{\text{Li}}/c_{\text{Nb}} = 0.94$. The non-stoichiometry of CLN causes several different types of intrinsic defects which strongly influence the optical properties of the crystal. Hence understanding the defect structure is crucial. The most important types of intrinsic defects and their absorption bands are listed in Tab. 2.1 and explained in the following.

Empty Li and Nb sites There are empty Li (V_{Li}) and Nb (V_{Nb}) sites. These empty sites do not cause absorption bands, however the closer a LiNbO_3 crystal comes to stoi-

Polaron	$\tilde{\nu}_0$ (cm^{-1})	Wavelength λ_0 (nm)	Lifetime/comment	Reference
$\text{Nb}_{\text{Li}}^{4+}$	12900 ± 3200	775	μs	[33, 34]
$\text{Nb}_{\text{Nb}}^{4+}$	8050 ± 3000	1240	μs - ms in reduced LiNbO_3	[34–36]
$\text{Nb}_{\text{Li}}^{4+}$ - $\text{Nb}_{\text{Nb}}^{4+}$	20140 ± 4400	490	stable in reduced LiNbO_3	[24, 34]
O^-	20000	500	metastable, induced by e.g. X-ray irradiation	[36, 37]

Table 2.1: *Polarons in CLN and their absorption peaks. Given are the centers $\tilde{\nu}_0$ (wavelength λ_0) and the half-width-at-half-maximum (HWHM) values (where available) of the absorption peaks.*

chiometry, the more the fundamental absorption edge is shifted to shorter wavelengths [18].

Small bound polaron Since there is an excess of Nb atoms, and Nb^{5+} ions have a similar radius as Li^+ ions, Nb ions partially fill empty Li sites. This is called a "Nb antisite defect" (Nb_{Li}). Four lithium vacancies V_{Li} in the vicinity of a Nb_{Li} antisite defect compensate the excess charges in order to keep charge neutrality. When an electron is trapped at a $\text{Nb}_{\text{Li}}^{5+}$ antisite, the crystal lattice is locally distorted. Thus the electron is bound to that site. An intrinsic defect, a so-called "small bound polaron", forms which is denoted with $\text{Nb}_{\text{Li}}^{4+}$ [33, 34]. These small bound polarons absorb light with the corresponding absorption peak centered at $\tilde{\nu}_0 = 12900 \text{ cm}^{-1}$ and a half-width-at-half-maximum (HWHM) value of 3200 cm^{-1} . In this case the absorption of photons is attributed to an intervalence transition from $\text{Nb}_{\text{Li}}^{4+}$ to $\text{Nb}_{\text{Nb}}^{5+}$, i.e. from a localized level to the conduction band [34].

Small free polaron Electrons can also be self-trapped at the regular $\text{Nb}_{\text{Nb}}^{5+}$ sites and form another type of polaron, a so-called "small free polaron" $\text{Nb}_{\text{Nb}}^{4+}$ [34, 35]. They absorb light in a broad absorption band at $8050 \pm 3000 \text{ cm}^{-1}$. Both, the bound and small free polarons are unstable at room temperature. Hence they are usually barely populated. However, they can be populated if enough electrons are provided. This situation can either be obtained by reduction treatments or optical excitation, e.g. pulsed laser or UV illumination, that excites electrons from extrinsic defects or the valence band to the conduction band. The typical lifetime of small polarons is on the order of microseconds in strongly reduced crystals.

Bound bipolaron Another possibility is that $\text{Nb}_{\text{Li}}^{5+}$ - $\text{Nb}_{\text{Nb}}^{5+}$ nearest neighbor pairs bind two electrons forming a bound bipolaron $\text{Nb}_{\text{Li}}^{4+}$ - $\text{Nb}_{\text{Nb}}^{4+}$ [34, 38]. These bound bipolarons are stable at room temperature in reduced LiNbO_3 crystals and can be dissociated thermally or optically by absorbing light in a broad absorption band at $20140 \pm 4400 \text{ cm}^{-1}$. Optical dissociation of the bipolaron creates a $\text{Nb}_{\text{Li}}^{4+}$ polaron and a $\text{Nb}_{\text{Nb}}^{4+}$ polaron of which the latter is easily ionized and the electron is rapidly trapped by a further empty $\text{Nb}_{\text{Li}}^{5+}$ defect, thus the bipolaron is dissociated into two bound small polarons $\text{Nb}_{\text{Li}}^{4+}$ which then again absorb light at 12900 cm^{-1} [24].

Small bound hole polaron In the case of illumination with high photon energy such as ultraviolet (UV) or X-ray irradiation direct excitation of an electron from the valence band (VB) to the conduction band (CB) is possible which leaves a hole in the VB. In this case the hole can be captured by an O^{2-} ion in the vicinity of an empty Li site thus forming a stable O^- small bound hole polaron [37]. This type of polaron absorbs light at 20000 cm^{-1} in a very broad absorption band [36].

2.2.3 Extrinsic defects – impurities and dopants

There are many vacant Li and also some Nb sites in the crystal lattice of CLN where impurity ions can be incorporated instead. These defects are extrinsic, and the impurity ions might occupy either of three available octahedra sites (Li, Nb, and empty octahedron) or even interstitial sites. However, although the ionic radii of Nb^{5+} and Li^+ are similar, most impurities prefer empty Li sites independent of their charge [24]. The distribution of an impurity within a crystal is mathematically described by the so-called "effective distribution coefficient" k_{eff} [8]:

$$c_{\text{S}}/c_{\text{M}} = k_{\text{eff}} \left[(1 - g)^{k_{\text{eff}}} \right]^{-1}, \quad (2.18)$$

where g is the solidification fraction, and c_{S} and c_{M} are the impurity concentrations in the crystal and in the melt respectively.

2.2.3.1 Transition metal impurities

Typical extrinsic defects in LiNbO_3 crystals are transition metal (TM) impurity ions [39–41] such as iron (Fe), copper (Cu), chromium (Cr), manganese (Mn), and Nickel (Ni). From intentionally doped LiNbO_3 crystals it is known that all these impurities show strong optical absorption bands from the UV up to the near-infrared wavelength range. A summary of known transition metal impurities of LiNbO_3 and the spectral positions (center) of their optical absorption bands is given in Tab. 2.2.

Ion	$\tilde{\nu}_0$ (cm ⁻¹)	$\tilde{\nu}_0$ (cm ⁻¹)	Transition	References
	<i>o</i> -wave	<i>e</i> -wave		
Cr ³⁺	13820	13780	${}^4A_2 - {}^2E$ (spin-forbidden)	[42–44]
	15330	15300	${}^4A_2 - {}^4T_2$	[42–44]
	20850	21390	${}^4A_2 - {}^4T_1$	[42–44]
Fe ²⁺	8860	N/A	${}^5T_2 - {}^5E$	[10, 45]
	20970	21510	Fe ²⁺ –Nb ⁵⁺ intervalence transfer	[10, 45, 46]
Fe ³⁺	20570	N/A	<i>d</i> – <i>d</i> (spin-forbidden transition)	[10, 45, 46]
Ni ²⁺	7970	7810	${}^3A_2({}^3F) - {}^3T_2({}^3F)$	[47]
	13330	13900	${}^3A_2({}^3F) - {}^3T_1({}^3F)$	[47]
	20410	19420	${}^3A_2({}^3F) - {}^1T_2({}^1D)$	[47]
	23360	21980	${}^3A_2({}^3F) - {}^3T_1({}^3P)$	[47]
Cu ²⁺	10070	10020	${}^3E - {}^3T_2$	[45, 48, 49]
Cu ⁺	26670	26300	Cu ⁺ –Nb ⁵⁺ intervalence transfer	[45, 48, 49]
Mn ³⁺ or Mn ⁴⁺	17330	18180	${}^5E - {}^5T_2$	[50]

Table 2.2: Spectral positions of known absorption bands of intentionally doped LiNbO₃ crystals for *o*-wave and *e*-wave polarization.

As can be seen from Tab. 2.2 some transition-metal impurities can be incorporated in different valence states, e.g. Fe can be incorporated as Fe²⁺ or Fe³⁺ and Cu as Cu⁺ or Cu²⁺. In the case of Mn it is still under discussion in which valence states Mn is incorporated into LiNbO₃, most likely they are Mn³⁺ and Mn⁴⁺ [50]. The multivalence impurities can be oxidized or reduced by special post-growth high-temperature annealing that adds or removes electrons from the crystal as is known from electrochemistry, e.g. Fe²⁺ → Fe³⁺ + e⁻ denotes an oxidization process [45, 51]. In contrast, Cr is only incorporated as Cr³⁺ [52] and Ni as Ni²⁺ [53, 54]. However, there are reports that Ni⁺ ions can be created by reducing Ni²⁺ due to an annealing treatment or γ -radiation [10]. Nevertheless, there are no absorption bands reported from Ni⁺.

2.2.3.2 Hydrogen impurities

OH-stretch vibration Hydrogen is a typical impurity in many different materials. Especially oxide compounds tend to incorporate hydrogen ions in order to form OH⁻ molecular ions [55, 56]. In the case of LiNbO₃, hydrogen ions (H⁺) enter the crystal via attachment

to the starting powders or during crystal growth in ambient air [56,57]. Note also that LiNbO₃ crystal boules are single-domain through post-growth poling by an external electric field at temperatures close to the Curie temperature [31]. This poling treatment can also lead to hydrogen incorporation [58]. The H⁺ ions in LiNbO₃ form OH⁻ stretch-vibration bonds which can be excited by photons resulting in the so-called "OH-stretch-vibration absorption peak" (OH-vibration peak). In CLN the OH-vibration peak is strongly ordinarily polarized from which it can be inferred that the OH⁻ bonds are mainly oriented perpendicular to the crystal **c**-axis [56]. It was shown that the hydrogen ions are located in the oxygen plane perpendicular to the **c**-axis. Taking into account lattice distortions, there are six different OH-bonds possible, however only four are energetically favorable [59]. In CLN the OH-vibration peak usually is a superposition of up to five different absorption bands whose amplitudes vary with temperature. The maximum of that composed absorption band is centered at about 3483 cm⁻¹ with a full-width-at-half-maximum (FWHM) of about 32 cm⁻¹. The exact absorption band position depends on stoichiometry, crystal growth method, and impurities [24,59].

Combination bands and higher harmonics of the OH-vibration peak Besides the characteristic OH vibration band there are higher harmonic OH-vibration bands, e.g. the first overtone can be found at 6778 cm⁻¹ [60], a second overtone can be found at 9900 cm⁻¹ [61]. Another type of OH-related absorption bands can be found at 4448 and 4435 cm⁻¹. It was shown that these bands are vibration-libration combination side bands [57,62,63].

Determination of the hydrogen concentration from the OH-vibration peak The magnitude of the of the OH-peak for the hydrogen concentrations typically found in as-grown LiNbO₃ boules is on the order of 1 cm⁻¹ [57]. The magnitude and peak area of the OH-vibration peak is a measure for the hydrogen concentration of the crystal and it usually is easy to measure, thus the OH-vibration peak is commonly used as a tool to determine the hydrogen content. In the case of CLN the absorption cross section of the OH vibration band (being the superposition of the different vibrational-bonds) is about $\sigma_{\text{OH}} = (6 \pm 3) \times 10^{-20}$ cm⁻² [64,65]. Typical hydrogen concentrations vary from 10²⁰ cm⁻³ for crystals grown in humid atmospheres and 10¹⁷ cm⁻³ grown in pure, dry oxygen [56].

Enrichment and depletion of LiNbO₃ with hydrogen As already indicated, hydrogen can also be incorporated into the crystal by post-growth annealing techniques. There are various processes known, e.g. annealing at temperatures as low as 700 °C in a water-vapor-rich atmosphere can homogeneously enrich the crystal with hydrogen within a few hours [56]. There are many other post-growth procedures that can incorporate hydrogen

into the crystal lattice such as proton exchange or high-energy H^+ ion implantation, just to name a few [56]. In contrast, hydrogen can also be permanently removed from the crystal by annealing LiNbO_3 at temperatures above $400\text{ }^\circ\text{C}$ in vacuum. After this annealing step the crystal is strongly reduced and subsequent annealing at $900\text{ }^\circ\text{C}$ in pure oxygen re-oxidizes the crystals. Such treatment decreases the hydrogen amount by at least two orders of magnitude (detection limit was reached) [66]. Adding or removing hydrogen by annealing treatment is a diffusion process [64]. The temperature dependence of the diffusion constant can be described by an Arrhenius equation

$$D = D_0 \exp\left(-\frac{E_A}{k_B T}\right), \quad (2.19)$$

where D_0 is the pre-exponential factor, k_B is the Boltzmann constant, T is the temperature, and E_A is the activation energy. Thus, using the one-dimensional diffusion equation, the proton out-diffusion can be approximately described by

$$A(t) \approx A_0 \exp\left(-\frac{D\pi^2 t}{d^2}\right), \quad (2.20)$$

where A is the absorbance, t is the time, A_0 is the initial OH^- absorbance of the as-grown crystal, and d is the sample thickness [64]. Proton out-diffusion experiments show that ($E = 1.1 \pm 0.2$) eV and $D_0 \approx 0.1\text{ cm}^2/\text{s}$ [64]. This shows, that no proton diffusion is possible at room temperature within finite time. Once the protons have left, e.g. due to an annealing process, and the crystal is cooled down to room temperature, the crystal stays proton-free. Note, it was under discussion for a long time whether OH^- ions or H^+ ions diffuse in or out in the according annealing process, however it could be shown that protons are moving, not entire OH^- ions [56, 67].

2.2.4 Overview – Optical transitions

Intrinsic and extrinsic crystal defects absorb light. The various defect absorption processes can be categorized in the following way:

- a) Internal transitions: Charge state of impurity ion is unchanged, e.g. crystal field transition.
- b) Charge transfer or intervalence transitions: Charge state of impurity ion is changed.
- c) Optical transfer of free and bound small polarons.

These processes are also schematically shown in Fig. 2.5. Thus, impurities and antisite defects strongly influence the optical properties of LiNbO_3 crystals.

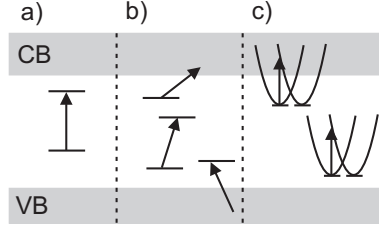


Figure 2.5: *Optical absorption processes in LiNbO_3 (redrawn from [40]). a) Internal transitions, e.g. crystal field transitions. b) Charge transfer or intervalence transitions. c) Optical transfer of free (upper diagram) or bound (lower diagram) small polarons. CB denotes the conduction band, VB the valence band.*

The absorption peaks caused by the above mentioned optical absorption mechanisms are rather broad. It is assumed that the crystal lattice is subject to thermal vibrations that cause broadening of the energy levels [68]. Thus an absorption peak is best fit by a Gaussian line shape, i.e.

$$\alpha(\tilde{\nu}) = \alpha_0 + A \exp \left[-\frac{1}{2} \left(\frac{\tilde{\nu} - \tilde{\nu}_0}{\tilde{w}} \right)^2 \right], \quad (2.21)$$

where A is the amplitude, $\tilde{\nu}$ is the wavenumber, $\tilde{\nu}_0$ is the peak center, α_0 is an offset, and $2\tilde{w}$ is the width ($1/e^2$ value) that relates to the full width at half-maximum (FWHM) according to $\text{FWHM} = 2\tilde{w}\sqrt{2\ln 2}$.

Note that absorption spectra are often plotted versus wavelength λ in the field of nonlinear optics. In the field of absorption spectroscopy, however, absorption spectra are commonly plotted versus wavenumber $\tilde{\nu} = 1/\lambda$ in the unit cm^{-1} because the wavenumber is proportional to photon energy. Both notations are used in this work.

2.3 Implications of optical absorption – Light-induced refractive index changes

Due to its large nonlinear-optical coefficients and its commercial availability LiNbO_3 is an important material for nonlinear-optical applications such as SHG or OPO. In principle the optical quality of the commercially available LiNbO_3 crystals is already very good and commercial vendors of LiNbO_3 crystals typically control impurity levels of transition metals to values lower than 1 wt. ppm. Hence, absorption levels are small ($\alpha < 0.005 \text{ cm}^{-1}$) in the wavelength range 350 – 2950 nm. But absorption of photons, even at these low absorption levels, is the starting point of processes that most notably disturb nonlinear-optical devices.

Optical losses in LiNbO_3 crystals are mostly caused by electronic transitions. This can lead to changes of the refractive index in several ways. For nonlinear-optical applications it is very important that the transmitted laser beam is not distorted or scattered. It is also crucial that there are no slowly varying refractive index changes in the material along the propagation direction, because these would decrease the conversion efficiency of nonlinear optical processes due to dephasing.

LiNbO_3 crystals are susceptible to light-induced refractive index changes. There are mainly two mechanisms causing these refractive index changes:

- "Photorefractive effect" (PRE): Light-induced refractive index change due to charge redistribution. This redistribution of charges is caused by electronic excitation due to photon absorption. In the case this effect is unwanted it is also called "photorefractive damage" (PRD).
- "Thermo-optic effect": Light-induced refractive index change due to a temperature change. The temperature change is caused by heat accumulation inside the crystal because of photon absorption.

In the following PRD and the thermo-optic effect will be explained in more detail and their consequences for high-power optical applications will be shown.

2.3.1 Photorefractive effect in bulk-photovoltaic media

If a photorefractive crystal such as undoped CLN is illuminated with light of intensity $I(\mathbf{r})$ (\mathbf{r} is the spatial coordinate) at a wavelength where electrons are excited into the conduction band, a charge migration process is initiated due to the bulk-photovoltaic effect, diffusion, and drift or a combination of these effects. Note that the most prominent effect causing PRD, which is characteristic for LiNbO_3 , is the bulk-photovoltaic effect [25, 69–71]. The

charge transport can be described by the total current density \mathbf{j} :

$$\mathbf{j} = \mathbf{j}_{\text{phv}} + \mathbf{j}_{\text{diff}} + \mathbf{j}_{\text{drift}} . \quad (2.22)$$

The different contributions are as follows [72]:

- Bulk-photovoltaic current density \mathbf{j}_{phv} : In a simplified picture, the bulk photovoltaic effect can be described as a light-induced current in the absence of an electric field taking the form $\mathbf{j}_{\text{phv}} = \beta I \hat{\mathbf{c}}$ [25,69]. Here $\beta = \alpha_{33}$ is the bulk-photovoltaic constant of LiNbO₃ and α_{33} is the 33-component of the contracted third-rank bulk-photovoltaic tensor α_{ijk} [25] (Note: Implications of deviations from this simple model are discussed in Ch. 5) and $\hat{\mathbf{c}}$ is the crystal's \mathbf{c} -axis. Since this thesis is limited predominantly to LiNbO₃, we furthermore assume $\hat{\mathbf{z}} \parallel \hat{\mathbf{c}}$. The bulk-photovoltaic current causes charge migration to darker areas of the crystal which leads to formation of a space-charge field.
- Diffusion current density \mathbf{j}_{diff} : The diffusion current is given by $\mathbf{j}_{\text{diff}} = (k_{\text{b}}T)\mu_{\text{e}}\nabla\tilde{n}_{\text{e}}$, where k_{b} is the Boltzmann constant, T is the temperature, \tilde{n}_{e} is the concentration of electrons in the conduction band, and μ_{e} is the electronic mobility. The diffusion current also leads to the formation of a diffusion field .
- Ohmic drift current density $\mathbf{j}_{\text{drift}}$: The drift current is given by $\mathbf{j}_{\text{drift}} = \sigma\mathbf{E}$, where σ is the conductivity and \mathbf{E} is the total electric field. This total electric field is the summation of all fields involved, i.e. it consists of space-charge fields, diffusion fields, drift fields etc.

The current density then takes the form

$$\mathbf{j} = \beta I \hat{\mathbf{z}} + k_{\text{b}}T\mu_{\text{e}}\nabla\tilde{n}_{\text{e}} + \sigma\mathbf{E} . \quad (2.23)$$

We assume intensities low enough that the photoconductivity is linear in the optical intensity, i.e. $\sigma_{\text{photo}} = \kappa I$, with κ being the specific photoconductivity. Then the total conductivity σ is given by

$$\sigma = \kappa I + \sigma_{\text{d}} , \quad (2.24)$$

where σ_{d} is the dark conductivity. Note, the photoconductivity, the dark conductivity, as well as the electronic mobility are in principle second rank tensors, however in LiNbO₃ these tensor properties can be neglected [8, 73, 74]. In contrast, in materials such as barium titanate (BaTiO₃) or Cr-doped strontium barium niobate mixed crystals (Cr:Sr_{0.61}Ba_{0.39}Nb₂O₆, Cr:SBN) electric tensor properties cannot be neglected [75, 76].

The charge migration process during illumination changes the total electric field \mathbf{E} with time, and due to the electro-optic effect this change in the electric field creates a refractive

index change according to

$$\Delta n_{[o,e]} = -n_{[o,e]}^3 r_{[13,33]} \frac{E_z}{2}, \quad (2.25)$$

with $n_{[o,e]}$ being the refractive indices for ordinarily and extraordinarily polarized light, respectively, and $r_{[13,33]}$ being the elements of the electro-optic tensor (13 and 33 are contracted indices) with $r_{33} \approx 3r_{13}$ in LiNbO_3 . The variable E_z denotes the z -component of \mathbf{E} . Note that there is no contribution from the x - and y -component of the electric field due to vanishing tensor elements. In the following section we only consider extraordinarily polarized light, thus $\Delta n = -n_e^3 r_{33} E_z / 2$, unless otherwise noted. If the electric field \mathbf{E} is inhomogeneous, as will be the case for any finite-diameter beam, the resulting refractive index distribution will be inhomogeneous as well. This refractive index inhomogeneity leads to focusing or defocusing of the whole beam. It can also drive the evolution of smaller scale index inhomogeneities that cause light scattering and characteristic dynamic light patterns in the far field [77]. These dynamic patterns together with the beam distortion are commonly referred to as PRD or "optical damage".

Note that, although the refractive index change is a whole-beam effect, the characteristic pattern formation, especially the dynamical substructures, might be caused on a microscopic scale. The exact mechanism by which these patterns build up is still under discussion. The theory most discussed in literature is photo-induced or so-called "holographic light scattering", i.e. inhomogeneities such as the refractive index change cause weak initial scattering centers which then act as seeds for subsequent holographic amplification [77,78]. However, it is beyond the scope of this work to go into detail concerning the dynamic substructure formation, here the focus is on whole-beam effects, i.e. how the refractive index changes are caused on a macroscopic scale.

2.3.1.1 Suppression of bulk-photovoltaic photorefractive damage in LiNbO_3 : Magnesium doping

There are several methods to reduce or even suppress bulk-photovoltaic PRD in CLN, e.g. by thermo-electrically oxidizing CLN [79] or heating the CLN crystal up to a temperature of about 200 °C [29]. However, the most common solution to this problem is to dope LiNbO_3 with magnesium oxide (MgO) [9]. Photorefractive damage can only be inhibited if the MgO concentration in LiNbO_3 crystals of near congruent composition is at least 4.5 – 4.9 mol% [9,80]; in near-stoichiometric LiNbO_3 crystals doping concentrations of about 0.8 – 1.8 mol% are sufficient [81,82]. This doping-threshold is called "optical damage threshold". In the following, 5-mol% MgO-doped LiNbO_3 crystals will be denoted MgO:LN or LiNbO_3 :MgO unless otherwise mentioned. These crystals do not show PRD even at very high light intensities in the visible wavelength range [12,83]. The MgO-doping changes some of the crystal properties significantly, e.g. the photoconductivity is one to

two orders of magnitude larger in MgO:LN than in CLN, using green laser light, and the bulk-photovoltaic current density is one order of magnitude smaller in MgO:LN than in CLN [81,84]. Both changes in properties contribute to the suppression of PRD in MgO:LN by lowering E_z (Eq. 2.25).

The effects of MgO doping are similar to bringing the crystal closer to stoichiometry. For MgO concentrations below the optical damage threshold, Nb_{Li} sites are substituted by Mg_{Li} sites. This means that the crystal lattice has to compensate for less Nb_{Li} , which means that there are less empty Nb sites available. When the MgO concentration reaches the optical damage threshold almost all Nb_{Li} sites are replaced by Mg_{Li} . Any further increase of the MgO concentration forces the Mg ions to occupy Nb sites (Mg_{Nb}). This shifts absorption bands, e.g. one characteristic change is the energy shift of the OH-vibration band from 3484 cm^{-1} (2870 nm) in CLN to about $3533 - 3539 \text{ cm}^{-1}$ (2830 – 2826 nm) in MgO:LN [9, 85]. Another difference is the polarization dependence: In CLN the OH-vibration band is strongly ordinarily polarized, i.e. e -wave light absorption can be neglected. In contrast, in MgO:LN an OH-vibration band contribution is also measured for e -wave light [85].

Another effect of MgO-doping above the optical-damage threshold is that transition metal impurities, which compete with Mg ions for the Li sites, are forced to occupy Nb sites. Thus doping LiNbO_3 with MgO also changes the absorption bands caused by transition metal impurities, e.g. the Cr^{3+} absorption band centered at 20850 cm^{-1} shifts to smaller wavenumbers in Cr_2O_3 -MgO-codoped LiNbO_3 crystals with increasing MgO-content [43]. Additionally, the fundamental UV absorption edge shifts to shorter wavelengths with increasing MgO concentration [86, 87].

Note that, since Mg ions occupy Li sites, the formation of $\text{Nb}_{\text{Li}}^{4+}$ small bound polarons is inhibited in MgO-doped LiNbO_3 crystals above the optical damage threshold and hence bipolarons do not occur as well [36]. In contrast, small free $\text{Nb}_{\text{Nb}}^{4+}$ polarons can occur in MgO:LN, but they are metastable and usually not populated as is the case in CLN [88, 89]. For the sake of completeness it has to be mentioned that there also are bound hole-polarons in MgO:LN absorbing around 20000 cm^{-1} , but they are also metastable and can only be populated by using high light intensities [36].

2.3.2 Thermo-optic effect and thermal lensing

Absorbed photons do not only generate charge transport due to charge excitation, but also lead to heat accumulation if the absorbed energy is not completely re-emitted as radiation. Absorbed light heats the crystal and, due to the thermo-optic effect, changes the refractive index. Heat accumulation and its resulting refractive index changes are a serious problem: Optical absorption limits the use of MgO-doped periodically poled MgO:LN. For instance,

heating due to optical absorption and subsequent beam-quality degradation in the infrared range have been reported in [14] for input-pump powers exceeding 10 W.

For CLN at the wavelength $\lambda = 632$ nm the thermo-optic refractive index change is [90]

$$\frac{dn_o}{dT} = -1.7 + 6.9 \times 10^{-3}T \quad (10^{-5}\text{K}^{-1}) \quad (2.26)$$

$$\frac{dn_e}{dT} = -2.6 + 22.4 \times 10^{-3}T \quad (10^{-5}\text{K}^{-1}) . \quad (2.27)$$

This creates a thermal lens with focal length [91]

$$f \approx \frac{\pi w^2 \lambda_{\text{th}}}{\alpha P L (dn/dT)} , \quad (2.28)$$

where P is the laser power, λ_{th} is the thermal conductivity ($\lambda_{\text{th}} = 5$ W/(m K) for LiNbO₃ [8]), w is the characteristic size of the beam (typically the beam radius), and L is the crystal length, however this approximation is restricted to cases where $f \gg L$. As an example, a laser beam with 10 W optical power, a typical beam radius of 150 μm , an absorption coefficient of $\alpha = 0.005$ cm⁻¹, and a crystal length of 20 mm at $T = 100$ °C induces a thermal lens with about 100 mm focal length.

Importance of photon absorption for OPOs With respect to OPO operation photon absorption is not only troublesome because of the thermo-optic or photorefractive effect. Optical parametric oscillation is only possible if the pump power exceeds a certain threshold power P_{thr} , e.g. for continuous-wave (CW) singly-resonant OPOs this threshold power is proportional to the roundtrip losses of the resonant wave [92]. One portion of these losses is attributed to optical absorption in the nonlinear crystals, i.e. PPCLN or PPMgOLN. For instance, an absorption coefficient on the order of 0.0001 cm⁻¹ is considered to be troublesome for typical continuous-wave (CW) singly-resonant OPO configurations using 10 – 20 W of pump power.

All these facts together show that, even if PRD is suppressed, e.g. in MgO:LN, small absorption losses limit the usability of LiNbO₃ crystals, e.g. optical absorption increases OPO pump power thresholds and absorption-induced heating can disturb the phase matching in nonlinear optical setups, can cause thermal lensing, or even destroy the LiNbO₃ crystal. The demanding question is, what causes absorption bands in MgO:LN and CLN and how can they be reduced. Thus a thorough study on absorption in nominally-pure, optical-grade MgO:LN and CLN has to be performed between 350 – 2950 nm, i.e. the spectral range of interest for most optical applications.

2.4 Thesis overview

The major scope of this dissertation is to study, characterize, and develop means to avoid the residual optical absorption in nominally undoped CLN and MgO:LN crystals that limits their performance in nonlinear-optical applications [13, 14, 29]. Thus a careful study of the absorption spectra in CLN and MgO:LN is necessary. So far, conventional absorption spectroscopy in lithium niobate using grating absorption spectrophotometers has been limited to measurement of absorption coefficients down to values on the order of 0.01 cm^{-1} . Hence it was not possible to determine the origin of residual optical absorption in these crystals and find ways to suppress it. Therefore one component of this dissertation is to increase measurement sensitivity of already existing conventional spectroscopic methods in order to measure absorption coefficients down to $1 \times 10^{-4} \text{ cm}^{-1}$ in some spectral ranges and to study the absorption spectra of CLN and MgO:LN. Thus, in chapter 3 the method used for the absorption spectroscopy experiments will be explained and results of absorption measurements in CLN and MgO:LN crystals will be presented and analyzed in the spectral range 350-2000 nm ($28600\text{-}5000 \text{ cm}^{-1}$). Impurities will be identified and the question will be addressed to which extent transition-metal impurities impact the optical absorption in these crystals. To accomplish this characterization, absorption spectra of CLN and MgO:LN will also be compared to absorption spectra of intentionally transition-metal doped LiNbO_3 and MgO:LN crystals.

In chapter 4 the results of absorption measurements in CLN and MgO:LN are presented for the spectral range 2000 – 2950 nm ($5000 - 3400 \text{ cm}^{-1}$) which is of special interest for OPO applications. In this spectral range the main impurity causing residual absorption is already known to be hydrogen [56, 63]. The demanding question will be addressed, if there are unknown absorption bands in CLN and MgO:LN which have not been discovered yet because conventional optical absorption measurements were limited to measure absorption coefficients exceeding 0.01 cm^{-1} . As it was discussed in Sect. 2.3.2 an absorption coefficient of only 0.0001 cm^{-1} is already too large for some nonlinear-optical applications.

The other major component of this dissertation is to study the effects absorption of photons can have on MgO:LN other than causing heating and thermo-optic lensing. These studies will be presented in chapter 5. As already mentioned, bulk-photovoltaic PRD is suppressed in MgO:LN, so the question will be addressed if there are experimental parameters so that other forms of PRD, that are relevant for applications, occur.

Chapter 3

Absorption in congruent LiNbO_3 and $\text{LiNbO}_3:\text{MgO}$ between 350 and 2000 nm

So far, studies of absorption in LiNbO_3 have focused on multi-valence transition metal impurities such as iron (Fe), copper (Cu), or manganese (Mn) in intentionally Fe-, Cu-, or Mn-doped LiNbO_3 crystals, because these impurities can be incorporated in different valence states. Thus they cause optical absorption and play a key role in the bulk-photovoltaic process in LiNbO_3 crystals [41,70,93]. These ions are incorporated as unwanted impurities in nominally pure CLN, especially Fe [39,41]. They are believed to be responsible for bulk-photovoltaic photorefractive CLN, however this is still under discussion [24]. The effects of these impurities on photon absorption in CLN have not been studied yet due to the limited detection resolution of the absorption coefficient in these studies, which is about 0.01 cm^{-1} [24]. The same applies to $\text{MgO}:\text{LN}$, where bulk-photovoltaic PRD is suppressed, but absorption is still a problem. Thus, in this chapter the residual optical absorption in nominally pure CLN and $\text{MgO}:\text{LN}$ crystals is studied in the spectral range 350 – 2000 nm ($28600 - 5000 \text{ cm}^{-1}$). In order to identify small absorption bands, the obtained spectra are compared to spectra of intentionally doped crystals. While those spectra for CLN can be mostly found in literature, there is a lack of transition-metal codoped $\text{MgO}:\text{LN}$ absorption spectra. Hence, in addition to nominally pure CLN and $\text{MgO}:\text{LN}$ crystals, $\text{MgO}:\text{LN}$ crystals intentionally codoped with Fe, Cr, Cu, Ni, and Mn are grown and their optical absorption is also studied. Note also that one LiNbO_3 boule doped with only Cr is grown in order to simplify comparison of Cr-doped LiNbO_3 to undoped CLN.

3.1 Methods

High-precision optical transmission measurements are performed with a Varian Cary 500 dual-beam absorption spectrophotometer, which is a grating spectrophotometer operating in the wavelength range 200 – 3050 nm ($50000\text{-}3300\text{ cm}^{-1}$). The wavelength resolution used in this work is 1 nm. The setup is shown schematically in Fig. 3.1.

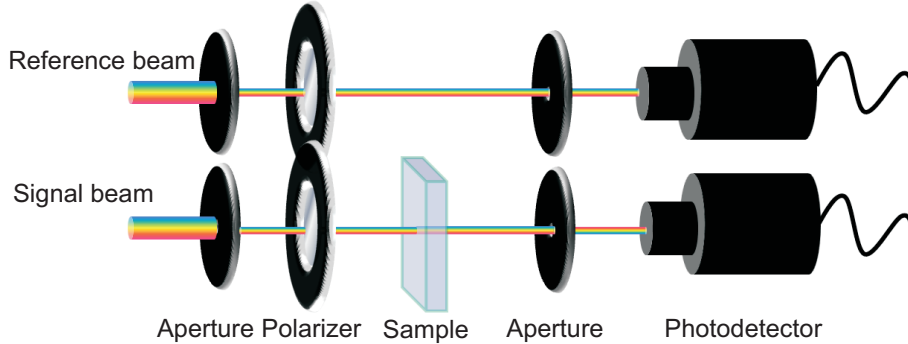


Figure 3.1: *Optical dual-beam absorption spectroscopy.*

Since the beam diameters in both arms are larger than 1 cm, apertures are used to limit the size of the beam. The spectrophotometer has two arms, in one arm the optical transmission of the sample is measured, the other arm can be used as the reference. Glan-Taylor polarizing prisms are used as polarizers. The spectrophotometer has several drawbacks that make precision measurements difficult, e.g. it switches detectors at 800 nm and lamps at 350 nm which leads to different measurement sensitivities in different spectral ranges. The beam is also slightly divergent which is an obstacle for studying thick samples. The thicknesses of samples used in this study are chosen such that the assumption of a parallel beam within the sample is still valid. The maximum sample thickness is 25 mm. Furthermore, in order to maintain stable conditions, the measurement chamber is purged with dried air and it is made sure that there is a homogeneous distribution of dried air within the chamber and that air flow is very stable.

Prior to each measurement a baseline measurement is performed with no samples in either of the measurement arms. Then the sample is consecutively thoroughly cleaned with water, acetone, and isopropanol and placed in the measurement arm (the reference arm contains no sample) and optical transmission is measured. The data are then automatically corrected for the baseline by the Cary 500 software. Finally the absorption coefficients are calculated from the optical transmission data by using Eq. 2.13, taking into account the Sellmeier equation for CLN or MgO:LN respectively [94].

Then the peak positions are determined, thus one ideally would subtract the intrinsic

Wavelength range (nm)	Accuracy	
	Background (offset) (cm^{-1})	Absorption band (cm^{-1})
300- 800	0.005	0.0001
800-2000	0.01	0.005
2000-2950	0.001	0.0005

Table 3.1: *Measurement accuracy for spectrophotometer measurements.*

band edge absorption. Unfortunately, absorption measurements, especially in the blue and UV spectral range, are very sensitive to Rayleigh scattering which increases steeply with decreasing wavelength, i.e. the intensity of scattered light is proportional to $1/\lambda^4$. This adds additional losses. An imperfect Fresnel correction adds further uncertainty. Therefore, in order to determine the correct shape and amplitude of the absorption peaks, a common procedure in spectroscopy is used, which assumes that the background can be approximated by a straight line in the vicinity of an absorption peak [95]. Hence in the visible and near-UV range Gaussian lineshapes (Eq. 2.21) on top of a straight line are fitted to the observed absorption peaks in the respective wavelength range.

Note also that an imperfect Fresnel correction due to uncertainties in the angle of the incident light, thickness of the sample, and surface scattering can lead to an offset of the underlying absorption background within the spectral region of an absorption peak. This limits the accuracy for the underlying absorption background. However the accuracy of the measured absorption bands with respect to that background is much higher. Both accuracies also vary for different spectral regions because of lamp, grating, and detector changes in the spectrophotometer itself. A list of the spectrophotometric accuracy is listed in Tab. 3.1.

Note that the detection limit in terms of α in the range 800–2000 nm ($12500\text{--}5000\text{ cm}^{-1}$) is worse than in the other spectral ranges covered by the spectrophotometer. Unfortunately this limit is caused by the instrument detectors and the use of large crystals does not increase measurement accuracy in this spectral range.

3.2 Crystals

Since the impurity content in today's commercially available, optical-grade CLN and $\text{MgO}:\text{LN}$ crystals is specified by the crystal growers to be lower than 1 wt. ppm for transition metal impurities, the optical path length within the crystal should be as long as possible in order to achieve the best signal-to-noise ratio for the optical absorption measurements. This means that the optical path within the crystals should be on the order of 20 – 25 mm. Hence crystals with standard wafer-thickness of about 1 mm cannot be used for conventional spectrophotometric means, instead customized crystals (with respect to size) are grown, cut, and polished by Crystal Technology, Inc.

3.2.1 Undoped congruent LiNbO_3 crystals

Congruent LiNbO_3 crystals can be grown very efficiently: Because of congruency it is possible to convert large fractions from the initial melt into crystalline material without having any or only minimal axial composition variations with respect to the Li and Nb concentration. Thus a CLN boule is grown for which the fraction of melt converted to crystal material exceeds 80 %. Such a high conversion factor is commonly only applied for CLN crystals intended to be used in surface acoustic wave (SAW) devices, however for this special boule the same raw materials are used as for the growth of optical quality CLN boules. The reason for growing such a large boule is that a large melt-to-crystal conversion helps to reveal segregation of impurities that lead to concentration gradients along the growth axis.

Two CLN crystal cubes, of dimensions $20 \times 20 \times 20 \text{ mm}^3$, are cut from this boule and they are oriented following standard convention orientation for the x , y , and z principal axes with respect to the crystal boule (Tab. 3.2).

Boule position	Dimensions $x \times y \times z$ (mm^3)	Short name
Top	$20 \times 20 \times 20$	CLN_T
Bottom	$20 \times 20 \times 20$	CLN_B

Table 3.2: *CLN crystals used in the experiments and their short names.*

The solidified fraction, defined as the crystallized portion of material over the initial melt charge, is approximately 15 % for the CLN cube fabricated from the top part of the boule, whereas the sample fabricated from the bottom part of the boule corresponds to a solidified fraction of about 70 %. The x -faces are polished to high optical quality. A representative picture of one of the CLN cubes is shown in Fig. 3.2

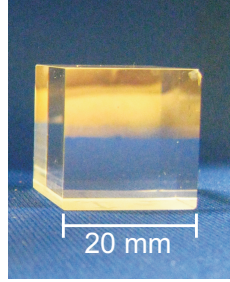


Figure 3.2: *Picture of a CLN cube.*

Two additional crystal pieces, one from the top and one from the bottom of the CLN boule, are used for impurity analysis. The impurity levels are measured by glow discharge mass spectrometry (GDMS) at Shiva Technologies (Evans Analytical Group). The GDMS technique can resolve trace impurities down to sub-parts per million and even parts per billion when interferences are not present; the precision (reproducibility) of the technique is about 30%. The drawback of GDMS analysis is that the samples are destroyed for GDMS sample preparation and, furthermore, GDMS cannot determine the valence state of multivalence ions incorporated into the crystal. Thus GDMS analysis is a helpful tool to investigate distribution coefficients, but it is not possible to directly connect the impurity content to optical absorption.

The GDMS results show that mainly five transition metal impurities are incorporated. The results are summarized in Table 3.3.

	Impurity level (wt. ppm)				
	Fe	Cr	Ni	Cu	Mn
Top	1.20	0.50	0.14	0.09	0.03
Bottom	1.10	0.06	< 0.01	< 0.05	< 0.01

Table 3.3: *GDMS results for CLN*

The Cr concentration changes dramatically from top to bottom. For Cu and Ni this is also the case, but the concentrations of Cu and Ni in the top part of the boule are already much lower than the concentration of Cr in the top part. The only impurity that is evenly distributed within the crystal is Fe. The Mn concentration is low compared to the concentrations of the other impurities.

3.2.2 MgO-doped LiNbO_3 crystals

All MgO:LN crystals used for this study are provided by Crystal Technology, Inc. and they are all doped with 5 mol% MgO and the Li/Mg ratio is chosen such that all MgO:LN crystals are above the optical-damage threshold (OH absorption peak is shifted to shorter wavelengths compared to that of CLN). The crystal samples are listed with their short names in Tab. 3.4.

MgO:LN boule	Dimensions $x \times y \times z$ (mm ³)	Short name
A	$25 \times 15 \times 20$	MgOLN ₁
A	$25 \times 15 \times 20$	MgOLN ₂
A	$25 \times 15 \times 20$	MgOLN ₃
A	$25 \times 15 \times 20$	MgOLN ₄
B	$25 \times 25 \times 25$	MgOLN _{Cube}
R	$20 \times 6 \times 7$	MgOLN _{Ref,T}
R	$20 \times 6 \times 7$	MgOLN _{Ref,M}
R	$20 \times 6 \times 7$	MgOLN _{Ref,B}

Table 3.4: MgO:LN crystals used in the experiments and their short names.

Samples MgOLN₁, MgOLN₂, MgOLN₃, MgOLN₄ are all cut from one optical grade commercial MgO:LN boule A with 80 mm diameter. In contrast to the CLN samples it is not possible to cut samples of that size from the top and bottom of the boule. MgO:LN samples MgOLN₁, MgOLN₂, MgOLN₃, and MgOLN₄ are all cut from the same slab from the center of the boule. The reason for that is that MgO-doped LiNbO_3 crystals present measurable axial Mg-Li composition variations [96], i.e. the distribution coefficient for Mg is larger than unity. This limits the fraction of how much crystalline material can be pulled from an initial melt charge. The melt fraction crystallized typically is below 30% ensuring high-purity and strain-free optical-quality material [94]. For comparison reasons a crystal sample MgOLN_{Cube}, grown under the same conditions as boule A, is cut from the center of another optical-grade MgO:LN boule B. Additionally, an optical grade MgO:LN boule R is grown using the same growth conditions as were used to grow boules A and B, but with an exceptionally large melt fraction of about 50% being converted into crystal and only having a diameter of about 45 mm. This helps to study segregation effects of impurities in MgO:LN. From this boule samples are cut from the top ($\approx 10\%$ solidified melt fraction, MgOLN_{Ref,T}), the center ($\approx 30\%$ solidified melt fraction, MgOLN_{Ref,M}), and the bottom ($\approx 50\%$ solidified melt fraction, MgOLN_{Ref,B}).

All MgO:LN samples listed in Tab. 3.4 have their x -faces polished enabling e - and o -wave

Impurity level (wt. ppm)				
Fe	Cr	Ni	Cu	Mn
≤ 1	≤ 0.5	≤ 0.1	≤ 1	≤ 0.1

Table 3.5: Specified impurity content of the MgO:LN crystals.

illumination. Unfortunately the surface polish of the samples from boule R is not as good as the surface polish of samples cut from boules A and B. Inspection reveals some small scratches and dents. These surface inhomogeneities can lead to scattering losses which leads to artifacts in the absorption measurements.

The impurity content of the optical grade MgO:LN crystals is specified by Crystal Technology, Inc. as it is summarized in Tab. 3.5. Further GDMS data of the specific samples are not available.

3.2.3 $\text{LiNbO}_3\text{:MgO}$ crystals codoped with a transition metal

In order to identify absorption bands in the absorption spectra of nominally impurity-free MgO:LN crystals, five boules of transition-metal codoped MgO:LN crystals are grown. Dopants are Fe, Cu, Cr, Ni, and Mn. The MgO doping level is again 5 mol% and all codoped crystals are above the optical damage threshold. The particular dopant concentration of the transition metal oxide is listed in Tab. 3.6 for each boule.

Transition metal oxide	Doping wt. ppm	Transition metal	Doping wt. ppm	MgO added
Cr_2O_3	50	Cr	34.2	✓
CuO	100	Cu	79.9	✓
Fe_2O_3	100	Fe	73.7	✓
MnO_2	100	Mn	63.2	✓
NiO	50	Ni	39.2	✓
Cr_2O_3	40	Cr	27.4	--
Reference MgO:LN boule R	--	--	--	✓

Table 3.6: Transition metal dopant and their concentration in the melt.

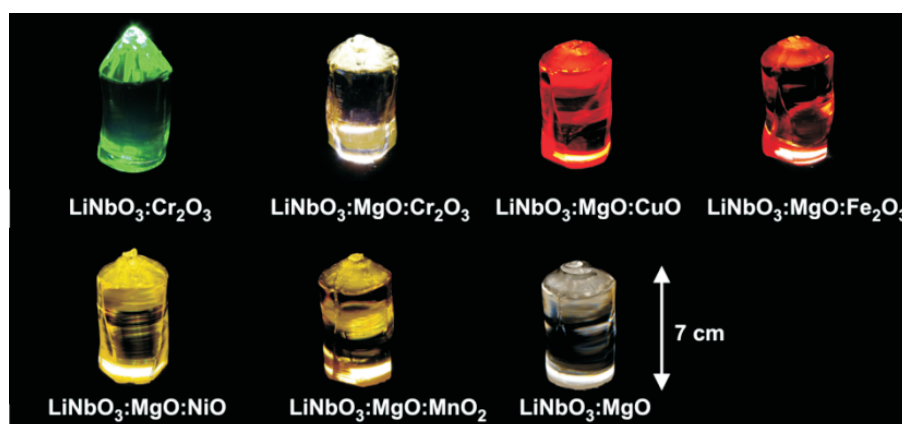


Figure 3.3: Pictures of MgO:LN and CLN crystal boules which are each (co-)doped with a transition metal

The crystal boules are grown with the same melt fraction converted into crystal material and having the same dimension as the optical grade boule R described in the previous section. Thus boule R also serves as reference for the intentionally transition-metal codoped MgO:LN boules. Furthermore, one LiNbO_3 crystal boule doped with Cr, but without Mg, is grown. Pictures of the crystal boules are shown in Fig. 3.3.

Samples of dimensions $20 \times 6 \times 7 \text{ mm}^3$ ($x \times y \times z$) are cut from the top, middle, and bottom of each boule with approximately 10%, 30%, or 50% of the melt fraction converted into crystal material respectively. Note that the sample from the top of the Mn-codoped MgO:LN cracked during dicing, and therefore it is not available for measurements. The x -surfaces of all samples are polished, but polishing characteristics of these samples are different from those of the optical grade MgO:LN samples and some scratches on the surfaces are visible. However this does not significantly influence the absorption measurements because the doping level is chosen such that minor losses due to surfaces inhomogeneities can be neglected with respect to the strength of optical absorption.

3.3 Results and discussion: Congruent LiNbO_3 crystals

In this section the results of the absorption measurements with the CLN and the Cr-doped LiNbO_3 crystals will be presented and discussed.

3.3.1 Results

3.3.1.1 Undoped congruent LiNbO_3 crystals

In Fig. 3.4 absorption spectra of the top-part sample CLN_T (solid line) and the bottom-part sample CLN_B (dashed line) are shown for *o*-wave (a) and *e*-wave illumination (b) in the visible spectral range.

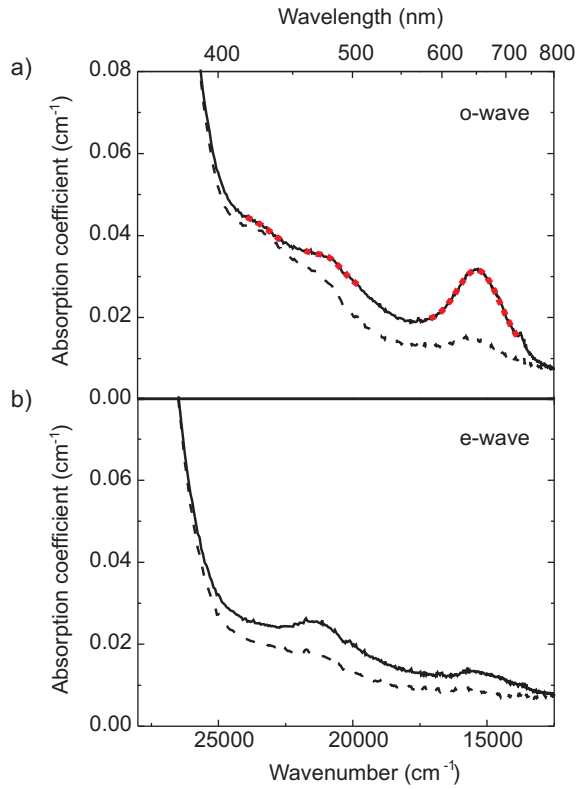


Figure 3.4: Absorption spectra of the top-part sample CLN_T (solid line) and the bottom part sample CLN_B (dashed line) for ordinarily polarized light (a) and extraordinarily polarized light (b). As an example, the fits for the top part of the *o*-wave spectrum are presented (red square-dotted line).

Crystal	Polarization	$\tilde{\nu}_0(\text{cm}^{-1})$	$\tilde{w} (\text{cm}^{-1})$	$A (\text{cm}^{-1})$
CLN Top	<i>o</i> -wave	13750	70	0.0023
		15300	900	0.0174
		20850	400	0.0023
		23400	400	0.0006
CLN Bottom	<i>o</i> -wave	13750	–	–
		15500	600	0.0023
		20900	–	–
		23400	–	–
CLN Top	<i>e</i> -wave	13650	200	0.0006
		15550	1500	0.0065
		21350	700	0.0040
CLN Bottom	<i>e</i> -wave	15650	300	0.0010
		21300	600	0.0018

Table 3.7: Absorption peak parameters of the CLN crystals for *o*-wave and *e*-wave illumination, where $\tilde{\nu}_0$ denotes the peak center, $2\tilde{w}$ the peak width parameter, and A the peak fit amplitude. Entries with "–" indicate that a fit is not possible, because $\alpha < 0.0001 \text{ cm}^{-1}$. In this case, $\tilde{\nu}_0$ is the position of the local maximum absorption.

Figure 3.4 shows that the measurement method is able to clearly resolve distinct absorption bands whose amplitude is on the order of 0.0005 cm^{-1} . The results reveal that absorption features cover the whole visible spectrum. In order to quantify the results, the absorption peak parameters $\tilde{\nu}_0$, \tilde{w} , and A defined in Eq. 2.21 are determined for each absorption peak by the fit procedure described in Sect. 3.1. The results are summarized in Tab. 3.7.

For both, *o*-wave and *e*-wave illumination, the absorption in the bottom part of the boule is drastically decreased over the entire visible spectrum. In the bottom part the absorption peak at 15500 cm^{-1} almost vanishes. In the near-infrared range $800 - 2000 \text{ nm}$ ($12500 - 5000 \text{ cm}^{-1}$) the accuracy of the absorption measurement is not sufficient to resolve any possible absorption peaks.

Fit accuracy Although the Gaussian peak fits show less than 1 % error, the fits slightly depend on the definition of the peak boundaries which is a systematic error. Hence, the actual errors for the peak parameters are larger than the error obtained by least-square fits. Therefore a set of errors for the peak position, width, and amplitude is estimated for

every peak which takes into account the difference in the fit results when slightly different peak boundaries are used. The accuracy for A is about 0.0001 cm^{-1} , for $\tilde{\nu}_0$ and $\tilde{\omega}$ about 50 cm^{-1} . It is important to note that, in the case of a weak broad absorption peak on top of a larger absorption shoulder, errors from assuming a linear peak background will appear, although the respective peak fit might have a very small error. This is the case, e.g., for the e -wave spectrum of the bottom CLN cube. However, for the narrow peaks at 13750 cm^{-1} (o -wave) and 13650 cm^{-1} (e -wave) $\tilde{\nu}_0$ can be determined to an accuracy of 10 cm^{-1} and $\tilde{\omega}$ to about 25 cm^{-1} .

3.3.1.2 Cr-doped LiNbO_3 crystals

In Fig. 3.5 absorption of the Cr-doped LiNbO_3 crystal boule is shown. As can be seen

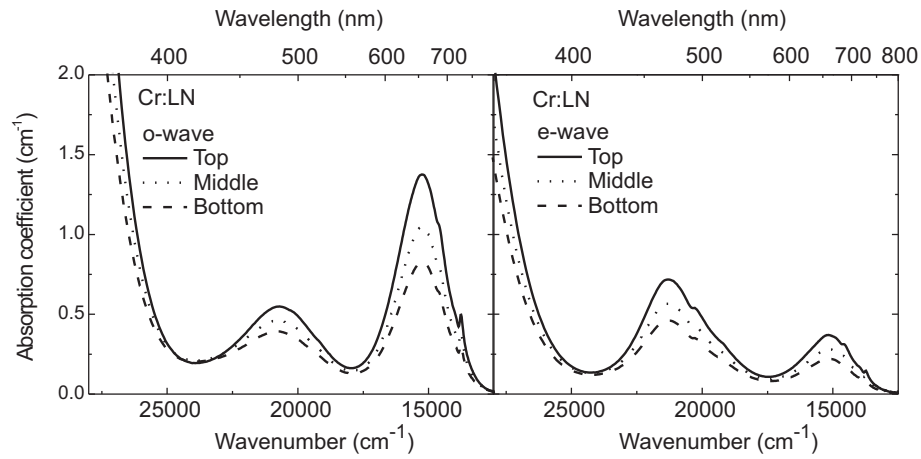


Figure 3.5: Absorption spectra of LiNbO_3 doped with 27 wt. ppm Cr for o -wave (left) and e -wave illumination (right).

from Fig. 3.5, there is a significant decrease in absorption peak amplitude A from the top to the bottom of the boule, however, spectral positions $\tilde{\nu}_0$ of the peaks do not change. Absorption peak parameters from peak fits for the sample cut from the top part of the boule are summarized in Tab. 3.8.

Table 3.8 shows that the centers of the most pronounced absorption peaks of Cr-doped LiNbO_3 , e.g. $\tilde{\nu}_0 = 13750, 15300, 20750$ for o -wave light, coincide with those of the most pronounced peaks in CLN, that are listed in Tab. 3.7.

Dopant	wt. ppm	$\tilde{\nu}_0$ (cm^{-1})	$\tilde{\omega}$ (cm^{-1}) o-wave	A (cm^{-1})	$\tilde{\nu}_0$ (cm^{-1})	$\tilde{\omega}$ (cm^{-1}) e-wave	A (cm^{-1})
Cr	27.4	13750	50	0.07	13750	50	0.01
		14550	100	0.06	14500	100	0.03
		15300	800	1.18	15200	750	0.26
		20750	1250	0.40	19300	500	0.13
					20050	220	0.06
					21250	950	0.58

Table 3.8: Peak fit parameters of the absorption peaks of the Cr-doped LiNbO_3 crystal from the top part of the boule for o-wave and e-wave illumination. The accuracy for A is about 0.01 cm^{-1} , for $\tilde{\nu}_0$ and $\tilde{\omega}$ the accuracy is about 50 cm^{-1} . For the narrow peaks at $\tilde{\nu}_0 = 13750 \text{ cm}^{-1}$ the error for the spectral position is only about 10 cm^{-1} . Same systematic error sources as for the CLN absorption spectra apply.

No absorption band can be detected in the spectral range $800 - 2000 \text{ nm}$ ($12500 - 5000 \text{ cm}^{-1}$), that is why the spectra for this range are not shown in Fig. 3.5.

3.3.2 Discussion

The absorption spectra of the CLN crystals show that it is indeed possible to resolve distinct absorption bands in optical-grade CLN. In the following the results of the absorption measurements with CLN crystals are discussed and related to impurity analysis data and spectra of transition-metal doped LiNbO₃ absorption spectra. These data are either available from literature (Tab. 2.2) or the results of the absorption measurements with Cr-doped LiNbO₃ crystals in Fig. 3.5.

3.3.2.1 Identification of impurities in undoped congruent LiNbO₃ crystals

Chromium GDMS measurements reveal that the main impurities in CLN are the transition metals Fe, Cr, Cu, Ni, and Mn. Thus the absorption spectra of CLN are analyzed with respect to characteristic absorption bands these impurities usually cause in absorption spectra of intentionally transition-metal doped LiNbO₃ crystals known from literature (see Tab. 2.2).

The absorption-spectra of the undoped CLN crystals depicted in Fig. 3.4a and b show absorption peaks centered at the same spectral positions as the peaks in the spectra of the Cr-doped LiNbO₃ crystal in Fig. 3.5, i.e. The *o*-wave absorption spectra of CLN and Cr-doped LiNbO₃ show the most pronounced absorption peaks centered at 15300 cm⁻¹ and 20850 cm⁻¹, and the *e*-wave absorption spectra of CLN and Cr-doped LiNbO₃ show the most pronounced absorption peaks centered at 21350 cm⁻¹ and 15550 cm⁻¹. The observed absorption peaks are in accordance with Cr³⁺ absorption bands known from literature (see Table 2.2). Additionally the characteristic narrow absorption peaks known from literature (Table 2.2) can clearly be identified around 13750 cm⁻¹ (*o*-wave) and 13650 cm⁻¹ (*e*-wave) in the CLN spectra shown in Fig. 3.4 as well as in the spectra of the Cr-doped LiNbO₃ crystal shown in Fig. 3.5. Comparison of the five impurities that are detected in the CLN crystals by GDMS measurements (Tab. 3.3), i.e. Fe, Cu, Cr, Ni, and Mn, to literature data of impurities and their respective absorption bands listed in Tab. 2.2 shows, that only Cr³⁺ can absorb in all three spectral regions, i.e. around 13850, 15300, and 21000 cm⁻¹ for *o*-wave and *e*-wave light. It is also remarkable that the absorption peak amplitude decreases from top to bottom, which is also characteristic for Cr-impurities in LiNbO₃ as can be seen from Fig. 3.5. Thus we deduce that Cr³⁺ impurities cause the dominant absorption features in the CLN samples.

Iron It is interesting to note that the *o*-wave absorption peak around 15300 cm⁻¹ in the bottom part of the boule almost vanishes, whereas this is not fully the case in the region around 20850 cm⁻¹; a shoulder remains. The most probable impurity to cause this absorption shoulder is Fe²⁺. According to the GDMS data in Tab. 3.3, the Fe content is almost

the same for the top and the bottom CLN sample. If part of the Fe impurities are incorporated in the valence state Fe^{2+} an *o*-wave absorption peak centered around 20970 cm^{-1} is caused, which extends from 16000 to 24000 cm^{-1} [45]. Hence, the Fe content may contribute significantly to the remaining *o*-wave absorption shoulder around 20850 cm^{-1} . Unfortunately, the actual Fe^{2+} content is unknown. However, the maximum Fe^{2+} content can be calculated according to Eq. 2.11 with the known Fe^{2+} -*o*-wave-absorption cross section at 20970 cm^{-1} of $\sigma_{\text{Fe}^{2+}}^{\text{abs}} = 4.63 \times 10^{-18} \text{ cm}^2$ [45] and the maximum contribution from Fe^{2+} ions to the shoulder in Fig. 3.4 of about $\alpha \approx 0.02 \text{ cm}^{-1}$. This results in $c_{\text{Fe}^{2+}} \leq 0.1 \text{ wt. ppm}$. It means, that from 1 wt. ppm Fe less than 10% of the entire Fe amount are actually incorporated as Fe^{2+} which contribute to the absorption shoulder. About 90% of the Fe amount are incorporated as Fe^{3+} which only absorbs photons via a narrow spin-forbidden transition (Tab. 2.2).

Similar observations are made for *e*-wave light: Comparison of the peaks in Fig. 3.4b to the peaks listed in Tab. 2.2 reveals, that Fe^{2+} ions most likely cause the residual absorption around 21350 cm^{-1} , but in this case the shoulder is less pronounced than for *o*-wave illumination. This is also expected, since the Fe shoulder around 21510 cm^{-1} for *e*-wave light is weaker than the corresponding shoulder around 20970 cm^{-1} for *o*-wave light [45].

Nickel, copper, and manganese The GDMS data in Tab. 3.3 show that Ni, Mn, and Cu are also present in the top part of the CLN boule, however, these impurities cannot be detected in the bottom part of the boule within the measurement accuracy.

The effect of Cu on the absorption in the spectral region between $25000 - 20000 \text{ cm}^{-1}$ ($400 - 500 \text{ nm}$) is small, e.g. the *o*-wave absorption cross section caused by Cu^+ absorption at 20970 cm^{-1} is about $\sigma_{\text{Cu}^+}^{\text{abs}} = 5.0 \times 10^{-18} \text{ cm}^2$ [97]. This leads to an absorption coefficient that is smaller than 0.002 cm^{-1} , if we assume that, similar to the Fe impurities, Cu is also mainly incorporated in the oxidized state Cu^{2+} and not as Cu^+ . So one obtains $c_{\text{Cu}^+} \leq 0.1 c_{\text{Cu}}$. A significant contribution to absorption from Cu impurities can be excluded for *e*-wave illumination, because the *e*-wave absorption cross sections between $25000 - 20000 \text{ cm}^{-1}$ ($400 - 500 \text{ nm}$) are even a factor of two smaller than the *o*-wave absorption cross sections [48].

Only little is known about the absorption cross sections of Ni and Mn ions in LiNbO_3 from the literature. However, Table 2.2 shows that Ni^{2+} ions probably cause the small *o*-wave absorption peak in CLN at 23400 cm^{-1} , and together with Cu^+ ions they contribute to the *o*-wave-absorption shoulder in the entire spectral region between 25000 and 18200 cm^{-1} . A small contribution from Ni is also possible for *e*-wave illumination, because an absorption band is situated at 21980 cm^{-1} in *e*-wave spectra of Ni-doped LiNbO_3 crystals. The impact of Mn impurities can probably be neglected because no absorption band can be seen in CLN between $15000 - 16550 \text{ cm}^{-1}$ ($600\text{-}500 \text{ nm}$),

the spectral region where Mn has absorption bands.

Polarons There is no measurable impact of polarons on the optical absorption; only a bipolaron absorption band centered at 20140 cm^{-1} caused by bipolarons could theoretically match the measured absorption bands in CLN, however, bipolarons are only stable in strongly reduced LiNbO_3 crystals as mentioned in Tab. 2.1, and our CLN samples are rather oxidized than reduced as can be seen from the fact that Fe is mainly incorporated in the oxidized state Fe^{3+} rather than in the state Fe^{2+} . Furthermore, the theoretical width of the bipolaron-absorption band (Tab. 2.1) is much larger than the observed width of the absorption bands in CLN.

3.3.2.2 Cr^{3+} absorption cross sections in LiNbO_3

The distribution coefficient of Cr in LiNbO_3 depends on many different parameters such as the pulling and rotation rates during crystal growth, and the electrical current flowing through the growing interface [98]. However, it is known that the distribution coefficient of Cr in LiNbO_3 is larger than unity, which agrees with our GDMS data. Hence it is expected that Cr-impurities in nominally undoped LiNbO_3 crystals show higher absorption in the top part of the boule than in the bottom part of the boule for almost the entire visible spectrum, as seen in Fig. 3.4. A Cr distribution coefficient larger than unity also means, that the more crystal material is grown, the more the Cr content of the melt is depleted and subsequently grown crystal material has less Cr incorporated. This gives opportunities to get a purified melt concerning Cr and therefore obtain crystals that contain less Cr.

The absorption cross sections of the main contributing impurities are useful in order to be able to estimate the peak absorption amplitude from GDMS data instead of being forced to cut large pieces of crystals out of a boule for absorption spectroscopy. The Fe^{2+} absorption cross sections in CLN are already known [45], but for Cr^{3+} there are several references giving different absorption cross sections, e.g. at 15500 cm^{-1} the *o*-wave absorption cross sections found in literature vary by almost two orders of magnitude: They are $12 \times 10^{-19} \text{ cm}^2$ [99], $8 \times 10^{-19} \text{ cm}^2$ [100], and $0.14 \times 10^{-19} \text{ cm}^2$ [101].

The absorption cross sections of the top and the bottom of the CLN crystal are determined according to Eq. 2.11 using the absorption peak amplitudes from the fits in Tab. 3.7 and the GDMS data from Tab. 3.3. However, it is more reasonable to determine the *o*-wave absorption cross section at 20850 cm^{-1} in a different way, because the *o*-wave absorption in CLN at 20850 cm^{-1} (Fig. 3.4a) is not very pronounced and there is an underlying absorption shoulder: From the spectra of the Cr-doped LiNbO_3 crystals in Fig. 3.5 $\sigma_{20850, \text{Cr}}^{\text{abs}}$ can be estimated to be 3.5 times smaller than $\sigma_{15300, \text{Cr}}^{\text{abs}}$. For *e*-wave light the same procedure is applied, i.e. for *e*-wave light $\sigma_{21300, \text{Cr}}^{\text{abs}}$ is about 2 times larger than $\sigma_{15500, \text{Cr}}^{\text{abs}}$.

The results for σ^{abs} are summarized in Tab. 3.9.

Crystal	$\tilde{\nu}_0$ (cm^{-1})	σ^{abs} (cm^2)
CLN Top: <i>o</i> -wave	15300	7×10^{-19}
	20850	2×10^{-19}
CLN Bottom: <i>o</i> -wave	15500	7×10^{-19}
	20900	2×10^{-19}
CLN Top: <i>e</i> -wave	15550	2×10^{-19}
	21350	4×10^{-19}
CLN Bottom: <i>e</i> -wave	15650	3×10^{-19}
	21300	6×10^{-19}

Table 3.9: Cr^{3+} absorption cross sections in LiNbO_3 .

The accuracy of the absorption cross sections in Tab. 3.9 is about 30 % because the accuracy of the GDMS data is about 30 %. Additionally, for the bottom CLN cube the absorption peak fits are less precise as was discussed earlier. The independently determined absorption cross sections for the top and the bottom CLN crystal agree with each other respectively within the accuracy limits. Furthermore, the *o*-wave absorption cross section for the peak centered at 15300 cm^{-1} agrees with the one determined from [100]. The *e*-wave absorption cross section is not given in Refs. [100, 101] and the value in Table 3.9 does not agree with that provided in [99]. One explanation for the deviation of the Cr^{3+} -absorption cross section in Refs. [99, 101] from our values might be that the determination of the impurity content was less precise in these early studies.

Note on Cr-doped LiNbO_3 Another important result is that the spectra of the Cr-doped LiNbO_3 crystals show more absorption bands (Fig. 3.5 and Tab. 3.8) than there are reported from literature [42–44], i.e. the spectra reveal a small absorption band centered at 14550 cm^{-1} for both polarizations. For *e*-wave light there are additional small absorption bands centered at 19300 and 20050 cm^{-1} . Due to the high doping level it is unlikely that these unknown absorption bands originate from other impurities. It is more likely that these absorption bands can also be attributed to Cr. One reason, why these absorption bands have not been reported so far, might be that these bands have very small amplitude with respect to the well-known absorption bands and therefore could not be identified in previous studies. The exact electronic transitions that cause these absorption bands cannot be determined by absorption spectroscopy. Electronic paramagnetic resonance studies may help to reveal the origin of these transitions [52].

3.4 Results and discussion: MgO-doped LiNbO_3 crystals

In this section the results of the absorption measurements with the MgO:LN and the transition-metal codoped MgO:LN crystals will be presented and discussed.

3.4.1 Results

3.4.1.1 MgO-doped LiNbO_3 crystals

Absorption spectra of three 5-mol% MgO-doped LiNbO_3 samples from different boules, i.e. samples MgOLN_1 , $\text{MgOLN}_{\text{Ref,T}}$, and $\text{MgOLN}_{\text{Cube}}$, are shown in Fig. 3.6 for *o*-wave and *e*-wave illumination.

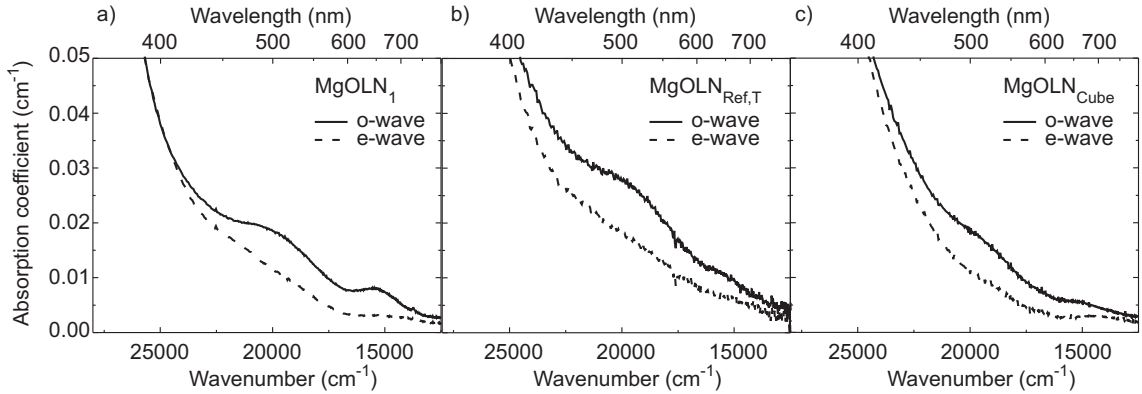


Figure 3.6: Absorption spectra of 5-mol% MgO-doped LiNbO_3 samples from three different boules for *o*-wave (solid line) and *e*-wave light (dashed line).

All three samples show the same characteristic pronounced absorption bands around 20000 cm^{-1} and 15000 cm^{-1} for *o*-wave light. Peaks are less pronounced for *e*-wave illumination. The peak amplitudes of all three samples are in the same absorption range, therefore peak-parameters of the characteristic absorption peaks of sample MgOLN_1 are summarized exemplarily in Tab. 3.10.

There is no significant difference within the accuracy of the measurement between absorption spectra in the visible spectral range from samples MgOLN_1 , MgOLN_2 , MgOLN_3 , and MgOLN_4 , which are cut from the same crystal slab, indicating that the absorbing species is uniformly distributed in the plane normal to the growth direction. Usually commercial wafers are cut from that part of the crystal, i.e. the absorption of different positions in a

Crystal	Polarization	$\tilde{\nu}_0(\text{cm}^{-1})$	$\tilde{\omega}(\text{cm}^{-1})$	A (cm^{-1})
MgO:LN	o-wave	13750	100	0.0006
		15200	660	0.0029
		19000	750	0.0022
		20350	760	0.0023
MgO:LN	e-wave	15050	1000	0.0012
		18800	650	0.0002
		21300	480	<0.0001

Table 3.10: Fit parameters of the absorption bands of sample MgOLN_1 for o- and e-wave illumination. The accuracy for the amplitude A is about 0.0001 cm^{-1} , for $\tilde{\nu}_0$ and $\tilde{\omega}$ the accuracy is about 50 cm^{-1} . The spectral position $\tilde{\nu}_0$ of the narrow peak at 13750 cm^{-1} (o-wave) is determined with an accuracy of 10 cm^{-1} .

single wafer is nearly constant, whereas it may vary between wafers from the same boule. Our measurement method is able to clearly resolve distinct absorption bands as is the case for the CLN absorption spectra.

The axial variation in absorption in boule $\text{MgOLN}_{\text{Ref}}$ is shown in Fig. 3.7.

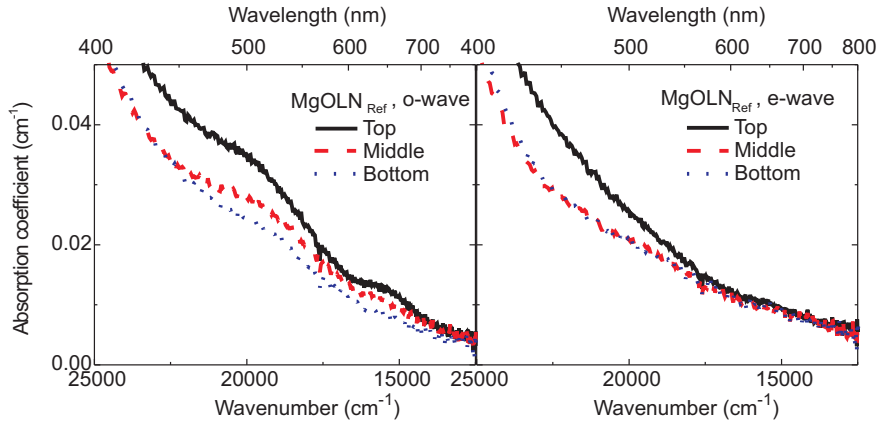


Figure 3.7: Axial absorption variation for reference MgO:LN boule R ($\text{MgOLN}_{\text{Ref}}$) for o-wave (left) and e-wave illumination (right).

Figure 3.7 shows that the characteristic absorption bands decrease from the top to the bottom of the crystal. No new absorption bands are present in the spectra from the

middle and the bottom part of the boule. Note also that the decrease in absorption from the top to the bottom of the boule is more pronounced for *o*-wave than for *e*-wave light.

Again, the accuracy of measurement is too low to reveal absorption peaks in the spectral range 800-2000 nm ($12500\text{-}5000\text{ cm}^{-1}$).

3.4.1.2 $\text{LiNbO}_3:\text{MgO}$ codoped with a transition metal

Spectral range 400–800 nm In Fig. 3.8 the absorption spectra from the top part of the Fe-, Cr-, Cu-, and Ni-codoped $\text{MgO}:\text{LN}$ boules and from the middle part of the Mn-codoped $\text{MgO}:\text{LN}$ boule are shown for *o*- and *e*-wave illumination in the spectral range 400 – 800 nm ($25000\text{ – }12500\text{ cm}^{-1}$).

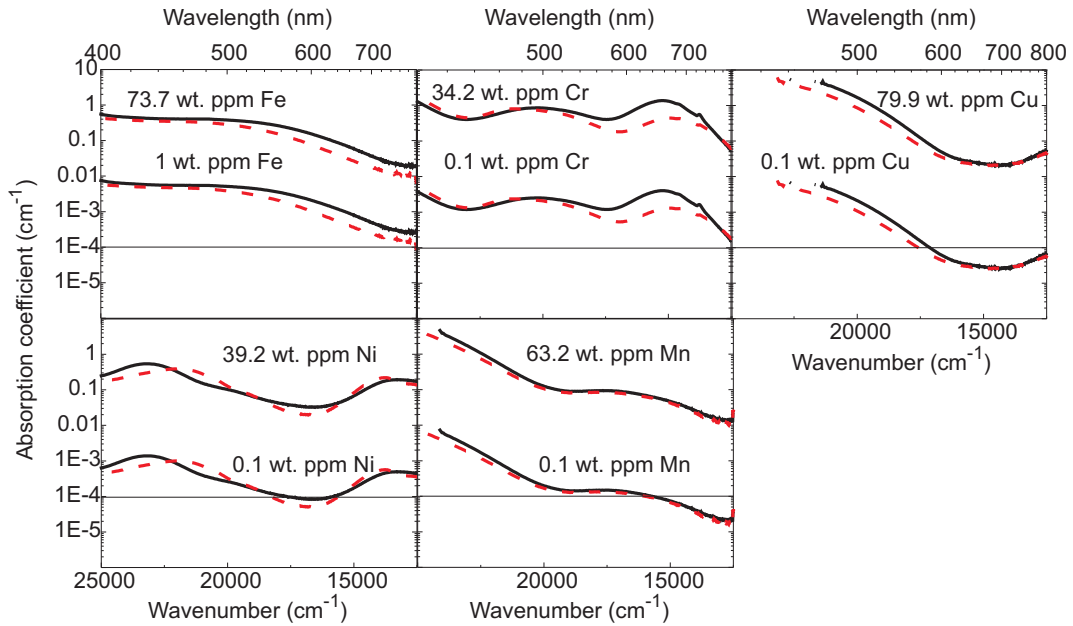


Figure 3.8: Absorption spectra of $\text{MgO}:\text{LN}$ crystals codoped with Fe_2O_3 , Cr_2O_3 , CuO , NiO , and MnO_2 respectively in the range 400 – 800 nm ($25000\text{ – }12500\text{ cm}^{-1}$) for *o*-wave (black solid line) and *e*-wave (red dashed line) illumination. Also shown are spectra scaled to transition-metal impurity levels typical for optical-grade $\text{MgO}:\text{LN}$. The critical absorption level $\alpha = 0.0001\text{ cm}^{-1}$, typical for nonlinear-optical applications, is drawn as a guide to the eye.

Between 350 – 400 nm ($28600\text{ – }25000\text{ cm}^{-1}$) optical absorption is too high to be measured.

In Fig. 3.8 scaled absorption spectra are also shown. They are obtained from the measured absorption spectra by scaling them to dopant levels as they are common in optical grade, nominally impurity-free $\text{MgO}:\text{LN}$ crystals. Here the assumption is made that the valence states of the ions do not change and that the dopant concentration in the melt is the same as in the crystal. Thus distribution coefficients of the dopants are neglected. Especially in the case of the Cr-doped $\text{MgO}:\text{LN}$ crystal this is a significant simplification. The horizontal line represents the absorption level of $\alpha = 0.0001 \text{ cm}^{-1}$. This is a typical level of absorption where thermal lensing can already impact nonlinear-optical applications. Hence Fig. 3.8 shows that impurity concentrations as low as 0.1 wt. ppm cause significant absorption. In Tab. 3.11 peak fit parameters of the measured absorption peaks are listed respectively. Comparison of the peak position in the spectra of Fig. 3.8 and Tab. 3.11 to the spectral positions of absorption peaks in the optical-grade $\text{MgO}:\text{LN}$ crystals in Fig. 3.6 and Tab. 3.10 shows agreement for many absorption peaks, especially with respect to Cr.

With respect to the segregation of the dopants within the crystal boule, measurements show that the amplitudes of the absorption peaks of the Fe- and Ni-codoped $\text{MgO}:\text{LN}$ crystals do not significantly vary from the top to the bottom of the boule ($< 10\%$). In the Mn-codoped $\text{MgO}:\text{LN}$ boule, where the top sample is not available for measurements, there is also no change in absorption measurable from the middle to the bottom of the boule ($< 10\%$). For the Cu-codoped $\text{MgO}:\text{LN}$ boule there is only a slight increase in absorption band amplitude from top to bottom ($\approx 25\%$). In contrast, a significant axial composition variation can be observed for the Cr-codoped $\text{MgO}:\text{LN}$ boule which is shown in detail in Fig. 3.9.

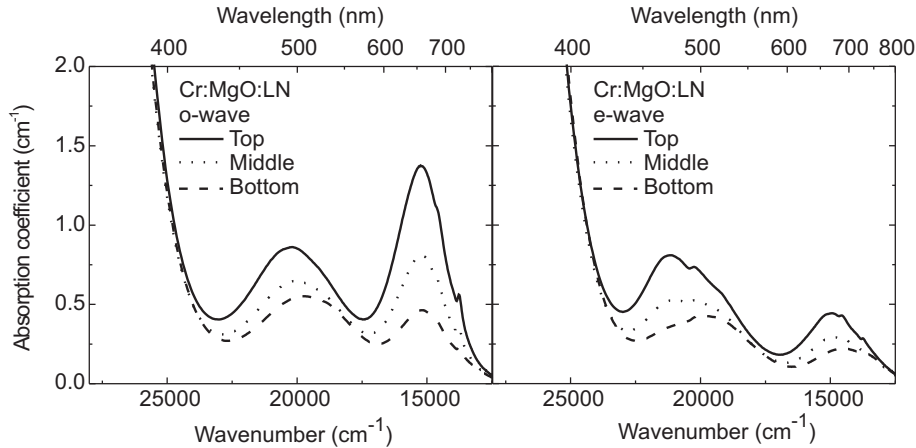


Figure 3.9: Axial absorption variation of the $\text{MgO}:\text{LN}$ boule codoped with 34.2 wt. ppm Cr for o-wave (left) and e-wave illumination (right).

Dopant	wt. ppm	$\tilde{\nu}_0$ (cm^{-1})	\tilde{w} (cm^{-1}) <i>o</i> -wave	A (cm^{-1})	$\tilde{\nu}_0$ (cm^{-1})	\tilde{w} (cm^{-1}) <i>e</i> -wave	A (cm^{-1})
Cr	34.2	13750	50	0.05	13700	200	0.04
		14750	400	0.11	14400	250	0.02
		15300	750	0.92	15000	750	0.27
		18800	650	0.09	19250	500	0.18
		20350	1150	0.49	20000	250	0.09
					21150	950	0.47
Fe	73.7	19650	1700	0.11	20600	1550	0.58
		20750	–	–	–	–	–
Ni	39.2				12200	750	0.08
		13150	1350	0.19	13900	850	0.20
		20000	–	–	19400	–	–
		23150	900	0.38	21900	1300	0.30
Cu	79.9		*		*		
Mn	63.2	17300	1800	0.05	17200	1800	0.05
			*			*	

Table 3.11: Peak fit parameters of the absorption bands of the transition-metal-codoped $\text{MgO}:\text{LN}$ crystals from the top part of respective boules for *o*- and *e*-wave light in the visible spectral range. Entries filled with "–" indicate that a fit is not possible, because respective peaks are not resolved well, i.e. $\alpha < 0.01 \text{ cm}^{-1}$. In this case $\tilde{\nu}_0$ is the position of the local maximum. Rows marked with * indicate that the absorption band merges with the UV absorption edge, hence no peak parameters can be fitted. The accuracy for A is about 0.01 cm^{-1} , for $\tilde{\nu}_0$ and \tilde{w} the accuracy is about 50 cm^{-1} . Again, the accuracy of $\tilde{\nu}_0$ of peaks with $w < 200 \text{ cm}^{-1}$ is about 10 cm^{-1} .

Figure 3.9 shows that for the Cr-doped $\text{MgO}:\text{LN}$ boule some absorption bands do not only decrease from top to bottom by up to factor of three, but different absorption bands change their amplitudes differently from top to bottom, e.g. resulting in a red-shift of the combined absorption band between $400 - 550 \text{ nm}$ ($25000 - 18200 \text{ cm}^{-1}$). This is different from the spectra of Cr-doped LiNbO_3 shown in Fig. 3.5.

Spectral range 800–2000 nm The absorption spectra of the transition-metal codoped $\text{MgO}:\text{LN}$ crystals between 800 – 2000 nm ($5000 - 12500 \text{ cm}^{-1}$) are shown in Fig. 3.10.

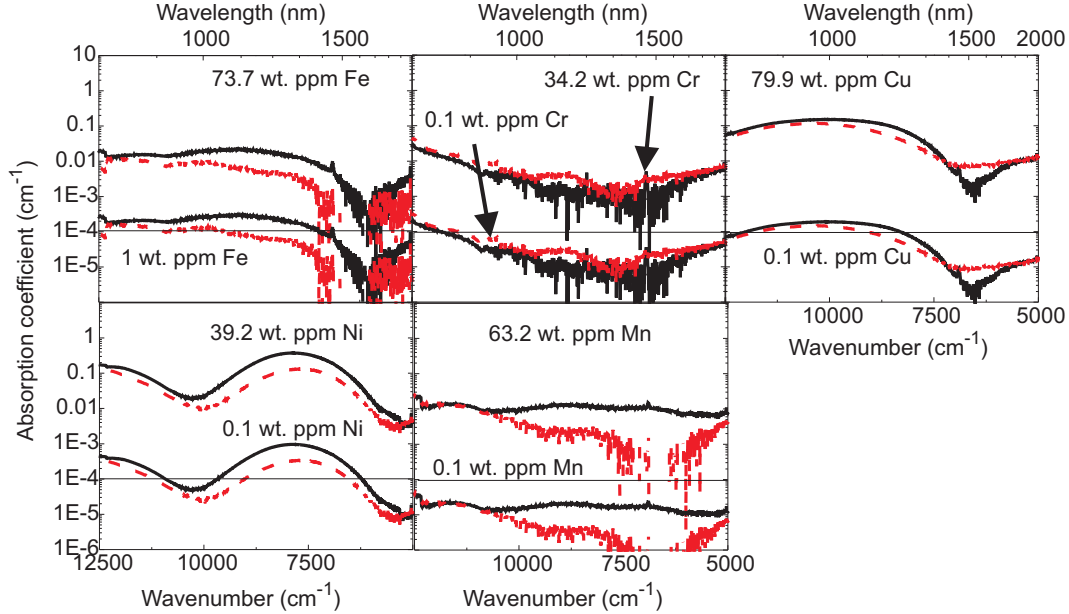


Figure 3.10: Absorption spectra of $\text{MgO}:\text{LN}$ crystals codoped with Fe_2O_3 , Cr_2O_3 , CuO , NiO , and MnO_2 in the wavelength range 800 – 2000 nm ($12500 - 5000 \text{ cm}^{-1}$) for *o*-wave (black solid line) and *e*-wave (red dashed line) illumination. Also shown are spectra scaled to transition-metal impurity levels typical for optical-grade $\text{MgO}:\text{LN}$. The critical absorption level $\alpha = 0.0001 \text{ cm}^{-1}$ is again drawn as a guide to the eye.

Here measurements are feasible because the doping level is high enough to measure absorption bands, although the measurement accuracy is smaller than in the visible range as mentioned in Tab. 3.1. The absorption peak parameters of the absorption bands are listed in Tab. 3.12. Scaling of the absorption spectra of the intentionally transition-metal codoped $\text{MgO}:\text{LN}$ crystals to impurity doping levels found in optical-grade $\text{MgO}:\text{LN}$ is also performed and shown in Fig. 3.10. The scaled curves in Fig. 3.10 show that only $\text{MgO}:\text{LN}$ crystals codoped with Fe, Cu, or Ni respectively have significant absorption bands in this spectral range with $\alpha > 0.0001 \text{ cm}^{-1}$.

Dopant	wt. ppm	$\tilde{\nu}_0$ (cm^{-1})	$\tilde{\omega}$ (cm^{-1}) <i>o-wave</i>	A (cm^{-1})	$\tilde{\nu}_0$ (cm^{-1})	$\tilde{\omega}$ (cm^{-1}) <i>e-wave</i>	A (cm^{-1})
Fe	73.7	9250	1850	0.03	–	–	–
Ni	39.2	7850	800	0.37	7750	750	0.12
Cu	79.9	10200	1550	0.16	10450	1400	0.11

Table 3.12: Peak fit parameters of the absorption bands of the transition-metal-codoped $\text{MgO}:\text{LN}$ crystals from the top part of the boule for *o*- and *e*-wave light in the spectral range 800–2000 nm (12500–5000 cm^{-1}). Entries filled with "–" indicate that a fit is not possible because respective peaks are not resolved well, i.e. $\alpha < 0.01 \text{ cm}^{-1}$. The accuracy for A is about 0.01 cm^{-1} , for $\tilde{\nu}_0$ and $\tilde{\omega}$ the accuracy is about 50 cm^{-1} .

3.4.2 Discussion

The measured absorption spectra of the optical-grade MgO:LN crystals reveal distinct absorption bands, similar to the CLN crystals. In the following, the MgO:LN absorption spectra will be discussed in detail and compared to the measured absorption spectra of the transition-metal codoped MgO:LN crystals.

3.4.2.1 Identification of impurities in MgO-doped LiNbO_3 crystals

The first thing to note is that the absorption spectra and the levels of absorption of all tested MgO:LN boules depicted in Fig. 3.6 are very similar to the absorption spectra and levels of absorption of the CLN samples shown in Fig. 3.4, and that the same impurities occur in the MgO:LN crystals as in the CLN crystals (compare Tab. 3.3 to Tab. 3.5). Fig. 3.6 shows that the main absorption features are the same in all three boules although absolute absorption coefficients slightly differ from each other. The different absorption peak amplitudes might be caused by different impurity concentrations. However, note that the higher level of absorption in sample $\text{MgOLN}_{\text{ref,T}}$ compared to the ones in samples MgOLN_1 and $\text{MgOLN}_{\text{Cube}}$ might also be caused by the imperfect surface polish which increases scattering losses with decreasing wavelength due to Rayleigh scattering, for which the intensity of scattered light is proportional to $1/\lambda^4$. This might also explain why the UV absorption edge seems to be shifted to longer wavelengths in sample $\text{MgOLN}_{\text{ref,T}}$ compared to samples MgOLN_1 and $\text{MgOLN}_{\text{Cube}}$.

Chromium As is the case for CLN crystals, Cr also causes the characteristic absorption peaks in the MgO:LN crystals. Fits of the *o*-wave absorption peaks in the spectrum of sample MgOLN_1 (Fig. 3.6a) yield a pronounced absorption peak centered at 15200 cm^{-1} and a second absorption band that is composed of two absorption peaks centered at 19000 and 20350 cm^{-1} (Tab. 3.10). These peak positions are consistent with the absorption spectra of the Cr-codoped MgO:LN crystals (Fig. 3.9 and Tab. 3.11). A similar observation is valid for *e*-wave illumination. Furthermore, the observed absorption peak positions are consistent with Cr^{3+} absorption bands reported in literature [43]. Especially the small and narrow peak at 13750 cm^{-1} in the *o*-wave spectrum of sample MgOLN_1 (Fig. 3.6a) is characteristic for Cr^{3+} [43]. However, due to a limited resolution of measurement, it is not possible to determine if there is an effective red shift of the absorption bands from top to bottom of the reference MgO:LN boule R (Fig. 3.7) as is the case in the spectra of the Cr-codoped MgO:LN boule (Fig. 3.9) and which is also reported from the literature [43].

The segregation of impurities can only be studied for the reference MgO:LN boule R (Fig. 3.7). One can clearly see that the characteristic absorption peaks decrease for both polarizations from the top to the bottom of the boule. This is also the case for the inten-

tionally Cr-codoped MgO:LN boule (Fig. 3.9) and the Cr-doped LiNbO_3 boule (Fig. 3.5). However, Fig. 3.7 also shows that the UV-absorption edge in the sample from the top rises much more steeply than in the samples from the middle and the bottom of the crystal. This might also be an artifact due to light scattering centers, because the surface polish of samples cut from MgO:LN boule R is not as good as for the other samples as mentioned in Sect. 3.2.2.

Finally, note that there is an additional small peak centered at 14750 cm^{-1} in the *o*- and *e*-wave absorption spectra of the Cr-codoped MgO:LN crystal. As is the case for the Cr-doped LiNbO_3 crystal this peak has not been reported in the literature so far. Another unknown peak is centered at 20000 cm^{-1} in the *e*-wave spectra of the Cr-codoped MgO:LN crystal.

Iron, nickel, copper, and manganese Figures. 3.9 and 3.7 show that an underlying absorption shoulder on the order of 0.01 cm^{-1} is present besides the characteristic peaks, which cannot solely be attributed to the UV absorption edge due to its sharp bend at 22500 cm^{-1} . It is likely that Fe, Cu, Ni, and Mn impurities contribute to this shoulder as is the case for CLN. The spectra of the MgO:LN crystals codoped with either Fe, Cu, Ni, or Mn in Fig. 3.8 show that these impurities strongly absorb in the visible range, especially between $25000 - 20000\text{ cm}^{-1}$ ($400 - 500\text{ nm}$) which can be disturbing for high-power applications.

Superposition of scaled absorption spectra Scaled absorption spectra in Fig. 3.8 show that impurity concentrations of Fe, Cr, Cu, Ni, or Mn as small as 0.1 wt. ppm most likely cause absorption levels larger than $\alpha > 0.0001\text{ cm}^{-1}$. However, note that the transition metal impurities Fe, Cu, and Mn (denoted as TM) are incorporated into LiNbO_3 in multiple valence states and the concentration ratio $c_{\text{TM}^x}/c_{\text{TM}^{x+1}}$ for different valence states might change from high doping levels to very small doping levels. So the scaled spectra might not perfectly reflect the real absorption spectrum, but they provide an estimate how pronounced absorption peaks might be. The scaled spectra are a good reference for the absorption in MgO:LN where standard absorption measurements are reaching their measurement resolution limits, especially for Ni and Cr ions, which are only incorporated into LiNbO_3 and MgO:LN in one single valence state, i.e. Cr^{3+} and Ni^{2+} .

In Fig. 3.11 it is shown that a superposition of scaled absorption spectra of the various dopants matches the measured *o*- and *e*-wave absorption spectra of sample MgOLN₁ well between $400 - 800\text{ nm}$ ($25000 - 12500\text{ cm}^{-1}$). The scaling is performed in analogy to the scaling procedure shown in Fig. 3.8 by using the following dopant concentrations: 0.1 wt. ppm Cu, 1.5 wt. ppm Fe, 0.1 wt. ppm Cr, 0.1 wt. ppm Ni, and 0.05 wt. ppm Mn. Then the resulting scaled spectra are superposed. The scaling procedure is not valid in

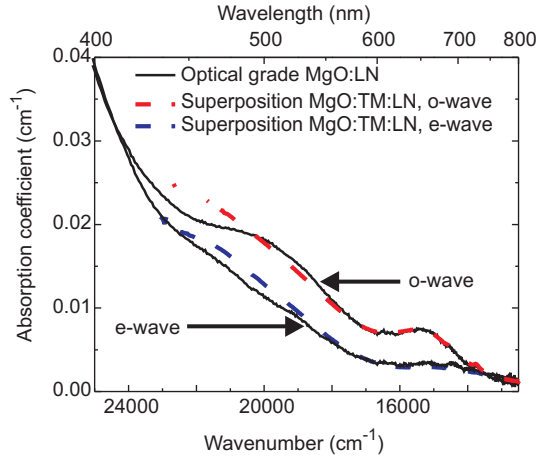


Figure 3.11: Superposition of scaled absorption spectra of Fe-, Cr-, Cu, Ni- or Mn-codoped LiNbO_3 . Scaling is performed to represent the following concentrations: 0.1 wt. ppm Cu, 1.5 wt. ppm Fe, 0.1 wt. ppm Cr, 0.1 wt. ppm Ni, 0.05 wt. ppm Mn. Also shown are the o- and e-wave absorption spectra of sample MgOLN_1 .

the spectral region 400 – 376 nm ($21000 - 25000 \text{ cm}^{-1}$) because absorption is too high to be measured in the MgO:LN crystals codoped with Mn or Cu, as is shown in Fig. 3.8. Note that the Fe-concentration of 1.5 wt. ppm is slightly larger than the maximum Fe concentration that the optical-grade MgO:LN crystals are specified for in Tab. 3.5, however the concentration ratio $c_{\text{Fe}^{2+}}/c_{\text{Fe}^{3+}}$ in optical-grade MgO:LN is probably not exactly the same as the one in Fe-codoped MgO:LN, and only Fe^{2+} causes significant absorption. So it might be that a total Fe concentration smaller than 1.5 wt. ppm yields the same absorption spectrum.

Near-infrared spectral range In previous sections it was shown that Fe, Cr, Cu, Ni, and Mn cause the residual optical absorption in MgO:LN in the visible. In the near-IR spectral range between $5000 - 12500 \text{ cm}^{-1}$ no absorption bands can be measured in MgO:LN due to the limited measurement accuracy. Nevertheless, absorption spectra of the transition-metal codoped MgO:LN crystals in Fig. 3.10 show that Fe, Cr, and Ni impurities absorb in this spectral range. Furthermore, these spectra show that impurity concentrations of less than 1 wt. ppm for Fe and less than 0.1 wt. ppm for Ni and Cu cause absorption bands with amplitudes A larger than 0.0001 cm^{-1} , e.g. for Ni the peak amplitude is on the order of $A = 0.001 \text{ cm}^{-1}$ at $\tilde{\nu}_0 = 7850 \text{ cm}^{-1}$ for o-wave light and $A = 0.0003 \text{ cm}^{-1}$ at $\tilde{\nu}_0 = 7750 \text{ cm}^{-1}$ for e-wave light.

3.5 Comparison: Congruent LiNbO_3 vs. MgO-doped LiNbO_3

In CLN and MgO:LN chromium impurities mainly cause the characteristic absorption bands in the visible together with contributions from Fe, Cu, Ni, and, to a small extent, Mn. The main absorption peak amplitudes are on the order of $0.001 - 0.01 \text{ cm}^{-1}$. Contributions from polarons can be neglected for both, CLN and MgO:LN crystals. In the spectral range $12500 - 5000 \text{ cm}^{-1}$ (800–2000 nm) Ni plays the key role in MgO:LN with a broad absorption peak centered at 7850 cm^{-1} . Nickel impurities can be present in CLN with concentrations on the order of 0.1 wt. ppm as well (Tab. 3.3). Absorption spectra of Ni-doped LiNbO_3 crystals [47] show similar absorption bands and absorption cross sections as the bands seen in Ni-codoped MgO:LN in Figs. 3.8 and 3.10 [49]. Hence, Ni probably causes similar residual absorption in the spectral range $12500 - 5000 \text{ cm}^{-1}$ (800–2000 nm) as in MgO:LN. Chromium and Ni are incorporated into CLN and MgO:LN in one single valence state, i.e. Cr^{3+} and Ni^{2+} . In contrast, so far research has focused on the multivalent impurities Cu, Fe, and Mn that play a key role in the bulk-photovoltaic process. Other impurities have usually been neglected in analyses because they were believed not to be important for the charge transport processes. Our results show that this assumption no longer holds not only with respect to absorption, e.g. studies have shown that the combination of Fe and Cr in Fe-Cr-codoped LiNbO_3 crystals can even enhance charge transport processes [100]. Nevertheless, the spectra of the transition-metal codoped MgO:LN crystals in Figs. 3.8 and 3.10 also show that absorption cross sections for *e*-wave light are smaller than for *o*-wave light for all five transition metal impurities. This can also be observed in the spectra of the optical-grade CLN and MgO:LN crystals. This knowledge is very important for applications because the nonlinear optical coefficient of CLN and MgO:LN is largest for *e*-wave light, making this polarization the most favorable.

3.6 Outlook and conclusion

Outlook The results of the absorption measurements in the spectral range 350–2000 nm ($28600 - 5000 \text{ cm}^{-1}$) have shown that optical absorption in CLN and MgO:LN crystals is dominated by transition-metal impurities. It is technically extremely challenging to obtain purer starting powders for crystal growth so far. The impurity content already is very low with respect to absolute numbers. Therefore, other approaches have to be pursued in order to reduce absorption. Our results have also shown that the absorption characteristics are the same as in intentionally transition-metal doped crystals with impurity contents that are two orders of magnitude larger than the impurity content in the optical grade CLN and MgO:LN crystals. Absorption measurements in such intentionally doped crystals have a better signal-to-noise ratio, and the effects that post-growth experiments have on absorption are much easier to observe. One promising post-growth process in order to decrease some absorption bands is thermo-electric oxidization, i.e. changing the oxidization state from, e.g. Fe^{2+} to Fe^{3+} by application of an electric field during annealing between $600 - 700 \text{ }^\circ\text{C}$ [102, 103]. Experiments with Fe-doped LiNbO_3 crystals show that the Fe^{2+} absorption peak in the blue can be reduced by more than two orders of magnitude [102, 103]. Frequency doubling experiments in undoped CLN indicate that this oxidization process also works for CLN because PRD is strongly reduced. The inhibition of PRD after processing is an indicator for the oxidization of Fe^{2+} ions [79]. However, absorption spectra have not been determined. Furthermore, thermo-electric oxidization has not been tried with MgO:LN so far. Therefore it would be interesting to measure the absorption in thermo-electrically oxidized CLN and MgO:LN in future experiments. One can expect that those impurities that are incorporated in more than one valence, i.e. Fe, Cu, and Mn, are affected by the thermo-electric oxidization process. Nevertheless, a reduction or oxidization treatment probably cannot fully suppress absorption, because ions are only transformed from one valence state to the other. This means that with the decrease of one absorption band another band might increase. For Fe this is not a problem because Fe^{3+} ions do not significantly absorb photons in the visible, but for, e.g. Cu, this is different. There oxidization could suppress absorption caused by Cu^+ , however absorption bands caused by Cu^{2+} would increase (Tab. 2.2). Anyway, it might still be possible to fabricate CLN or MgO:LN crystals that have low optical absorption in a limited spectral range that is of interest for a particular application.

In the case of impurities that are only incorporated in one single valence state, i.e. Cr and Ni, studies with applied electric fields during growth might be promising. For instance, crystal growth experiments have shown that varying the rate with which a crystal is pulled out of the melt strongly influences Cr impurity incorporation, i.e. the distribution coefficient of Cr increases from one to three by decreasing the pulling rate from 15 mm to 3 mm per hour [98]. The larger the distribution coefficient of an impurity is, the more the crystal

is enriched with the particular impurity in the top part of the crystal and depleted in the bottom part. Interestingly, the distribution coefficient of Cr was even smaller than unity by application of an electric field during growth [98]. In this case Cr prefers to stay in the melt, and thus the top part of the boule will have less Cr incorporated than the bottom. These segregation studies were only performed with Cr as the dopant, but similar studies might also be performed with Ni, Fe, Cu, and Mn. Ideally, segregation of impurities in one part of the boule would allow to use the purified part for low-loss applications. The rest of the boule could be used for applications where optical losses are not critical.

Conclusion In this chapter it was shown that it is feasible to resolve absorption coefficients in CLN and MgO:LN, using a conventional grating spectrophotometer. The measurement accuracy in terms of absorption coefficient was about 0.0001 cm^{-1} between 350 – 800 nm ($28600 - 12500 \text{ cm}^{-1}$), which is an improvement of about two orders of magnitude in comparison to already existing absorption spectroscopy data in literature. The results of the absorption measurements with CLN and MgO:LN crystals showed that Cr causes the characteristic absorption bands in the range 350 – 800 nm together with contributions from Fe, Cu, Ni, and Mn. The observed Cr^{3+} absorption bands between 350 – 800 nm had amplitudes on the order of $0.001 - 0.01 \text{ cm}^{-1}$ for a concentration of 0.5 wt. ppm that is typical for optical grade CLN. In MgO:LN the observed absorption band amplitudes caused by Cr^{3+} were on the order of 0.001 cm^{-1} . The underlying absorption shoulder that merged with the UV-absorption edge was probably caused by Fe, Cu, Ni, and Mn impurities. Absorption spectra of transition-metal codoped MgO:LN crystals in the range 800 – 2000 nm ($12500 - 5000 \text{ cm}^{-1}$) showed that typical Ni concentrations of 0.1 wt. ppm would cause absorption bands with amplitudes on the order of 0.001 cm^{-1} for *o*-wave and 0.0001 cm^{-1} for *e*-wave light. Typical concentrations of Cu and Fe impurities probably cause absorption bands with amplitudes on the order of 0.0001 cm^{-1} . This spectral range is of special interest for OPO applications because of available pump lasers, and an absorption coefficient exceeding 0.0001 cm^{-1} can already cause thermal lensing.

Chapter 4

Suppression of mid-infrared absorption in congruent LiNbO_3 and $\text{LiNbO}_3\text{:MgO}$ crystals

Optical parametric oscillators have been established as attractive sources of tunable coherent radiation in the mid-IR [104]. The practical range of operation of OPOs has been drastically expanded since highly nonlinear and non-critically phasematched materials such as PPLN crystals became available. This development was of great importance especially for continuous-wave (CW) singly-resonant oscillators (SROs) [104, 105]. Up to now, CW mid-IR SROs have been pumped with light in the spectral range 1000-1100 nm, with resonant wavelengths around 1400-1900 nm. However, pumping a CW SRO in the 1545-1560 nm wavelength range has not been successful so far, although very powerful, narrow-bandwidth, highly tunable pump laser sources are available such as external-cavity-diode lasers (ECDL) in connection with erbium-doped amplifiers (EDFA), delivering 20 and more Watts of optical output power. Note that, because of larger pump wavelengths, the corresponding resonant wavelengths also typically shift into the wavelength range 2500-2700 nm for idler outputs in the 3600-3850 nm wavelength range. A schematic of the proposed CW-SRO setup is shown in Fig. 4.1.

Pumping at the wavelength 1550 nm is of interest for signal processing applications, e.g. to convert the amplitude and phase modulation of a tunable telecom-band pump wave in the 1445-1560 nm range into a long-wavelength idler around 3800 nm. The idler wave can be transmitted through air because of low optical absorption in this spectral range [106]. Successful conversion of a telecom signal at 1550 nm onto a long-wave idler at 3800 nm would be a first step towards building a free-space optical communication system. There have been efforts to build such a CW SRO using 5-mol% MgO-doped PPLN (PPMgOLN) in

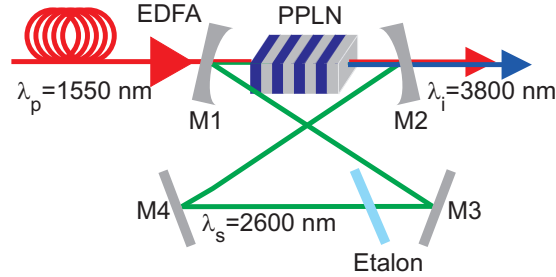


Figure 4.1: Continuous-wave SRO pumped at $\lambda_p = 1550 \text{ nm}$, with the resonant signal wavelength around $\lambda_s = 2600 \text{ nm}$ and the idler wavelength $\lambda_i = 2800 \text{ nm}$. The 1550-nm light is amplified by an erbium-doped amplifier (EDFA) in order to achieve high enough pump intensities. Mirrors M1, M2, M3, and M4 have high reflectivity R for the resonant signal wave ($> 99.9\%$) and high transmission T for the pump and idler waves ($T > 97\%$).

previously published work [107] and in our own laboratories, however these attempts failed because of threshold pump-powers P_{thr} that exceeded the available power of 20 W. One well-known difficulty of CW SROs is that they are very sensitive to optical absorption, especially of the resonant wave, as the threshold pump power P_{thr} is proportional to the total round trip loss in the cavity [92]. Since $P_{\text{thr}} \propto \alpha_s$, where α_s is the absorption coefficient of the resonant signal wavelength, an absorption coefficient in the range of only 0.005 cm^{-1} in a several centimeter long crystal would add significantly to the total loss of a well designed cavity and therefore increase P_{thr} substantially. As mentioned in Sects. 2.2.3.2 and 2.3.1.1, some absorption bands in CLN and MgO:LN are known in the range 2000 – 2900 nm: The OH-vibration peak that is always present in CLN ($\tilde{\nu}_0 = 2870 \text{ nm}$) and MgO:LN crystals ($\tilde{\nu}_0 = 2826 \text{ nm}$) and combined OH-vibration-libration absorption bands that have only been reported from CLN around 2250 nm. Typical OH-vibration peak amplitudes are on the order of 1 cm^{-1} [59], the combined OH-vibration-libration absorption bands in CLN have amplitudes on the order of 0.01 cm^{-1} [57]. There are no absorption bands known so far for CLN and MgO:LN between 2300 – 2800 nm. Measurements in the range 2000–3000 nm with detection limit smaller than $\alpha = 0.01 \text{ cm}^{-1}$ are not reported in literature. Thus, increasing the sensitivity of absorption measurements to about 0.0005 cm^{-1} might reveal so-far unknown absorption bands.

In this chapter we present results of optical absorption measurements in CLN and MgO:LN crystals in the range 2000 – 2950 nm ($5000 - 3390 \text{ cm}^{-1}$). Some MgO:LN and CLN crystals are subject to high-temperature annealing, and absorption spectra of as-grown crystals will be compared to those of the annealed crystals. Finally the annealing process will be evaluated with respect to the above mentioned SRO problem.

4.1 Crystals and measurement method

4.1.1 Crystals

The CLN and MgO:LN samples used in the experiments are provided by Crystal Technology, Inc. A complete list of samples is presented in Tab. 4.1.

Crystal	Position in boule	Dimensions $x \times y \times z$ (mm ³)	Process	T_{anneal} (°C)	Short name
MgO:LN	Center	$25 \times 15 \times 20$	as-grown	–	MgOLN _G
MgO:LN	Center	$25 \times 15 \times 20$	annealing	1050	MgOLN _A
CLN	Top	$20 \times 20 \times 20$	as-grown	–	CLN _{Top,G}
CLN	Top	$20 \times 20 \times 20$	annealing	1000	CLN _{Top,A}
CLN	Bottom	$20 \times 20 \times 20$	as-grown	–	CLN _{Bottom,G}
CLN	Bottom	$20 \times 20 \times 20$	annealing	1000	CLN _{Bottom,A}

Table 4.1: *Undoped CLN and MgO:LN samples used in the infrared absorption experiments. The annealing temperature is denoted with T_{anneal} . Entries marked with "-" denote crystals that are not annealed.*

Some of the MgO:LN and CLN crystals used in this study are subject to a post-growth annealing process performed by Crystal Technology, Inc. Those unpolished CLN and MgO:LN samples are annealed at 1000 °C and 1050 °C respectively in a dry oxygen atmosphere for 24 hours. The purpose of the annealing step is to diffuse hydrogen out of the crystal [108]. After annealing, back at room temperature, the diffusion coefficient of hydrogen is too low for significant incorporation back into the crystal, and the crystals are permanently reduced in hydrogen content [108].

Two MgO:LN crystal pieces are cut from the center slab of one MgO:LN boule, but only one sample is subject to the high-temperature annealing process. Thus one can expect that both samples have about the same initial concentration of impurities and the same optical absorption spectrum in the as-grown state (as it was already seen in Sect. 3.2.2). Due to the annealing procedure that is applied to sample MgOLN_A it is thus possible to evaluate the annealing effect by comparison of the resulting absorption spectra to the spectra from the as-grown sample MgOLN_G. The same applies to the CLN samples. There two CLN samples are cut from the top part (15% solidified melt fraction) of a CLN boule and two sample are cut from the bottom part (70% solidified melt fraction) of that boule. Note also that the x -surfaces of every crystal used in this study are polished to high optical quality.

4.1.2 Measurement method

Absorption measurements are performed as already described in Sect. 3.1. However, it is important to note, that the purge with dried air is crucial for absorption spectroscopy in this spectral range due to pronounced absorption bands of the ambient, undried air that would overlap with the absorption spectrum of the crystal [106]. But even though dried air is used for purging, problems can occur due the sensitivity of the measurements and the high optical absorption of air in this spectral range. Thus absorption measurements require extreme caution to keep measurement conditions, especially air flow, stable so that the baseline correction is valid. Therefore, in order to check for any baseline drift, a final measurement without any samples inside the compartment is also performed. If this measurement shows a flat zero-line in terms of optical density within an accuracy of $OD = 0.0001$, the measurements performed previously using the same baseline can be further evaluated. In contrast, if the result deviates by more than $OD = 0.0001$, previous measurements using the same baseline are rejected.

4.2 Experimental results

4.2.1 Infrared absorption spectra of MgO-doped LiNbO_3 crystals

In Fig. 4.2 the absorption spectra of the as-grown and annealed MgO:LN samples, i.e. samples MgOLN_G and MgOLN_A , are shown for *o*-wave (left) and *e*-wave (right) light.

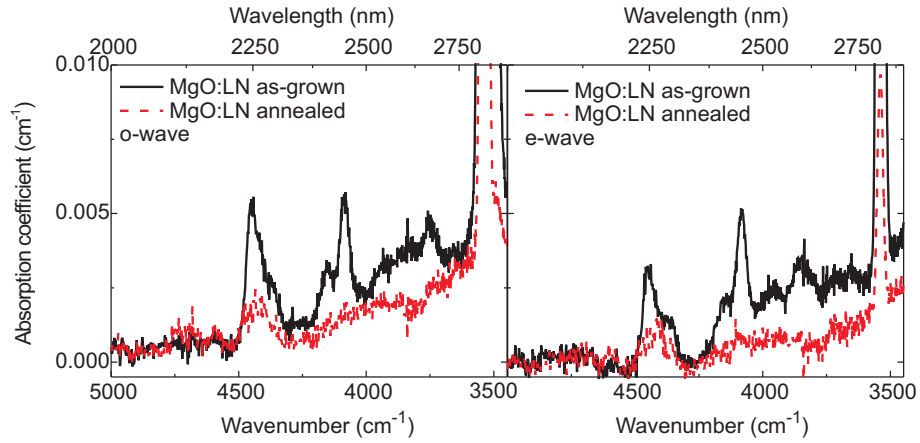


Figure 4.2: Absorption spectra of as-grown MgO:LN (black solid line) and annealed MgO:LN (red dashed line) for *o*-wave (left) and *e*-wave (right) light in the spectral range $5000 - 3390 \text{ cm}^{-1}$ ($2000 - 2950 \text{ nm}$).

Figure 4.2 shows that besides the well known OH-vibration band, broad absorption bands between $4000 - 3570 \text{ cm}^{-1}$ ($2500 - 2800 \text{ nm}$) can be determined for the as-grown sample MgOLN_G . The magnitude of the absorption coefficient is similar for ordinary and extraordinary light polarization within these absorption bands, however the wavelength dependence is somewhat shifted for the two polarizations. Due to the limited resolution it is not clear how many distinct absorption peaks the entire absorption band is built of, thus it is not possible to fit Gaussian peaks to these absorption bands. In contrast, there are further more pronounced absorption bands in the spectral range $5000 - 4000 \text{ cm}^{-1}$ ($2000 - 2500 \text{ nm}$) where Gaussian fits can be applied. The fit results are summarized in Tab. 4.2 for the as-grown sample MgOLN_G .

Figure 4.2 also shows that absorption is decreased by up to one order of magnitude in the annealed sample in comparison to that of the as-grown sample. Some absorption peaks even vanish within the accuracy of measurement in the case of the annealed sample. Note that the small negative absorption coefficients in Fig. 4.2 can easily be explained by an imperfect Fresnel correction due to uncertainties in the angle of the incident light,

Crystal	$\tilde{\nu}_0(\text{cm}^{-1})$	$\tilde{\omega}(\text{cm}^{-1})$	A (cm^{-1})
MgO:LN: <i>o</i> -wave	4083	26	0.0038
	4158	19	0.0017
	4367	18	0.0012
	4422	21	0.0027
	4455	13	0.0031
MgO:LN: <i>e</i> -wave	4081	31	0.0045
	4164	26	0.0017
	4358	18	0.0012
	4415	27	0.0017
	4454	17	0.0025

Table 4.2: Spectral positions of the absorption peaks of sample MgOLN_G for *o*- and *e*-wave light in the spectral range $5000 - 4000 \text{ cm}^{-1}$ ($2000 - 2500 \text{ nm}$). The accuracy for the peak amplitude A is about 0.0001 cm^{-1} , the accuracy for $\tilde{\nu}_0$ and $\tilde{\omega}$ is about 1 cm^{-1} respectively.

thickness of the sample, and surface scattering which lead to an offset. The shape of the graph is unaffected by these errors within the measurement accuracy which is about $\Delta\alpha = 0.0005 \text{ cm}^{-1}$.

The well-known OH-vibration peak at 3538 cm^{-1} (2826 nm) is plotted separately in Fig. 4.3 for both polarizations because the amplitudes exceed the scale in Fig. 4.2. Furthermore, since the OH-vibration peak amplitude and its peak area are a measure for the hydrogen content [56], the OH-vibration peak amplitude and peak area are determined with Gaussian peak fits for the as-grown and the annealed MgO:LN sample. The fit results are summarized in Tab. 4.3.

From Tab. 4.3 it can be seen that annealing decreases the OH-vibration peak of MgO:LN by an order of magnitude for both polarizations.

Alternative absorption measurement scheme and results An additional measurement procedure is pursued in order to find the reason for the gradually increasing slope in Fig. 4.2 between $4170 - 3450 \text{ cm}^{-1}$ ($2400 - 2900 \text{ nm}$) for the as-grown and the annealed sample. The measurement setup is the same as depicted in Fig. 3.1, but the measurement procedure is slightly changed: Instead of measuring the baseline with no sample in either the signal arm nor the reference arm, the baseline is measured with the annealed sample MgOLN_A in the signal compartment for *o*-wave light first. Then the actual measurement with *o*-wave light is performed with the as-grown sample MgOLN_G in the signal arm.

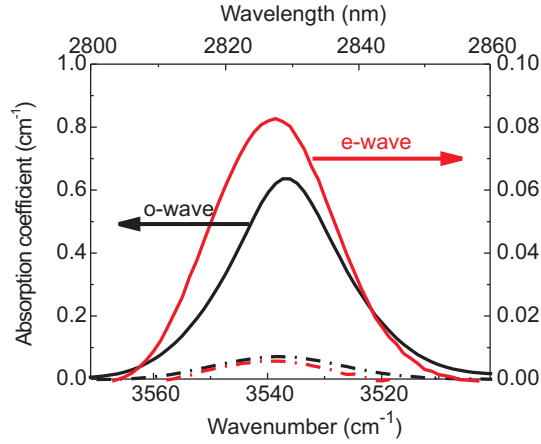


Figure 4.3: *OH-vibration peaks of as-grown MgO:LN (solid lines) and annealed MgO:LN (dash-dotted lines) for o- (black, left axis applies) and e-wave (red, right axis applies) light. Note the different scales for o- and e-wave light.*

Polarization	Crystal	$\tilde{\nu}_0(\text{cm}^{-1})$	$\tilde{\omega}(\text{cm}^{-1})$	A (cm^{-1})	Area (cm^{-2})
o-wave	as-grown	3536	10	0.60	15.2
	annealed	3538	11	0.07	2.0
e-wave	as-grown	3539	11	0.085	2.3
	annealed	3539	11	0.008	0.2

Table 4.3: *Impact of annealing on the OH-vibration peak in MgO:LN. Summarized are fit parameters, including the peak area, of the OH-vibration peak for o- and e-wave light. For o-wave light the accuracy of the peak amplitude A is about 0.01 cm^{-1} , for e-wave light it is 0.001 cm^{-1} . For both polarizations the accuracy for $\tilde{\nu}_0$ and $\tilde{\omega}$ is about 1 cm^{-1} respectively, and for the peak area it is 0.1 cm^{-2} .*

Thus the difference in absorption between samples MgOLN_A and MgOLN_G is measured. Finally a measurement is taken with sample MgOLN_A in the signal arm again. This final measurement is supposed to deliver a flat spectrum, ensuring that there was no baseline drift or change in the measurement chamber during the main absorption difference measurement with sample MgOLN_G . Then the entire measurement procedure, including the baseline measurement, is repeated for e-wave light. The advantage of this measurement procedure is, that it directly measures the change in optical transmission between the as-grown and the annealed crystal without the need to correct for Fresnel-reflection losses, i.e.

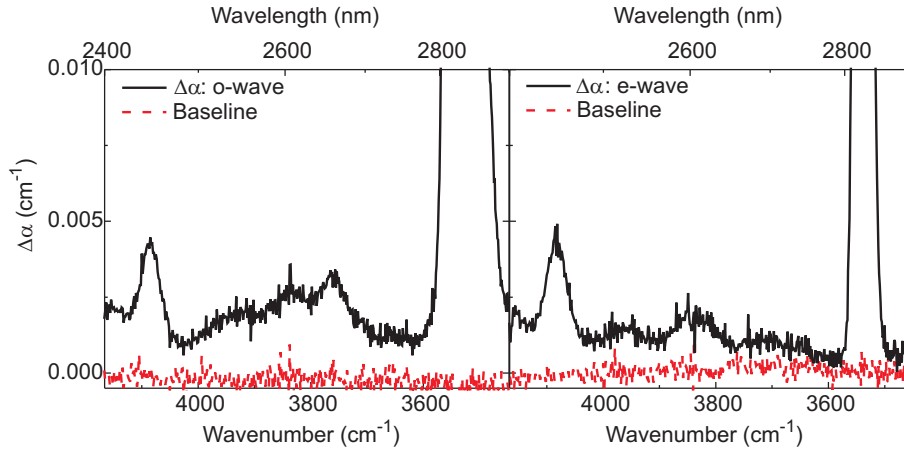


Figure 4.4: Difference absorption spectrum $\Delta\alpha$ of as-grown MgO:LN vs. annealed MgO:LN (black solid line) for o -wave (left graph) and e -wave (right graph) light. The measurement with the annealed sample MgOLN_A yields flat lines (red dashed line) for both polarizations.

without knowledge of the correct Sellmeier equation. But note also that this measurement scheme is only valid because we can assume that the Fresnel reflections are the same for both MgO:LN samples and that the dimensions and quality of the surface polish are the same for both samples within the accuracy of the measurement. The disadvantage is that this measurement procedure only measures changes in optical absorption and not absolute absorption coefficients. The results are depicted in Fig. 4.4 for o -wave (left) and e -wave illumination (right) between $4170 - 3450 \text{ cm}^{-1}$ ($2400 - 2900 \text{ nm}$). This is the spectral range where the underlying slope is most pronounced in Fig. 4.2.

In Fig. 4.4 the difference spectra between the as-grown and the annealed sample (black solid line) show the same characteristic absorption bands for both polarizations as the absorption bands in the spectra of the absolute measurements in Fig. 4.2, however, the difference spectra do not exhibit the slope that is present in the spectra of the absolute absorption measurements. Furthermore, the difference measurement with the annealed sample yields a flat line (red dashed line) for both polarizations indicating that the baseline correction is valid.

4.2.2 Infrared absorption spectra of congruent LiNbO_3 crystals

In Fig. 4.5 the absorption spectra of an as-grown CLN crystal (sample $\text{CLN}_{\text{Bottom,G}}$, black solid line) and an annealed CLN crystal (sample $\text{CLN}_{\text{Bottom,A}}$, red dashed line) are shown

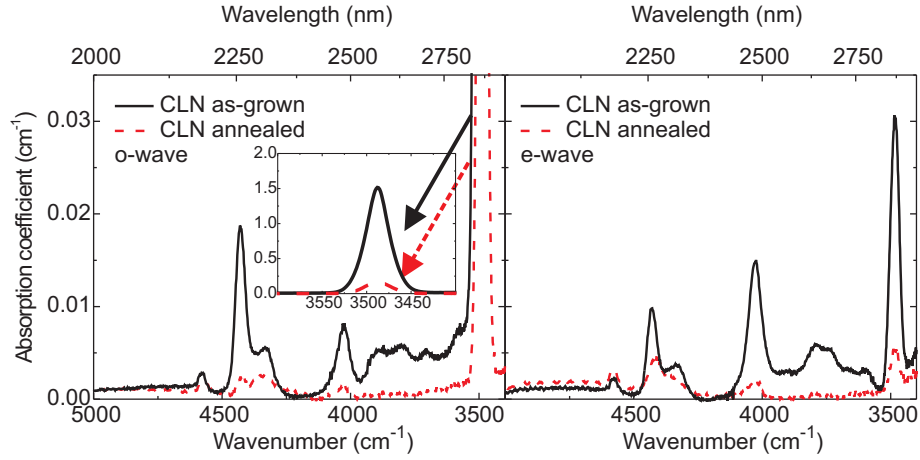


Figure 4.5: Optical spectrum of as-grown CLN (sample $\text{CLN}_{\text{Bottom,G}}$, black solid line) and annealed CLN ($\text{CLN}_{\text{Bottom,A}}$, red dashed line) for *o*- (left) and *e*-wave (right) in the spectral range $5000 - 3390 \text{ cm}^{-1}$ ($2000 - 2950 \text{ nm}$). The inset shows the OH-vibration peaks of the as-grown and the annealed sample for *o*-wave light.

for *o*-wave (left graph) and *e*-wave light (right graph). Note that there is no difference in the absorption spectra in this spectral range between as-grown CLN samples from the top and the bottom of the boule ($\text{CLN}_{\text{Top,G}}$ and $\text{CLN}_{\text{Bottom,G}}$) within the accuracy of measurement. The same observation applies to the annealed CLN samples $\text{CLN}_{\text{Top,A}}$ and $\text{CLN}_{\text{Bottom,A}}$.

There are absorption bands between $4000 - 3570 \text{ cm}^{-1}$ ($2500 - 2800 \text{ nm}$) that are similar to the absorption bands observed in the as-grown $\text{MgO}:\text{LN}$ crystal. The magnitude of the absorption coefficient is again similar between ordinary and extraordinary light polarization within these absorption bands, but the wavelength dependence is also somewhat shifted for the two polarizations. As for the case of $\text{MgO}:\text{LN}$ it is not clear how many separate peaks the bands are built of. Further pronounced absorption bands can be found in the spectral range $5000 - 4000 \text{ cm}^{-1}$ ($2000 - 2500 \text{ nm}$) as well. For these peaks Gaussian fits can be applied similar to the absorption spectra of $\text{MgO}:\text{LN}$. The peak fit results for the as-grown sample $\text{CLN}_{\text{Bottom,G}}$ are summarized in Tab. 4.4.

As mentioned in Sect. 2.2.3.2, the OH-absorption peak in CLN is a combination of several absorption peaks due to the fact that hydrogen impurities on different sites have slightly different OH-stretch-vibration frequencies. Similar behavior has been reported from studies with stoichiometric crystals where the peak widths are narrower [59]. However, we are only interested in the envelope of these OH-vibration bands that appear to be one single peak. A Gaussian fit describes this OH-vibration peak envelope very well for the crystals

Crystal	$\tilde{\nu}_0(\text{cm}^{-1})$	$\tilde{\omega}(\text{cm}^{-1})$	A (cm^{-1})
CLN: <i>o</i> -wave	4028	29	0.0069
	4345	39	0.0052
	4429	19	0.0174
	4581	21	0.0017
CLN: <i>e</i> -wave	4026	30	0.0138
	4344	36	0.0035
	4428	19	0.0092
	4579	24	0.0017

Table 4.4: Spectral positions of the absorption peaks of sample $\text{CLN}_{\text{Bottom,G}}$ for *o*- and *e*-wave light in the spectral range $5000\text{-}4000\text{ cm}^{-1}$. The fit accuracy for the peak amplitude A is about 0.0001 cm^{-1} , the accuracy for $\tilde{\nu}_0$ and $\tilde{\omega}$ is about 1 cm^{-1} respectively.

used in this study. The fit results are summarized in Tab. 4.5.

Polarization	Crystal	$\tilde{\nu}_0(\text{cm}^{-1})$	$\tilde{\omega}(\text{cm}^{-1})$	A (cm^{-1})	Area (cm^{-2})
<i>o</i> -wave	as-grown	3488	13	1.42	47.5
	annealed	3487	15	0.16	5.8
<i>e</i> -wave	as-grown	3484	17	0.029	2.3
	annealed	3482	18	0.004	0.2

Table 4.5: Impact of annealing on the *OH*-vibration peak in CLN. Summarized are fit parameters, including the peak area, of the *OH*-vibration peak for *o*-wave and *e*-wave light. With respect to *o*-wave light the fit accuracy of A is about 0.01 cm^{-1} , with respect to *e*-wave light it is 0.001 cm^{-1} . For both polarizations the accuracy for $\tilde{\nu}_0$ and $\tilde{\omega}$ is about 1 cm^{-1} respectively, and for the peak area it is 0.1 cm^{-2} .

Figure 4.5 and Tab. 4.4 show that annealing efficiently suppresses absorption in the same way as is the case for $\text{MgO}:\text{LN}$. The maximum decrease in absorption is about one order of magnitude.

4.3 Discussion

As mentioned in Sect. 4.2.2, the absorption spectra from the top part of the CLN boules coincide with the spectra of the bottom of the CLN boules between $5000 - 3390 \text{ cm}^{-1}$ ($2000 - 2950 \text{ nm}$). This indicates that there is no axial change in absorption and that the dominating, optically active impurities are evenly distributed in the crystal boules. This is also observed for the annealed samples from the top and the bottom of the CLN boules, indicating that annealing also homogeneously affects the crystal.

Identification of absorption bands in as-grown CLN and as-grown MgO:LN

Other than the well-known OH-vibration peaks in CLN and MgO:LN only the peak centered at 4429 cm^{-1} in the *o*- and *e*-wave spectra of CLN can be identified with spectral features in the literature. It is a combined OH-vibration-libration peak [62]. The corresponding peak in the *o*- and *e*-wave spectra of MgO:LN around 4455 cm^{-1} can probably also be attributed to OH-vibration-librations due to the isomorphic crystal structure and due to the fact that the spectral features are very similar in CLN, but only slightly shifted to longer wavelengths. However, there is no reference in the literature reporting the other absorption peaks in the range $4350 - 4000 \text{ cm}^{-1}$ ($2300 - 2500 \text{ nm}$) and the broader absorption bands in the range $4000 - 3570 \text{ cm}^{-1}$ ($2500 - 2800 \text{ nm}$) for either CLN or MgO:LN.

Comparison of absorption between as-grown CLN and as-grown MgO:LN

Tables 4.3 and 4.5 show that the amplitudes of the absorption peaks between $5000 - 3570 \text{ cm}^{-1}$ ($2000 - 2800 \text{ nm}$) do only weakly depend on light polarization, while the OH-vibration peak for MgO:LN is about 8 times larger for ordinarily than for extraordinarily polarized light. In the case of CLN the OH-vibration peak is even more strongly polarized; there the peak for *o*-wave light is about 50 times larger than the one for *e*-wave light. In this context it is important to note that the absorption peak in CLN centered at $\tilde{\nu} = 4028 \text{ cm}^{-1}$ is about two times larger for *e*-wave than for *o*-wave light. The main difference between as-grown CLN and MgO:LN is that all absorption bands in CLN for both, ordinarily and extraordinarily polarized light, are shifted by about $\Delta\tilde{\nu} \approx 48 \text{ cm}^{-1}$ ($\Delta\lambda \approx 40 \text{ nm}$) to longer wavelengths with respect to those in MgO:LN. This shift is similar to the well-known shift of the OH-vibration peak [56].

Effect of annealing on optical absorption in CLN and MgO:LN

Annealing is very effective in reducing the hydrogen content, i.e. in both, CLN and MgO:LN, the respective OH-vibration peak in the spectrum is reduced in terms of peak amplitude and area by about one order of magnitude as is shown in Tabs. 4.2 and 4.4. This shows that the annealing process is very efficient in decreasing the hydrogen content. Note also that the

annealing process described here is performed in a single annealing step without reducing the crystal first. This is different from the well-known two-step annealing process reported from the literature [56,66] and which is described in Sect. 2.2.3.2.

Furthermore, Figs. 4.2 and 4.5 show that absorption in the annealed CLN and MgO:LN samples is generally decreased between $5000 - 3390 \text{ cm}^{-1}$ ($2000 - 2950 \text{ nm}$), so that, e.g. in MgOLN_G the peak structure almost vanishes between $4000 - 3571 \text{ cm}^{-1}$ ($2500 - 2800 \text{ nm}$) and only a small slope in the spectra remains. In CLN there is not even a slope remaining in this range and, e.g. the maximum decrease of absorption between $4000 - 3570 \text{ cm}^{-1}$ ($2500 - 2800 \text{ nm}$) due to annealing is about one order of magnitude, i.e. from $\alpha = 0.005 \text{ cm}^{-1}$ to less than $\alpha = 0.0005 \text{ cm}^{-1}$ which is the limit of the measurement accuracy. Note also that peak positions, in the case they still can be determined, do not shift due to annealing.

With respect to applications such as the discussed CW SRO depicted in Fig. 4.1, it is important to know if the absorption bands completely vanish. Note that, e.g. an absorption coefficient of about 0.005 cm^{-1} in the signal wave of a CW SRO would raise P_{thr} by at least 7 W in typical 1550-nm-pumped OPO configurations. In the case of CLN the absorption indeed decreases to values that are at the limit of the measurement accuracy. In contrast, for MgO:LN a slope in the o - and e -wave spectra remains that is on the order of 0.001 cm^{-1} . The alternative measurements, for which Fresnel corrections are not necessary and which are presented in Fig. 4.4, show the difference in absorption between the as-grown sample MgOLN_G and the annealed sample MgOLN_A for both polarizations. These spectra do not exhibit any slope which shows that annealing does not influence the slope. This shows that either the slope is already present in the spectra of the as-grown MgO:LN crystal and, e.g. might be caused by another so-far unknown impurity, or it is simply a measurement artifact, which is also indicated by the fact that this slope is not present in CLN and, so far, the absorption spectra have been very similar from the UV to the IR spectral range. One error source might be the Fresnel reflection correction based on an incorrect Sellmeier equation. In the literature there are different publications reporting slightly different Sellmeier equations for MgO:LN, e.g. compare Zelmon [94] to Gayer [109]. The refractive index is very material specific, e.g. it depends strongly on Li/Nb and Mg/Nb ratios, and thus the Sellmeier equation from [94] used for the Fresnel correction might be slightly different from the actual Sellmeier equation for these particular MgO:LN crystals. One other reason for the slope might be the so-called multiphonon edge that is slightly different for CLN and MgO:LN, which drastically increases absorption for $\tilde{\nu} < 2000 \text{ cm}^{-1}$ [110], and which might already be measurable in the observed spectral range.

Origin of absorption bands All absorption bands observed between $5000 - 3390 \text{ cm}^{-1}$ ($2000 - 2950 \text{ nm}$) are probably caused by hydrogen impurities, because at least two of the peaks in each spectrum, for MgO:LN at $\tilde{\nu}_0 = 4455 \text{ cm}^{-1}$ and for CLN at $\tilde{\nu}_0 = 4429 \text{ cm}^{-1}$

and the OH-vibration peaks respectively, are caused by hydrogen, and all peaks in the observed spectral range decrease as the hydrogen content, i.e. OH-vibration peak, decreases. Transition-metal impurities can be excluded as origin for these various absorption bands because transition-metal impurities do not absorb photons in the range $5000 - 3390 \text{ cm}^{-1}$ ($2000 - 2950 \text{ nm}$) in LiNbO_3 [10]. As already mentioned, the observed absorption bands cannot be attributed to the already known combined OH-vibration-librations [62]. Further experiments have to be performed in order to study the origin of these absorption bands and if these bands might be explained by, e.g. defects in the vicinity of the hydrogen atoms, different hydrogen sites, combination bands similar to OH-vibration-librations [63], or coupled phonon-OH-vibrations.

Calibration The observation that the discovered absorption bands are caused by hydrogen is important for applications. In PPMgOLN crystals it is usually not possible to directly measure the absorption coefficient of small absorption bands such as those in the spectral range $4000 - 3570 \text{ cm}^{-1}$ ($2500 - 2800 \text{ nm}$). The PPMgOLN crystals usually are z-cuts and only 1 mm thick, which would not allow to measure *e*-wave absorption spectra by means of conventional absorption spectrophotometers due to the limited aperture. However, the OH peak for *o*-wave can be measured directly by conventional absorption spectrophotometers without much effort. Thus only a scaling factor between the OH-vibration peak and the absorption bands of interest has to be known, e.g. for *o*-wave light, the ratio of the maximum absorption coefficient of the OH-vibration peak to the maximum absorption coefficient of the absorption bands between $4000 - 3570 \text{ cm}^{-1}$ ($2500 - 2800 \text{ nm}$) is $\approx 300 \pm 50$ for both, CLN and MgOLN crystals. Applying this relation, the magnitude of these absorption bands can be easily inferred from the amplitude of the OH-vibration peak for *o*-wave light, and since the absorption bands between $4000 - 3571 \text{ cm}^{-1}$ ($2500 - 2800 \text{ nm}$) are similar in magnitude for both light polarizations, the magnitude of these absorption bands for *e*-wave light can also be estimated.

4.4 First OPO experiments – Operation of a 1550-nm-pumped singly-resonant continuous-wave OPO

In order to demonstrate the success of the annealing procedure and the importance for OPO applications, we build an SRO as described in Fig. 4.1 pumped with a tunable 1550-nm source based on an external cavity diode laser amplified in an EDFA. It delivers up to 20 W of CW single-frequency radiation around $\lambda = 1550$ nm. As the nonlinear medium we use either as-grown PPMgOLN or annealed congruent PPLN (PPCLN). In order to produce the annealed PPCLN crystal, first an as-grown 1-mm thick, 5-mm long z-cut CLN crystal is subject to annealing as is described for CLN in Sect. 4.1. After annealing the crystal is polished and subsequently poled with a $32.8\text{-}\mu\text{m}$ period by conventional electric-field poling methods [22]. The CLN crystals are used instead of MgO:LN crystals because of the easier poling properties, but poling of annealed PPMgOLN is also feasible.

The OPO is of conventional bow-tie type, designed for resonance at 2600 nm, with a spot size of $80\ \mu\text{m}$ at the center of the 1-mm thick, 5-cm long periodically poled crystal, which is anti-reflection coated at the signal and pump wavelengths. The output coupler has 99.9 % reflectivity at 2600 nm and 3 % reflectivity at the 3800-nm idler wavelength. It is important to note that the entire bowtie is contained in a vacuum chamber ($P = 5 \times 10^{-5}$ Torr) to eliminate absorption by water vapor in the cavity or adsorbed on the surface of the optics.

With the annealed PPCLN crystal CW SRO operation is achieved at a threshold pump power of only $P_{\text{thr}} = 6.5$ W. The pump wavelength can be tuned from $\lambda_p = 1545 - 1560$ nm resulting in a corresponding idler output wavelength of $\lambda_i = 3875 - 3850$ nm. At 12 W pump power the CW SRO achieves an idler output power of $P_{\text{idler}} = 3.2 \pm 0.2$ W over the entire pump wavelength tuning range. OPO operation is obtained with several annealed PPCLN crystals.

As noted in the introduction of Ch. 4, OPO operation using not-annealed PPMgOLN crystals cannot be obtained, which indicates that P_{thr} exceeds the available 20 W pump power due to losses of the signal wave in the signal tuning range 2500 – 2700 nm. This is exactly the range where we found the hydrogen impurities cause absorption bands in as-grown CLN and MgO:LN. The absorption coefficient of the as-grown PPMgOLN crystals for which CW SRO operation cannot be obtained is estimated to be about $\alpha_s = 0.008 \pm 0.001\ \text{cm}^{-1}$ around 2600 nm. This is deduced from the OH-vibration peak amplitude and the calibration factor of 300. Therefore P_{thr} is theoretically about 11-13 W larger than in an annealed PPCLN crystal. Together with the fact that there are additional cavity losses such as imperfect mirrors and coatings, and slightly changing adjustment, this explains why OPO operation with these PPMgOLN crystals is not feasible with 20 W of maximum available pump power.

4.5 Outlook and conclusion

Outlook Our results indicate that all observed absorption bands are caused by hydrogen impurities. High-temperature annealing decreases absorption significantly, however, it is not clear which electronic transitions generate these particular absorption peaks. Furthermore, the resolution of the various peaks in the spectra is not very good as well. Here further studies are necessary.

Absolute measurement methods such as photothermal-common-path interferometry [111] have to be developed further, especially in terms of wavelength tunability. Then it might also be possible, e.g. to determine if the observed slope in $\text{MgO}:\text{LN}$ is a measurement artifact and measurement precision might be significantly enhanced. In order to facilitate such studies as long as convenient measurement methods are not available, the same idea as in the case of the transition-metal impurities should be applied: Intentional doping with hydrogen. This will help to resolve the various absorption peaks. There already is one very efficient processes known to enrich CLN and $\text{MgO}:\text{LN}$ with hydrogen, so-called "proton exchange" (PE) in which Li atoms are exchanged with protons by chemical treatment of the crystal with special acids [56]. The Li-H exchange rate can be up to 85%. Unfortunately PE changes the crystal lattice structure due to Li-H exchange, e.g. the OH peak in CLN is shifted from about $\tilde{\nu}_0 = 2871 \text{ cm}^{-1}$ to $\tilde{\nu}_0 = 3510 \text{ cm}^{-1}$, hence PE is not an option. Softer methods have to be applied that do not strongly replace Li atoms with hydrogen, but which fill empty Li-sites with H atoms, so that the crystal structure is not significantly changed. One such method is conventional annealing in water vapor at about $700 \text{ }^\circ\text{C}$ [57] which can be even more efficient by simultaneously applying an electric field [112]. This can increase the hydrogen content by at least one order of magnitude. Using higher temperatures might help to facilitate in-diffusion of hydrogen even further.

In order to identify the various absorption peaks, temperature dependent absorption measurements are attractive. If low temperatures are applied, the linewidth of the peaks should narrow because lattice vibrations decrease. This will increase peak resolution significantly as was already shown for the OH-vibration peak [112]. On the other hand absorption measurements at elevated temperatures might reveal new optical transitions, as was demonstrated to be the case for the OH-vibration peak in $\text{MgO}:\text{LN}$ [113]. Hence temperature dependent absorption measurements might be a good starting point for the identification of the various absorption bands.

In contrast, for OPO applications it is of great interest to further decrease absorption in CLN and $\text{MgO}:\text{LN}$ by more than one order of magnitude. Hence the annealing process in dry oxygen has to be improved. One solution might be to use longer annealing times and higher annealing temperatures. Application of an electric field during annealing in dry atmosphere might also be a promising method in order to make the annealing more efficient.

Conclusion In this chapter we showed that there are so-far unknown absorption bands in CLN and MgO:LN that are on the order of $0.0005\text{-}0.01\text{ cm}^{-1}$ that are attributed to hydrogen impurities. High-temperature annealing decreased the hydrogen content by one order of magnitude, which was measured by the amplitude of the OH-vibration peak and it also suppressed absorption in the range $2200\text{--}2800\text{ nm}$ by up to one order of magnitude. Other impurities could be excluded as causes of these absorption bands. Finally annealed PPCLN crystals enabled successful operation of a 1550-nm pumped SRO that was very sensitive to optical absorption around 2600 nm .

Chapter 5

Pyroelectrically-induced photorefractive damage in $\text{LiNbO}_3\text{:MgO}$

5.1 Introduction

In the previous chapters we have studied the origin of the residual optical absorption in CLN and MgO:LN. We have identified small amounts of transition-metal impurities and, where it was possible, we have shown ways to reduce their amount and thus decrease residual absorption. In this chapter it will be shown which effects even the smallest amount of photo-excitabile electrons and absorption-induced heating can have on the optical performance of MgO:LN in nonlinear-optical applications.

As already discussed in Sect. 2.3.1.1, MgO:LN does not show PRD at even very high light intensities in the visible wavelength range. However, we observe in an OPO using a PPMgOLN crystal that was pumped with 1064-nm laser light characteristic PRD in the remaining uniformly poled parts of the crystal. The experiments indicate that the pyroelectric effect in combination with parasitic green light is related to this phenomenon. This leads us to the question if pyroelectrically-induced PRD can be observed in MgO:LN, even though it is known to show no conventional bulk-photovoltaic PRD, by choosing a suitable light intensity and creating a pyroelectric field [114–117]. Another open question is why damage is not observed in CLN under similar conditions.

In the following we first summarize what is known from literature about the impact of external and pyroelectric fields on photorefractive. Then we explore theoretically if pyroelectrically-induced PRD is possible in MgO:LN. Therefore the problem will be theo-

retically examined in one dimension. Then the model will be extended to two dimensions in order to simulate more realistic experimental conditions. The impact of this model on nonlinear-optical applications will also be discussed, as well as beam self heating and inhibition of pyroelectrically-induced PRD in $\text{MgO}:\text{LN}$. Finally experiments and their results will be presented and theoretical predictions will be compared to experimental results.

5.1.1 Photorefractive damage due to an externally applied electric field

The basic equation for the charge transport in a photorefractive medium is given by Eq. 2.23 which describes the total current density. Note that the electric field \mathbf{E} can be expressed by the electric potential ϕ through $\mathbf{E} = -\nabla\phi$. Now consider the case that a constant external potential difference is applied at the boundaries of an illuminated photorefractive crystal, e.g. a voltage is applied to the $+$ and $-z$ -faces, then ϕ splits up into an external and internal potential, i.e. $\phi = \phi_{\text{ext}} + \phi_{\text{int}}$. If the boundaries are far away from the beam and if the illuminated region is small compared to the dimensions of the crystal, the externally applied potential difference creates a constant electric field $\mathbf{E}_0 = -\nabla\phi_{\text{ext}}$. The total electric field in Eq. 2.23 can then be described as $\mathbf{E} = \mathbf{E}_0 - \nabla\phi_{\text{int}}$ and the boundary condition $\nabla\phi_{\text{int}} \rightarrow 0$ for $|\mathbf{r}| \gg w$, where w is the characteristic size of the beam such as the beam radius, has to be fulfilled. Then the basic current equation Eq. 2.23 becomes:

$$\mathbf{j} = \sigma(\mathbf{E}_0 - \nabla\phi_{\text{int}}) + k_b T \mu_e \nabla \tilde{n}_e + \beta I \hat{\mathbf{z}}. \quad (5.1)$$

It has also been shown experimentally that PRD is caused not only by the bulk-photovoltaic effect, but also by externally applied potential differences, i.e. external electric fields \mathbf{E}_0 , under simultaneous illumination, e.g. in LiNbO_3 doped with iron bulk-photovoltaic photorefractive is enhanced by application of an external electric field [118]. In another case a homogeneous electric field \mathbf{E}_0 is applied to a non-bulk-photovoltaic (or only weakly bulk-photovoltaic) but photoconductive medium such as SBN. There the refractive index is changed homogeneously according to Eq. 2.25, first, but as soon as the crystal is illuminated with, e.g. a Gaussian beam at a visible wavelength with \mathbf{E}_0 being present, the photoconductivity in the center of the beam becomes larger than in the outer wings of the beam or the dark parts of the crystal. Thus the increased photoconductivity together with \mathbf{E}_0 cause a drift current that leads to screening of \mathbf{E}_0 in the center of the beam [114, 119]. According to Eq. 2.25 this leads to a refractive index change within the beam profile and depending on the parameters of the beam this can either lead to beam distortion or even beam self-trapping. In the case of beam self-trapping a so-called "spatial bright screening soliton" is formed [120].

5.1.2 Pyroelectrically-induced photorefractive damage

The pyroelectric effect in LiNbO_3 can generate an electric field, the so-called "pyroelectric field" \mathbf{E}_{pyro} , that influences photorefraction similarly to an externally applied electric field \mathbf{E}_0 . The pyroelectric field in a z -cut plate, assuming homogeneous heating, is given by

$$\mathbf{E}_{\text{pyro}} = -\frac{1}{\epsilon_{33}\epsilon_0}p_3\Delta T\hat{\mathbf{z}}, \quad (5.2)$$

where ϵ_0 is the permittivity of vacuum, ϵ_{33} is the tensor element of the static permittivity tensor $\hat{\epsilon}$, and ΔT is the temperature change. Equation 5.2 means that a temperature change of 1 °C leads to $|\mathbf{E}_{\text{pyro}}| = 2.6$ kV/cm. If the dark conductivity σ_d is small enough, so that the decay of the electric field is slow, and if charge neutralization on the crystal surface is also weak, these fields may persist for several weeks [121]. Then, to a good approximation, \mathbf{E}_{pyro} can be treated as an external electric field \mathbf{E}_0 . That \mathbf{E}_{pyro} can substitute for \mathbf{E}_0 in photorefractive materials has already been shown [116, 117, 122, 123], e.g. it has been demonstrated that so-called "spatial screening-photovoltaic bright solitons" [124] are created in CLN by applying pyroelectric fields instead of an external electric field [122]. Furthermore, it has been shown that pyroelectric fields can cause beam distortion in materials such as barium strontium potassium sodium niobate (BSKNN), Ce-SBN:60, or SBN:60 that only show very weak or no bulk-photovoltaic effect [70, 114, 115]. For instance, a pyroelectric field is created by cooling a BSKNN, Ce-SBN:60, or SBN:60 crystal. Then the crystals are illuminated and the observed phenomena are the same as if an external electric field would be applied [114].

These results show that the pyroelectric effect can have an impact on photorefraction in various media in principle. For MgO:LN the influence of pyroelectric fields on the photorefractive behavior has not been studied yet, but it is of special interest, because MgO:LN does not suffer from bulk-photovoltaic PRD and therefore it is a commonly used nonlinear optical material for high-power frequency conversion devices. But, as discussed in previous chapters, use of high optical power also means that absorption of light and therefore heating occurs. And this heat accumulation in turn generates pyroelectric fields.

5.2 Theory

In this section we develop a theoretical model for pyroelectrically-induced whole-beam refractive-index changes in $\text{MgO}:\text{LN}$ in order to derive the electric potential ϕ and electric field \mathbf{E} .

5.2.1 Steady-state photorefractive effect – one-dimensional case

As already introduced in Sect. 2.3.1, the basic equation of photorefraction is given by Eq. 5.1. First we consider the one-dimensional (1D) steady-state case of Eq. 5.1 in accordance with [125] and using a similar notation. First, there are no external fields \mathbf{E}_0 applied and the temperature is constant in order to simplify the problem and introduce some new variables. One-dimensional means that a uniformly poled crystal is considered and a planar beam propagates through the crystal along $\hat{\mathbf{y}}$ with the gradient of intensity parallel to $\hat{\mathbf{z}}$.

In the following we assume that the crystal is illuminated with light of intensity $I(\mathbf{r}) = I_0 \bar{I}(\mathbf{r})$ with $\bar{I}(\mathbf{r}) \leq 1$. For a Gaussian intensity distribution in the planar case the normalized intensity is $\bar{I} = \exp(-2\xi^2)$, where w is the characteristic beam size, e.g. the beam radius, and $\xi = z/w$ is the spatial coordinate normalized to w . We make the assumption that local charge neutrality holds [125, 126] and that the intensity is low enough, so that the conductivity is linear in intensity (Eq. 2.24), i.e. $\sigma = \sigma_{\text{photo}} + \sigma_{\text{d}} = \kappa I + \sigma_{\text{d}}$. Note that the photoconductivity is mostly caused by electrons, thus it is also $\sigma_{\text{photo}} = \mu_e \tilde{n}_e e$, where e is the electron charge.

We introduce the concept of the so-called "equivalent dark intensity" I_{d} [119, 125], which is the intensity necessary to bring the photoconductivity up to a value of the dark conductivity. Then the conductivity can be written as

$$\sigma = \sigma_0 \bar{\sigma}(\mathbf{r}) = \sigma_0 [\bar{I}(\mathbf{r}) + \eta] , \quad (5.3)$$

where $\sigma_0 = \kappa I_0$ and $\eta = I_{\text{d}}/I_0$. This concept facilitates normalization of the problem. Furthermore, the ratio η of the equivalent dark intensity to the peak intensity will be an important parameter for the characterization of charge transport in LiNbO_3 in the following sections.

In steady state the current from Eq. 2.23 must obey $\nabla \cdot \mathbf{j} = 0$, thus the space-charge field generates a drift current $\mathbf{j}_{\text{drift}}$ balancing the other currents [125]. In the case of open-circuit boundary conditions the total electric field is then obtained

$$\mathbf{E}(\xi) = E_{\text{pv}} \frac{\bar{I}(\xi)}{\bar{I}(\xi) + \eta} \hat{\mathbf{z}} + E_{\text{w}} \frac{d\bar{I}(\xi)/d\xi}{\bar{I}(\xi) + \eta} \hat{\mathbf{z}} , \quad (5.4)$$

where the first term describes the bulk-photovoltaic field scaling with the characteristic bulk-photovoltaic field $E_{\text{pv}} = -\beta/\kappa$ and the second term describes the diffusion field E_{diff} with characteristic field $E_w = k_B T/(ew)$ [125].

5.2.2 Time-dependence of pyroelectrically-induced photorefractive damage – one-dimensional case

Assume that an unilluminated MgO:LN crystal of thickness H is uniformly heated by a temperature difference ΔT . This temperature difference generates a pyroelectric field \mathbf{E}_{pyro} according to Eq. 5.2. Regarding \mathbf{E}_{pyro} as equivalent to an externally applied electric field [123], one can assume that there is a fixed voltage U applied across the crystal thickness H if the experiment is done within a time t smaller than the dark decay time. With this assumption it is possible to separate the bound charges (the pyroelectric charge) from the free charges originating from the photo- and dark conductivities. If the crystal is then illuminated with an intensity pattern $I(\mathbf{r})$, and if we neglect the photovoltaic current and the diffusion, Eq. 2.23 simplifies to

$$\mathbf{j} = \sigma \mathbf{E} . \quad (5.5)$$

Note that, since we have formulated the transport as linear as discussed in Sect. 2.3.1, the pyroelectric field can be added to the bulk-photovoltaic and the diffusion field given in Eq. 5.4. However, for cases of interest here, the pyroelectric field will be much larger than the bulk-photovoltaic field. Furthermore, since we are only considering whole-beam effects the diffusion field is also orders of magnitude smaller than $|\mathbf{E}_{\text{pyro}}|$, e.g. for a $w = 100 \mu\text{m}$ and $T = 300 \text{ K}$ it is $E_w = 2.5 \text{ V/cm}$ while $|\mathbf{E}_{\text{pyro}}| = 2.6 \text{ kV/cm}$ for $\Delta T = 1 \text{ }^\circ\text{C}$. Thus diffusion will be neglected in the further analysis as well.

The relation between the current \mathbf{j} and the space charge density ρ is given by the continuity equation

$$\frac{\partial \rho}{\partial t} + \nabla \cdot \mathbf{j} = 0 . \quad (5.6)$$

Then Eq. 5.6 together with Gauss' law and Eq. 5.5 yield

$$\nabla \cdot \left[\epsilon \epsilon_0 \frac{\partial \mathbf{E}}{\partial t} + \sigma \mathbf{E} \right] = 0 \quad (5.7)$$

with the solution

$$\epsilon \epsilon_0 \frac{\partial \mathbf{E}}{\partial t} + \sigma \mathbf{E} = \mathbf{j}_d , \quad (5.8)$$

where \mathbf{j}_d is a divergenceless current chosen to meet the boundary conditions.

Assume fixed-voltage boundary conditions, i.e. that there is a fixed voltage applied across the crystal thickness H . Then a current is flowing even in the absence of illumination and

in the case that the illuminated region is small in extent compared to the thickness H of the crystal, i.e. $w \ll H$, j_d can be approximated by $j_d = U\sigma_d\hat{\mathbf{z}}/H$. This simple model is appropriate for our pyroelectric case for times short compared to the dark decay time of the pyroelectric field. Using the notation from Sect. 5.2.1 the solution for Eq. 5.8 is then given by

$$\mathbf{E}(\bar{t}, \xi) = \frac{U}{H} \left\{ \frac{\eta}{\bar{I}(\xi) + \eta} + \frac{\bar{I}(\xi)}{\bar{I}(\xi) + \eta} \exp[-\bar{t}(\bar{I} + \eta)] \right\} \hat{\mathbf{z}}, \quad (5.9)$$

where $\bar{t} = t/\tau_{\text{di}}$ and $\tau_{\text{di}} = \epsilon\epsilon_0/\sigma = \epsilon\epsilon_0/[\sigma_0(\bar{I} + \eta)]$ with $\sigma_0 = \kappa I_0$. The time constant τ_{di} is also known as the characteristic Maxwell time, the characteristic time for buildup or decay of electric fields in the illuminated medium.

For $\bar{t} = 0$ it follows $\mathbf{E} = (U/H)\hat{\mathbf{z}}$, which means that the field has not been screened in the illuminated region yet and is fully present. For the steady state case $\bar{t} \gg 1$ one gets $\mathbf{E}(\bar{t}, \xi) = U\eta\hat{\mathbf{z}}/[H(\bar{I}(\xi) + \eta)]$, which is a nearly flat-top profile for the commonly encountered case of $\eta \ll 1$. Due to Eq. 2.25 the change in the electric field in the illuminated area of the crystal (Eq. 5.9) leads to a refractive index change

$$\Delta n = -\frac{1}{2}n_e^3 r_{33} \frac{U}{H} \left\{ \frac{\eta}{\bar{I}(\xi) + \eta} + \frac{\bar{I}(\xi)}{\bar{I}(\xi) + \eta} \exp[-\bar{t}(\bar{I} + \eta)] \right\}. \quad (5.10)$$

This refractive index change consists of two parts

$$\Delta n = \Delta n_{\text{hom}} + \Delta n_{\text{ill}}. \quad (5.11)$$

First the homogeneous heating causes a homogeneous refractive index change

$$\Delta n_{\text{hom}} = -\frac{1}{2}n_e^3 r_{33} \frac{U}{H} \quad (5.12)$$

due to $\mathbf{E}_{\text{pyro}} = (U/H)\hat{\mathbf{z}}$. This homogenous refractive index change does not cause beam distortion. However, the subsequent illumination changes the refractive index inhomogeneously by

$$\Delta n_{\text{ill}} = -\frac{1}{2}n_e^3 r_{33} \frac{U}{H} \left(\frac{\bar{I}(\xi)}{\bar{I}(\xi) + \eta} \{ \exp[-\bar{t}(\bar{I} + \eta)] - 1 \} \right). \quad (5.13)$$

Note Δn_{ill} and Δn_{hom} have opposite signs. The refractive index change Δn_{ill} normalized to $-\Delta n_{\text{hom}}$ is shown in Fig. 5.1.

In Fig. 5.1a the normalized refractive index change is plotted for $\bar{t} = 5\tau_{\text{di}}$ and varying η . In Fig. 5.1b the normalized refractive index change is plotted for varying time t and $\eta = 0.001$. In both graphs \bar{I} is shown as a red dashed line. Note, for $\eta \rightarrow 1$ screening cannot be reached. This is the case when $\sigma_d = \sigma_0$.

The phenomenological explanation is the same as in Sect. 5.1.1; due to the increased photoconductivity in the center of the illuminated part of the crystal, E_{pyro} is screened

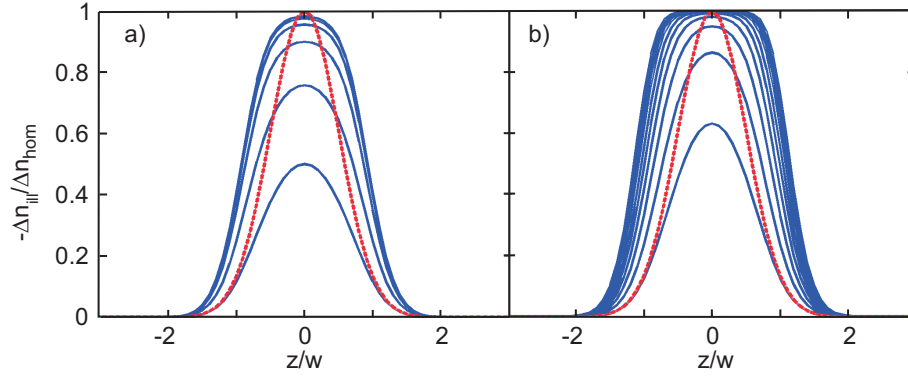


Figure 5.1: Pyroelectrically induced refractive index change Δn_{ill} (normalized to $-\Delta n_{\text{hom}}$) versus $\xi = z/w$. In a) the refractive index change is plotted for $\bar{t} = 5\tau_{\text{di}}$ and $\eta = 0.1^j$ varying logarithmically where $j = 0, 0.5, 1, 1.5, \dots, 4$ (from smallest to largest refractive index change) is just an index. The curves for $j = 2, \dots, 4$ overlap each other. In b) the refractive index change is plotted for $\bar{t} = 0, 1, \dots, 10 \times \tau_{\text{di}}$, and $\eta = 0.001$ (from inside to outside). In both graphs \bar{I} is shown as a red dashed line.

faster there than in the wings of the Gaussian light intensity distribution where the lower photoconductivity leads to slower screening of E_{pyro} . In the dark part of the crystal the entire pyroelectric field persists. This change in the electric field leads to a refractive index change according to Eq. 2.25, as can be seen in Fig. 5.1. Especially for times where the flat part of the refractive index profile has not yet developed, the transmitted beam will be distorted and partially deflected due to the refractive index change in the illuminated region. However, one can also expect that beam distortion will be reversed once the flat-top profile has developed because the beam would not be disturbed anymore.

5.2.3 Time-dependence of pyroelectrically-induced photorefractive damage – two-dimensional case

In order to solve the problem in the two-dimensional (2D) case, the corresponding general equations must be derived. The 2D-steady-state solution has already been derived by [119], the 2D time-dependent equations have been solved numerically for the model system bismuth titanate $\text{Bi}_{12}\text{TiO}_{20}$ with an external electric field applied, which neglects a bulk-photovoltaic current and diffusion [127]. Similar simulations can also be applied for the case of $\text{MgO}:\text{LN}$ as is shown in the following.

Again we assume that a $\text{MgO}:\text{LN}$ crystal is heated uniformly first, generating an electric field $\mathbf{E}_0 = \mathbf{E}_{\text{pyro}}$, and that \mathbf{E}_{pyro} is constant within the time frame of the experiment.

The diffusion term is neglected as in Sect. 5.2.2 since we only consider whole-beam effects. Simulations are performed for the case that \mathbf{E}_{pyro} has just been established and already is fully present, and illumination with a laser beam with Gaussian intensity distribution is then switched on. In the following we focus on the time dependence of the charge distribution ρ of free charge carriers which is determined by the continuity equation (Eq. 5.6). Substituting Eq. 5.1 into Eq. 5.6 one obtains

$$\frac{\partial \rho}{\partial t} = - \{ \kappa(\mathbf{E}_0 - \hat{\mathbf{z}}E_{\text{pv}}) \cdot \nabla I - \nabla \cdot [(\kappa I + \sigma_d)\nabla \phi_{\text{int}}] \} . \quad (5.14)$$

Furthermore, the Poisson equation gives the relation between ϕ_{int} and ρ :

$$-\frac{\rho}{\epsilon_0} = \epsilon_{11}\partial_x^2 \phi_{\text{int}} + \epsilon_{11}\partial_y^2 \phi_{\text{int}} + \epsilon_{33}\partial_z^2 \phi_{\text{int}} . \quad (5.15)$$

Unfortunately there is no analytical solution to this problem, however, it can be solved numerically with Finite-Difference-Time-Domain (FDTD) simulations that give a solution for ρ and ϕ . Then it is possible to determine the total electric field \mathbf{E} .

We perform FDTD simulations for the 2D case based on Eqs. 5.14 and 5.15. For the calculation a Gaussian light intensity distribution is assumed and $|E_{\text{pv}}| \ll |\mathbf{E}_{\text{pyro}}|$. Note that, for MgO:LN and the case of interest here, E_{pv} is orders of magnitude smaller than E_0 , thus it can be neglected. Concerning σ_d there hardly exist any data for CLN and MgO:LN for $T < 100$ °C because CLN and MgO:LN crystals are quite good electrical insulators for temperatures below 150 °C. In CLN one can assume that σ_d is in the range $10^{-16} - 10^{-18} (\Omega\text{cm})^{-1}$ [121]. For as-grown MgO:LN crystals doped with 5 mol% MgO an upper bound for σ_d at room temperature has been determined $\sigma_d \leq 2 \times 10^{-15} (\Omega\text{cm})^{-1}$ [128]. In another publication σ_d of MgO:LN doped with 5 mol% MgO is on the order of $10^{-16} (\Omega\text{cm})^{-1}$ [129] at room temperature. From [84, 129] it then becomes clear that σ_d in MgO:LN is at least two to three orders of magnitude smaller than $\sigma_0 = \kappa I_0$ in the intensity range $1 - 10 \text{ W/cm}^2$. Therefore we neglect σ_d in Eq. 5.14 and Eq. 5.16 for all cases where I_0 is on the order of 1 W/cm^2 or higher. This approximation will not affect the refractive index changes significantly in the region $|\mathbf{r}|/w < 2$ for MgO:LN. Furthermore, one can expect that σ_0 and σ_d are not affected by small temperature changes of less than 10 °C.

Figure 5.2 shows the time dependence of the refractive index change Δn_{ill} . Since $\hat{\epsilon}$ represents a tensor, a characteristic dielectric time constant has to be defined, which approximately describes an exponential time dependence of the z -component of the space charge field for $t \approx 0$ in the center of the illuminated region and which depends on κ as well. For LiNbO_3 and the z -component of the electric field this time constant is given by [130]:

$$\tau_{\text{di}} = \frac{\epsilon_0(\epsilon_{33} + \sqrt{\epsilon_{33}\epsilon_{11}})}{\kappa I_0 + \sigma_d} . \quad (5.16)$$

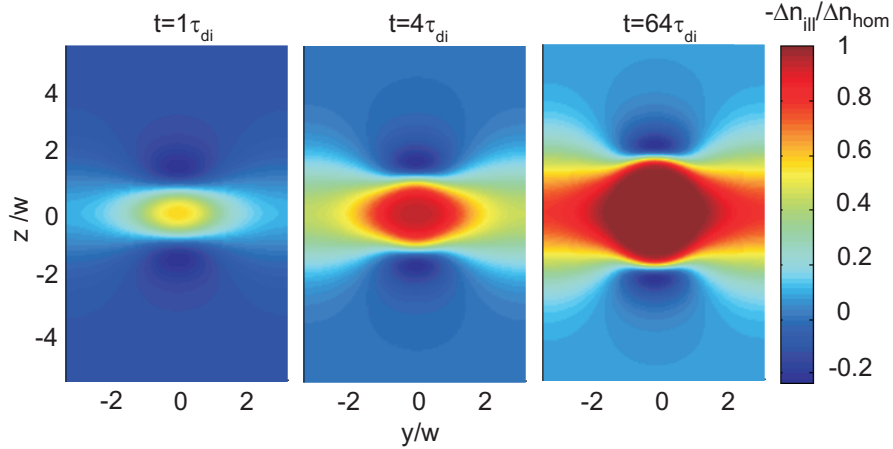


Figure 5.2: Numerically simulated normalized refractive index change $-\Delta n_{\text{ill}}/\Delta n_{\text{hom}}$ for the 2D case. The illuminated area is small in extent compared to the z and y dimensions of the crystal. The ratio of $\epsilon_{11}/\epsilon_{33}$ is 2.9, as is the case for $\text{MgO}:\text{LN}$.

Hence time t in Fig. 5.2 is normalized to τ_{di} . The refractive index change Δn_{ill} is normalized to Δn_{hom} . The 2D-simulations show the screening of the pyroelectric field in the areas of increased σ_{photo} . With increasing time, similar to the 1D-case, a flat-top refractive-index profile develops in the illuminated area. In the dark areas of the crystal the entire pyroelectric field is present and the refractive index is unchanged. However, the 2D-case is also slightly different from the 1D-case. Similar to conventional PRD in CLN, the characteristic side lobes in $+z$ and $-z$ direction develop with opposite sign with respect to that of the flat area in the middle [119]. Figure 5.3 depicts z -cuts through the refractive index profile beam center $\Delta n_{\text{ill}}(y=0, z)$ normalized to $-\Delta n_{\text{hom}}$ for different illumination times t in multiples of τ_{di} . Again similarities to the 1D case are obvious.

5.2.4 Impact on applications

One simple solution to inhibit pyroelectrically-induced PRD due to homogeneous heating simply is to short-circuit the c -faces of the crystal, e.g. by applying a conductive paste on the c -faces and electrically connecting them with each other. This connection prevents the crystal from accumulating surface charges during heating or cooling, hence pyroelectric fields cannot develop. However, if a nonlinear-optical device with a PPMgOLN crystal is pumped by a strong infrared pump beam, spatially inhomogeneous self-heating occurs, and thus local temperature increase can induce local pyroelectric fields that cannot be fully screened by short-circuiting the surfaces of the crystal. It has been reported from experimental observations in SBN that a pyroelectric field due to beam self-heating with

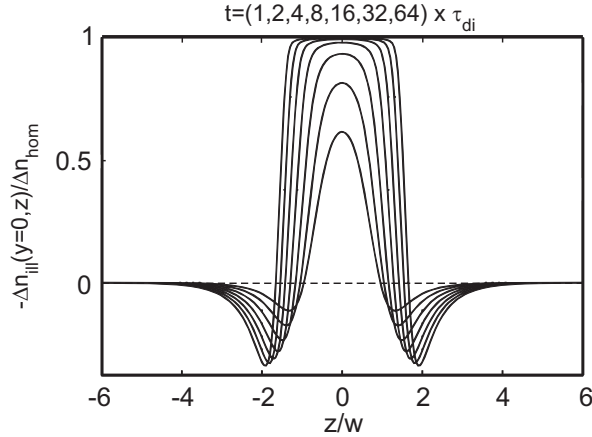


Figure 5.3: Numerically simulated refractive index change $\Delta n_{\text{ill}}(y=0, z)$ in MgO:LN for varying illumination times $t = 1\tau_{\text{di}}, 2\tau_{\text{di}}, 4\tau_{\text{di}}, 8\tau_{\text{di}}, 16\tau_{\text{di}}, 32\tau_{\text{di}}, 64\tau_{\text{di}}$ (smallest to largest Δn_{ill}).

visible laser light can be created in pyroelectric media [131]. There the pyroelectric fields lead to lensing. The same can be expected to happen in MgO:LN if just a strong enough infrared pump beam is used because there is always residual optical absorption inside the crystal. Since, at the same time, high average power infrared lasers usually generate some parasitic visible light in PPMgOLN due to accidentally phase-matched frequency conversion processes [132], this parasitic light would then partially screen the pyroelectric fields, and hence a very inhomogeneous pyroelectrically induced refractive index profile would be the consequence.

In the following sections a new theoretical model for the pyroelectrically-induced PRD in MgO:LN due to beam self-heating will be developed and a method to reduce this effect will be presented.

5.2.4.1 Beam self-heating in a uniformly poled $\text{LiNbO}_3:\text{MgO}$ crystal

In the case of a uniformly poled MgO:LN crystal in which a laser beam is partially absorbed, there will be a radially varying temperature rise in addition to an increase in the average temperature of the crystal. The pyroelectric effects associated with the average temperature rise can be eliminated by short-circuiting the z -faces of the crystal, as discussed in Sect. 5.2.4. However, the spatially varying part of the temperature will create a volume polarization charge, which cannot be screened by the surface, but will be screened by the

volume conductivity of the crystal. Thus in the case of beam self-heating we also have to include the heat equation into our model. As already mentioned, pyroelectrically induced lensing was reported experimentally in SBN [131]; here we analytically and numerically investigate this effect and its implications for $\text{MgO}:\text{LN}$.

In the case of self heating it is possible to get analytic solutions for the space charge fields involved in the pyroelectrically-induced PRD only for times short compared to the dielectric relaxation time. We will derive some approximations for the temperature and pyroelectric field before we solve the problem with numerical FDTD simulations.

First we determine the temperature field. The heat equation is given by

$$\left(\frac{1}{k_{\text{th}}} \frac{\partial}{\partial t} - \nabla^2 \right) \Delta T = \frac{q(\mathbf{r})}{\lambda_{\text{th}}}, \quad (5.17)$$

where ΔT is the temperature rise above the original temperature, q is the heat generated per unit volume per unit time by absorption of the optical beam, k_{th} is the thermal diffusivity, and λ_{th} is the thermal conductivity. Furthermore, it is $k_{\text{th}} = \lambda_{\text{th}}/\rho c_p$, where ρ is the mass density and c_p is the heat capacity. Note, k_{th} and λ_{th} are second-rank tensors. The anisotropy of these properties can again be neglected for LiNbO_3 [8]; in other media they may have to be taken into account. For an intensity distribution $I(\mathbf{r})$ and absorption coefficient α the heat source term q is given by

$$q(\mathbf{r}) = \alpha I(\mathbf{r}) = \alpha I_0 \bar{I}(\mathbf{r}), \quad (5.18)$$

where we normalize the intensity to its peak value, I_0 .

The thermal field in steady state obeys [133]

$$\nabla^2(\Delta T) = -q(\mathbf{r})/\lambda_{\text{th}}. \quad (5.19)$$

It is convenient to normalize the temperature according to $\Delta T(\mathbf{r}) = T_0 \Delta \bar{T}(\bar{\mathbf{r}})$, where $T_0 = \alpha I_0 w^2/\lambda_{\text{th}}$ is the temperature field amplitude and $\bar{\mathbf{r}} = \mathbf{r}/w$ (in the one-dimensional case it is $\xi = z/w$). In terms of optical power $P = \pi I_0 w^2/2$ for a Gaussian beam it is

$$T_0 = 2P\alpha/(\pi\lambda_{\text{th}}). \quad (5.20)$$

With these definitions Eq. 5.19 can be written

$$\bar{\nabla}^2(\Delta \bar{T})(\bar{\mathbf{r}}) = -\bar{I}(\bar{\mathbf{r}}). \quad (5.21)$$

The solution $\Delta T(r)$ of Eq. 5.19 for a Gaussian beam $I(r) = I_0 \exp[-2(r/w)^2]$ at radius r from the heat source in a cylindrical sample with radius R is given in terms of exponential integral functions [133]

$$\Delta T(r) = \frac{\alpha P}{4\pi\lambda_{\text{th}}} \left[-E_i \left(-2\frac{R^2}{w^2} \right) + E_i \left(-\frac{2r^2}{w^2} \right) - 2 \ln \left(\frac{r}{R} \right) \right]. \quad (5.22)$$

The boundary condition at $r = R$ is taken to be $\Delta T(r = R) = 0$. The on-axis asymptotic form ($\mathbf{r} \rightarrow 0$) of Eq. 5.22 is

$$\Delta T(0) \approx \frac{\alpha P}{4\pi\lambda_{\text{th}}} \left[\gamma_{\text{Euler}} + \ln \left(2 \frac{R^2}{w^2} \right) \right], \quad (5.23)$$

where $\gamma_{\text{Euler}} \sim 0.577215\dots$ is Euler's constant. In a next step the maximum pyroelectric field that can build up due to beam self heating is estimated. The appropriate analysis of this situation depends on the time constants for the thermal field to become established versus τ_{di} . The time for the portion of the thermal field varying across the beam region to become established is on the order of the thermal diffusion time $\tau_{\text{th}} = w^2/(4k_{\text{th}})$. For $w = 50 \mu\text{m}$, $\lambda_{\text{th}} \approx 5 \text{ W}/(\text{m K})$, $\rho \approx 4.64 \text{ g}/\text{cm}^3$, and $c_p \approx 0.5 \text{ J}/(\text{g K})$ [8], as would be appropriate for a confocally focused beam of $1\text{-}\mu\text{m}$ radiation in a 20-mm-long LiNbO_3 crystal, the thermal diffusion time is $\tau_{\text{th}} \approx 0.001 \text{ s}$. In contrast, τ_{di} can be months in CLN in the dark or several weeks in $\text{MgO}:\text{LN}$. Under illumination with green light of intensity $100 \text{ W}/\text{cm}^2$ the time constant τ_{di} in CLN can be several minutes [134] and on the order of seconds in $\text{MgO}:\text{LN}$ [84]. Hence we assume that the steady-state thermal field is established before the polarization charge is significantly screened. It should be borne in mind that for sufficiently large samples non-negligible screening can occur before the thermal field has diffused to the edges of the crystal.

From [130] it can be derived that the z-component of the pyroelectric field in the beam center, before charge screening starts, takes the form

$$E_{z,\text{pyro}} \approx -\frac{p_3 T_0}{\epsilon_0(\epsilon_{33} + \sqrt{\epsilon_{33}\epsilon_{11}})} \text{ for } t \ll \tau_{\text{di}}, \quad (5.24)$$

where the anisotropy factor $\epsilon_{33} + \sqrt{\epsilon_{33}\epsilon_{11}}$ for the z-component of the pyroelectric field in the beam center is used according to [130]. Thus a characteristic pyroelectric field is defined for the beam self-heating case by substituting Eq. 5.23 into Eq. 5.24:

$$E_{\text{pyro}} \approx -\frac{p_3 \alpha P \left[\gamma_{\text{Euler}} + \ln \left(\frac{2R^2}{w^2} \right) \right]}{4\pi\lambda_{\text{th}}\epsilon_0 (\epsilon_{33} + \sqrt{\epsilon_{33}\epsilon_{11}})}. \quad (5.25)$$

For 2D temperature diffusion in the slab-like crystal geometry used in practice, the temperature rise of the beam center also depends logarithmically on the size of the crystal. We find that for an estimate for the temperature rise of the beam center in this case $\ln(2R^2/w^2)$ can be replaced with $\ln \left[(\min[L_y, L_z]/w)^2 / 2 \right]$, where L_y and L_z are the dimensions of the crystal in y or z direction respectively. Note, the scaling of E_{pyro} in the beam self-heating case is qualitatively different between the 1D and 2D geometries. This difference arises because the temperature rise at the beam center is much smaller when thermal diffusion occurs in two dimensions rather than one.

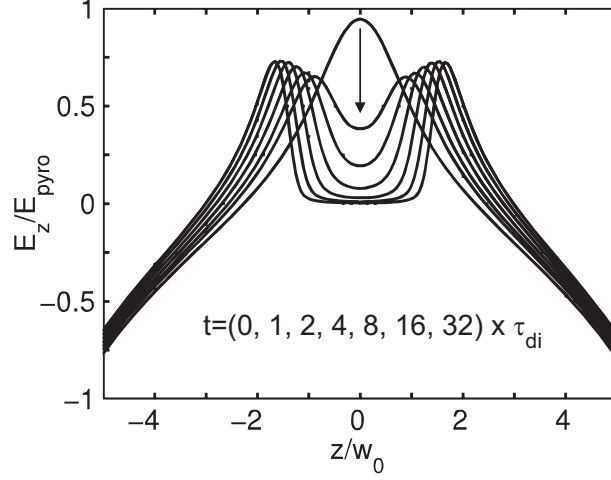


Figure 5.4: Cut of $E_z(y = 0, z, t)$ through the 2D electric field profile along the z -axis for the beam self-heated case for different times (multiples of τ_{di}) and slab-like crystal shape normalized to E_{pyro} . For $t = 0$ the curve is parabolic around $y = z = 0$, for longer times a flat-top profile starts to develop. The electric field is normalized to E_{pyro} from Eq. 5.25.

In order to determine the electric field for all \mathbf{r} and times t in the case of beam self-heating, two-dimensional FDTD simulation were performed by taking Eq. 5.19 into account in addition to Eqs. 5.14 and 5.15. Again it was assumed that $\sigma_{\text{photo}} = \kappa I$. The potential ϕ and the charge distribution ρ were determined for a slab-shaped crystal taking into account that the total time-dependent charge density is a sum of pyroelectric and free electronic charge densities ($\rho = \rho_{\text{pyro}} + \rho_{\text{free}}$) with

$$\rho_{\text{pyro}}(\mathbf{r})(\mathbf{r}, t = 0) = -\nabla \cdot (\Delta \mathbf{P}_s) = -\nabla \cdot (p_3 \Delta T(\mathbf{r}) \hat{\mathbf{z}}), \quad (5.26)$$

where \mathbf{P}_s is the spontaneous polarization. Again we used $\sigma \approx \kappa I$ and $t_{\text{th}} = w^2/(4k_{\text{th}}) = 0.001$ s. As boundary conditions $\phi = 0$ and $\Delta T = 0$ have to be fulfilled at the crystal surfaces at all times, i.e. we assume that the crystal surface is perfectly heat sunk to a fixed temperature and electrically grounded.

As a result the cut $E_z(y = 0, z, t)$ through the electric field profile along the z -axis is shown in Fig. 5.4 for different times (multiples of τ_{di}). For $t = 0$ the curve is parabolic around $y = z = 0$, while for longer times a flat-top profile starts to develop. For convenience the plot is normalized to E_{pyro} (Eq. 5.25) considered above. Thus, for short times, the pyroelectric field causes an imperfect lensing effect, but for intermediate times a rather hard edge in the pyroelectric field (and therefore in the refractive index profile) develops in the region of significant intensity, which can cause PRD. Whole-beam diffractive and holographic effects can be calculated in 3D by adding the x -axis as the light-propagation

direction into the simulations and including beam diffraction to calculate the resulting electric field $\mathbf{E}_{\text{optical}}(x, y, z, t)$, which will be described elsewhere.

As a practical example, according to Eq. 5.20 a LiNbO_3 crystal with an absorption coefficient $\alpha = 0.005 \text{ cm}^{-1}$ illuminated with a Gaussian beam of power $P = 20 \text{ W}$ would change the steady-state temperature difference across the beam by about 1.2 K and create a pyroelectrically-induced refractive-index change before screening (extraordinarily polarized) on the order of -2×10^{-5} . In comparison, a temperature change of 1.2 K would create a thermo-optic refractive index change of about 4×10^{-5} (Eq. 2.27). Considering Eq. 2.28, a beam with typical beam radius of, e.g. $w = 100 \text{ }\mu\text{m}$ and a crystal length of $L = 20 \text{ mm}$ would create a thermo-optic focusing lens with a focal length of about 20 mm [91]. The pyroelectrically induced refractive index change before charge screening starts creates a defocusing lens with focal length on the same order of magnitude as the thermo-optic lens. But due to charge screening the pyroelectrically-induced refractive index change will become spatially even more inhomogeneous for times exceeding the dielectric relaxation time. (Fig. 5.4). Hence thermo-optic and pyroelectric refractive index changes will not cancel out each other, but will lead to a very inhomogeneous refractive index profile which will cause beam distortion and light scattering. This combined lensing effect illustrates the importance of pyroelectrically induced refractive index changes.

5.2.4.2 Electric field due to beam self-heating in a periodically-poled LiNbO_3 crystal

Although homogenous pyroelectric fields can be short-circuited in principle, in the case of beam self-heating, short-circuiting the z -facets will not completely solve the problem (Fig. 5.4). One solution might be homogeneous illumination of the crystal with UV light [135]. However there might be an even easier solution to the problem: Periodic poling. It was already theoretically shown that the bulk-photovoltaic PRD is strongly suppressed in periodically poled CLN [125, 136]. In the following we will show that a similar analysis as shown in [125] can be applied to the pyroelectrically-induced PRD.

Consider the same basic assumptions as in case of beam self-heating in a uniformly poled crystal, but include a domain pattern varying periodically along y with a fundamental spatial frequency $K_g = 2\pi/\Lambda$ (Λ is the poling period), so that, noting that the pyroelectric coefficient varies from positive to negative sign in oppositely oriented domains, it can be written as

$$p(y)/p_3 = a_0 + \sum_{m=1}^{\infty} a_m \cos(mK_g y + \nu_m) , \quad (5.27)$$

where $a_0 = 2D - 1$, and $a_m = 4 \sin(\pi m D) / (\pi m)$, with D being the QPM duty cycle, and p_3 is again the bulk pyroelectric coefficient. The DC term a_0 is proportional to the deviation

in the duty cycle from its ideal value (for odd order QPM) of 50 %. For $D = 50\%$ and for a grating whose first domain is centered at $y = 0$ it is $a_0 = 0$, $a_m = 4/(m\pi)$ for $m = 1, 5, 9, \dots$ and $a_m = -4/(m\pi)$ for $m = 3, 7, 11, \dots$, and $a_m = 0$ for m even and the $\nu_m = 0$.

According to Eq. 5.26 and a vector identity, it can be shown that the pyroelectric charge density ρ_{pyro} is $\rho_{\text{pyro}}(\mathbf{r}, t = 0) = -\hat{\mathbf{z}} \cdot \nabla [p(y)\Delta T(\mathbf{r})]$. For short times $t \ll \tau_{\text{di}}$, the pyroelectric field obeys $\nabla \cdot \mathbf{E} = \rho_{\text{pyro}}/\epsilon\epsilon_0$. The problem is most conveniently solved in terms of the potential rather than directly for E_{pyro} [125]:

$$\nabla^2 \phi = \frac{\hat{\mathbf{z}} \cdot \nabla [p(y)\Delta T(\mathbf{r})]}{\epsilon\epsilon_0}, \quad (5.28)$$

where the potential can be taken in the form

$$\phi(\mathbf{r}) = \Phi_0(x, z) + \sum_{m=1}^{\infty} \Phi_m(x, z) \cos(mK_g y + \nu_m). \quad (5.29)$$

Since we only consider the case where $\hat{\mathbf{c}} \parallel \hat{\mathbf{z}}$, it follows

$$\nabla^2 \phi = \frac{p(y)}{\epsilon\epsilon_0} \hat{\mathbf{z}} \cdot \nabla [\Delta T(\mathbf{r})]. \quad (5.30)$$

For simplicity we discuss the planar case where $I = I(z) = I_0 \bar{I}(z)$, $\xi = z/w$, and $\Delta T(z) = T_0 \Delta \bar{T}(\xi)$. With Eqs. 5.27, 5.29, and 5.30 and projecting out the various coefficients, the m 'th term in Eq. 5.28 obeys

$$(\nabla_t^2 - m^2 K_m^2) \Phi_m(x, z) = \frac{p_3 a_m}{\epsilon\epsilon_0} \hat{\mathbf{z}} \cdot \nabla_t [\Delta T(\mathbf{r})], \quad (5.31)$$

where $m = 0, 1, 2, \dots, \infty$ includes the DC term as well as those with spatial modulation, and $\nabla_t = \nabla - \mathbf{y}\partial/\partial y$. Equation 5.31 then becomes

$$\left(\frac{d^2}{d\xi^2} - m^2 K_g^2 w^2 \right) \Phi_m(\xi) = \frac{p_3 T_0 a_m}{\epsilon\epsilon_0} w \frac{d\Delta \bar{T}(\xi)}{d\xi}. \quad (5.32)$$

In the case of uniform poling, i.e. $m = 0$, and with $\mathbf{E} = -\hat{\mathbf{z}}d\phi/dz$, one obtains $E(z) = -p_3 a_0 \Delta T(z) \hat{\mathbf{z}} / (\epsilon\epsilon_0)$ which is consistent with E_{pyro} in Eq. 5.2. As mentioned in [125], $K_g^2 w^2$ is usually quite large, e.g. for $\Lambda = 30 \mu\text{m}$ and $w = 50 \mu\text{m}$ which are typical numbers for a PPMgOLN crystal used for OPOs, $K_g^2 w^2 = 110$. Thus, in the case $m^2 K_g^2 w^2 \gg 1$, Eq. 5.32 becomes simply

$$\Phi_m(\xi) = -\frac{p_3 T_0 a_m}{\epsilon\epsilon_0} \frac{1}{m^2 K_g^2 w^2} \frac{d\Delta \bar{T}(\xi)}{d\xi}. \quad (5.33)$$

With Eq. 5.21, $T_0 = \alpha I_0 w^2 / \lambda_{\text{th}}$, and in analogy to Eq. 5.29 $E_z(y, z) = E_{z,0}(z) + \sum_{m=1}^{\infty} E_{z,m}(z) \cos(mK_g y + \nu_m)$ the transverse component of the electric field is

$$E_{z,m}(z) = -\frac{1}{w} \frac{\partial \Phi_m(y, \xi)}{\partial \xi} = -\frac{p_3 \alpha I_0 w^2 a_m}{\epsilon \epsilon_0 \lambda_{\text{th}}} \frac{1}{m^2 K_g^2 w^2} \bar{I}(\xi). \quad (5.34)$$

There also is a longitudinal field $E_y(y, z)$ that can be derived similarly, but in analogy to the photovoltaic case discussed in [125] it is not important for this analysis, because it is $\pi/2$ out of phase with the domain grating and hence does not significantly contribute to the average electro-optic refractive index change.

In order to determine the electro-optic refractive index change according to Eq. 2.25, the same analysis as in [125] is done by expanding the electro-optic tensor r/r_{33}^{eff} in a Fourier series like $p(y)/p_3$ in Eq. 5.27. Then the refractive index change is

$$\Delta n_{e,\text{PPMgOLN}} = -\frac{p_3 T_0}{\epsilon \epsilon_0} \frac{n_e^3 r_{33}^{\text{eff}}}{2} \left[a_0 + \sum_{m=1}^{m=\infty} \frac{a_m}{2} \cos(mK_g y + \nu_m) \right] \times \left[E_{z,0} + \sum_{m=1}^{m=\infty} E_{z,m} \cos(mK_g y + \nu_m) \right]. \quad (5.35)$$

Due to the fact that for $D \sim 50\%$, $a_1 \gg a_0$ and $a_m \propto 1/m$ in Eq. 5.35, terms for $m > 1$ and mixed terms can be neglected in the Fourier series. Thus a good approximation is

$$\Delta n_{e,\text{PPMgOLN}} \approx -\frac{p_3 T_0}{\epsilon \epsilon_0} \frac{n_e^3 r_{33}^{\text{eff}}}{2} \left[a_0^2 \Delta \bar{T}(\xi) + \frac{a_1^2}{2 K_g^2 w^2} \cos^2(K_g y) \bar{I}(\xi) \right]. \quad (5.36)$$

The refractive index change in a uniformly poled crystal due to beam self-heating is (Eq. 5.24) $\Delta n_{e,u} = -p_3 T_0 n_e^3 r_{33}^{\text{eff}} / (2\epsilon \epsilon_0)$, thus in a PPMgOLN crystal with 50 % duty cycle it is

$$\frac{\Delta n_{e,\text{PPMgOLN}}}{\Delta n_{e,u}} \approx \frac{8}{\pi^2} \frac{1}{(K_g w)^2} \frac{\bar{I}(\xi)}{\Delta \bar{T}(\xi)}. \quad (5.37)$$

Equation 5.37 shows that the electro-optic index change in PPMgOLN is suppressed by a factor $(\pi K_g w)^2 / 8$ compared to that in uniformly poled MgO:LN, which can be about about 1/140 if one assumes the same experimental parameters mentioned above are used. It also shows that the refractive index perturbation is proportional to the intensity profile $\bar{I}(\xi)$ in PPMgOLN, whereas it is proportional to the temperature change profile $\Delta \bar{T}(\xi)$ in the case of uniform poling. Note, for PPMgOLN in the 2D case $\Delta n_{e,\text{PPMgOLN}} \propto d^2(\Delta T) / d\xi^2$.

The previous analysis was made under the assumption of a perfect 50 % QPM duty cycle. However, if there is a duty cycle error of $a_0 = 2D - 1$, suppression is less effective and the

DC term ($m = 0$) in Eq. 5.36 adds a significant contribution when

$$a_0^2 = (2D - 1)^2 > \frac{8}{\pi^2} \frac{1}{(K_g w)^2} , \quad (5.38)$$

e.g. for $\Lambda = 30 \mu\text{m}$ and $w = 50 \mu\text{m}$ and $D \approx 54 \%$ the maximum refractive index suppression is $\Delta n_{e,\text{PPMgOLN}}/\Delta n_{e,u} \approx 1/70$ which is already only half of that for $D = 50 \%$. With a deviation from a perfect duty cycle pyroelectric fields can build up due to beam self-heating and therefore can lead to pyroelectrically-induced PRD. The above analysis shows that even if there is only a small portion of the light path where there are duty cycle errors or where periodic poling is totally missing, e.g. at the crystal edges, PRD can occur, especially in resonators. If that is the case it is very likely that using a strong infrared pump beam that generates parasitic green or blue light, whose photo-generated carriers partially screen the pyroelectric fields, can cause pyroelectrically-induced PRD in the PPMgO:LN sample in addition to conventional thermo-optic lensing effects.

The theoretical analyses in Sect. 5.2.2, 5.2.3, and 5.2.4 are not limited to MgO:LN in principle but could apply to other periodically-poled photoconductive ferroelectrics as well.

5.3 Experimental setups and results

In the previous sections we have developed a theoretical model for pyroelectrically induced whole-beam photorefractive effects in MgO:LN. In the following sections we present experimental data.

The experiments are conducted with several 5-mol% MgO-doped LiNbO_3 (MgO:LN) and undoped CLN crystals provided by Crystal Technology, Inc. (CTI). For comparison, and in order to make sure that the results are not crystal-grower specific, MgO:LN crystals from Yamaju Ceramics Co., Ltd. are also used. All crystals are polished to high optical quality on their x -facets of the crystals. Table 5.1 summarizes all samples used in the experiments.

Vendor	Crystal type	Dimensions $x \times y \times z$ (mm ³)	Short name
Crystal Technology	CLN	$20 \times 20 \times 20$	CLN ₁
	CLN	$9 \times 11 \times 1$	CLN ₂
	MgO:LN	$9 \times 11 \times 1$	CTIMgOLN ₁
	MgO:LN	$9 \times 11 \times 0.5$	CTIMgOLN ₂
	MgO:LN	$25 \times 25 \times 25$	CTIMgOLN ₃
	MgO:LN	$25 \times 15 \times 20$	CTIMgOLN ₄
Yamaju Ceramics	MgO:LN	$10 \times 12 \times 0.5$	YamMgOLN ₁

Table 5.1: *Crystals used in the photorefraction experiments and their short names.*

5.3.1 Beam distortion

5.3.1.1 Setup and experimental procedure

Prior to each measurement, the crystal under investigation is thoroughly cleaned with acetone, water, and methanol. Then the crystal is placed on a heated aluminum block, which itself is mounted on a 3-axis translation stage. Before the start of any experiment the crystal is thermally equilibrated to the initial oven temperature T_1 , and electric charges that may have been generated pyroelectrically or deposited on the crystal surfaces during handling are removed by short-circuiting the z -faces of the crystals temporarily. Then the crystal is put in open-circuit condition again.

The crystal is illuminated with a Gaussian beam of 532-nm radiation from a frequency-doubled continuous-wave Nd:YAG laser, linearly polarized along the crystallographic z -axis

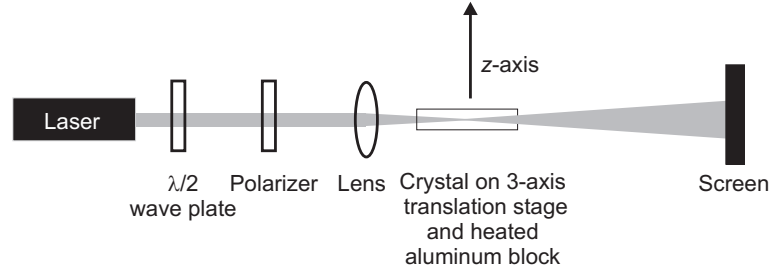


Figure 5.5: Setup for the observation of beam distortion. The laser is a 532-nm frequency-doubled continuous-wave Nd:YAG laser.

and propagating along the x -direction of the crystal. The temperature of the crystal is controlled with a temperature accuracy of ± 0.1 °C at the surface of the crystal in contact with the heating block; the temperature is also measured at the opposite (air) surface of the crystal. During illumination the crystal is heated until the top and bottom of the crystal reaches stable T_f . Experiments are also carried out with the illumination applied after the crystal has been thermally equilibrated at the final temperature T_f .

The setup is shown schematically in Fig. 5.5. Before the beam enters the crystal, it passes through a half-wave plate and a polarizer which, together with neutral density filters, enables continuous adjustment of the power P incident on the crystal from $20 \mu\text{W}$ to 2 W . The beam is focused at the center of the crystal to a $1/e^2$ intensity diameter $2w$, which is $100 \mu\text{m}$ in all experiments unless otherwise noted. The incident beam is extraordinarily polarized, i.e. polarized along the z -axis of the crystal. The transmitted beam is observed on a screen placed approximately 50 cm beyond the output face of the crystal. Various temperature differences $T_f - T_i$ are applied in several experiments, however, T_f is always kept below 50 °C. After illumination is stopped, the c -faces of the crystal are short-circuited to discharge any pyroelectric surface charges while the crystal cools down to the initial temperature T_i . Note that any internal space charge fields that may have been created during illumination would not be erased by this process [114].

5.3.1.2 Results

Before studying the effects of changing the temperature of the MgO:LN crystals, we first carry out measurements on samples CTIMgOLN₁, CTIMgOLN₂, and YamMgOLN₁ at constant temperature in order to examine their conventional photovoltaic PRD behavior. For these measurements, the crystals are illuminated along the x -axis, first with $P = 2 \text{ W}$ and then with $P = 20 \mu\text{W}$. No measurable PRD is observed in any of the MgO:LN crystals (less than 1 % change in diameter on the screen in the far field).

The $\text{MgO}:\text{LN}$ samples are then illuminated at a constant power of $20 \mu\text{W}$, and the temperature is ramped from $T_i = 40 \text{ }^\circ\text{C}$ to $T_f = 50 \text{ }^\circ\text{C}$ in order to investigate the effects of varying temperature. A picture of the shape of the beam transmitted through sample YamMgOLN_1 at different stages of the experiment is shown in Fig. 5.6.

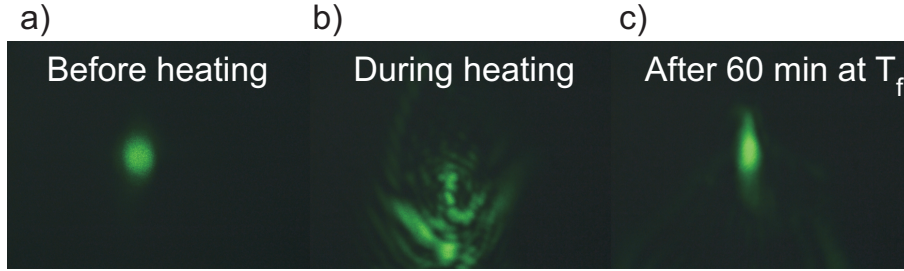


Figure 5.6: Shape of a laser beam after passing a $\text{MgO}:\text{LiNbO}_3$ crystal (sample YamMgOLN_1) that is heated from $40 \text{ }^\circ\text{C}$ to $50 \text{ }^\circ\text{C}$.

All $\text{MgO}:\text{LN}$ samples show similar behavior. Less than one second after initiation of the temperature ramp, PRD is observed with typical beam distortion and far-field pattern formation. After several seconds the original beam shape cannot be recognized anymore (Fig. 5.6b); however, the beam shape continues to evolve. Beam distortion remains even after the crystal equilibrates to T_f . Finally, after several minutes in this stage, the beam shape begins to restore slowly towards its original shape, but it does not fully recover. Scattered light is still observed in the region outside the original beam diameter even after one hour elapses (Fig. 5.6c).

In another experiment the samples are heated first and then, after thermal equilibration at T_f , are subject to subsequent illumination with the same beam parameters as described above in order to create optical damage. Illumination is started once the selected temperature has been reached. Note between heating and illumination the crystal c-facets are not short-circuited again. In all the samples the beam shows similar distortion as seen in Fig. 5.6b.

In order to investigate the persistence of these photorefractive effects, the $\text{MgO}:\text{LN}$ crystals with PRD are stored at room temperature in the dark for times up to several weeks, and then probed optically with the same 532-nm beam as it was used in the previous experiments. Scanning the beam along the y -axis of the crystal on a path that intersected the previously damaged spot results in scattered light when the beam intersects the regions displaced slightly to the $+y$ and $-y$ side of the previously illuminated and damaged spot. In contrast, in areas where no PRD was created earlier, no PRD is observed. For this experiment the crystal is not heated in order to make sure that the transmitted beam does not create any additional optical damage.

We also observe that the PRD can be completely erased by homogeneously illuminating the crystal with an incandescent lamp for 30 minutes. After that exposure the beam diameter in the far field is within 1% of its original value. For applications, it is important to note that after erasing the optical damage with white light, the MgO:LN crystals can be used for subsequent experiments without any apparent change in properties.

Similar experiments are also conducted with different starting temperatures and temperature differences. All experiments reveal the same qualitative behavior. However, when the incident power is increased to $P = 100$ mW rather than the $P = 20$ μW used in the previous experiments, the strong distortion shown in Fig 5.6b is not observed, but the weak scattering in the wings of the beam (as in Fig. 5.6c) is still observed. The effect again persists for weeks in crystals stored in the dark.

It is very important to note that the beam is not distorted and no patterning occurred in any experiment when the z -faces of the MgO:LN crystal are short-circuited during heating, e.g. by painting silver conducting paste on the z -faces and connecting them with each other. Furthermore, conducting the experiment with sample CLN₂, photorefractive damage is not observed with 20 μW optical power and 100- μm beam diameter, whether or not a temperature step is applied during illumination. However, at higher laser powers (on the order of milliwatts) at room temperature the conventional bulk-photovoltaic PRD [77] is observed in CLN independent of heating whereas, as already noted, bulk-photovoltaic PRD is not observed in MgO:LN under these conditions.

5.3.2 Interferometry

5.3.2.1 Setup

A Zygo laser interferometer and Zygo MetroPro data processing software are used to image any whole-beam refractive index changes inside the crystals associated with the above observed optical damage, to compare with predictions from Sect. 5.2.3. Crystals are first exposed to 532-nm radiation and temperature changes as described in Sect. 5.3.1. However, since the spatial resolution of the Zygo interferometer is about 100 μm , it is necessary to generate a refractive index distribution of significantly greater spatial extent to have a reasonable number of pixels in the interferogram, which is accomplished by using a collimated 532-nm beam of 5-mm diameter rather than the 100- μm beam used in the previous experiments. Hence the illumination setup depicted in Fig. 5.5 is adjusted: A second lens is placed into the beam behind the first lens in order to have a collimated beam with diameter $d = 5$ mm. Thus only the large crystals CTIMgOLN₃, CTIMgOLN₄, and CLN₁ can be used in this experiment. However, the heating and illumination part of the experiment is performed in the same way as described in Sect. 5.3.1. Note that the temperature at the top of the large crystals is generally 0.4 °C lower than that at the bottom of the crystal,

but as the diameter of the optical beam is small compared to the crystal dimension, the effective pyroelectric field in the area where the beam illuminated the crystal could be seen as constant and, indeed, within the accuracy of measurement, no effect of the temperature gradient is measured. In the following we refer to the temperature measured at the bottom. The sample with initial temperature $T_i = 23$ °C is heated and equilibrated to temperature $T_i + \Delta T = T_f$ with no illumination (for approximately 15 minutes), after which illumination is initiated. This procedure ensures reproducibility of measurement conditions. Subsequent to illumination the crystal is short-circuited while cooling down to room temperature. Then the crystal is characterized with the Zygo interferometer. Note that in different experiments different illumination times are used, the longest illumination time used is 160 s.

The Zygo interferometer uses light at $\lambda = 632.8$ nm with an intensity that is orders of magnitudes smaller than the intensity of the green writing beam. The sample is placed in the interferometer with the x -axis almost parallel to the measurement beam, a slight tilt of the crystal inhibited multiple back-reflections into the detector. The Zygo MetroPro software is able to correct for that tilt later. The interferometer measures variations in the optical path length $\text{OPL} = \int_C n(s)ds$, where C is the geometrical path and s is the distance along the path C . Hence the optical path difference (OPD) does not only depend on the change in the refractive index, but also on the change in geometrical path. However, the Zygo MetroPro software is able to correct for OPDs caused by crystal thickness variations due to, e.g. curved or tilted surfaces. In addition, as a cross check, we also take measurements of the unprocessed crystals in order to measure OPD due to thickness variations, surfaces roughness, or refractive index inhomogeneities that are already present before the experiment is performed. Thus the interferometric data are corrected for these variations.

5.3.2.2 Results

Interferometric measurements with unprocessed as-grown $\text{MgO}:\text{LN}$ samples show that the crystal length L is constant between subsequent measurements to an accuracy of about half a wavelength, thus any larger OPD (compared to the unprocessed crystal) after heating, illumination, and short-circuiting can be attributed to refractive index changes Δn_{ill} , which can be determined as deviations from uniformity from the corrected OPD data. Note, the measurement procedure does not allow to determine absolute numbers for the refractive index, it can only determine refractive index deviations from uniformity.

Some typical results of the Zygo interferometer measurements after heating and subsequent illumination of a $\text{MgO}:\text{LN}$ crystal are shown in Fig. 5.7 for different illumination times. For these measurements sample CTIMgOLN₄ is used with $\Delta T = 2$ °C and $P = 150$ mW. Depicted are the OPDs within the crystal normalized to $2L$, i.e. the distance the light

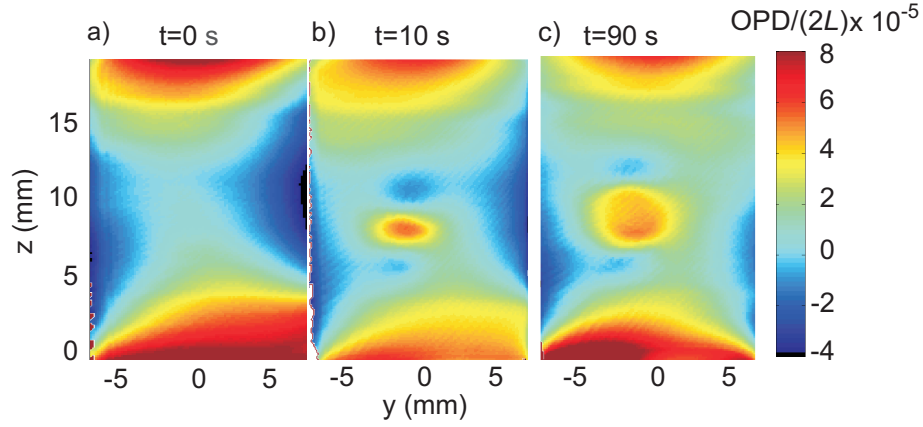


Figure 5.7: *OPD map of CTIMgOLN₄ for $\Delta T = 2^\circ\text{C}$ and $P = 150\text{ mW}$, a) unprocessed, b) after 10 s, and c) 90 s of illumination. Data are normalized to $2L$.*

travels within the crystal in the interferometric setup. The results shown in Fig. 5.7 are corrected for tilt and misalignment of the sample within the interferometer arm by using the Zygo MetroPro software. They are not corrected for crystal thickness variations, surface roughness errors, or as-grown refractive index inhomogeneities yet in order to show the significance and character of the effect. Prior to heating and illumination the crystal is examined with the Zygo interferometer in order to obtain the OPD map (Fig. 5.7a) of the as-grown crystal.

Then the sample is illuminated for 10 s using the experimental routine described in Sect. 5.3.2 without heating. After that the experiment is repeated with heating and subsequent illumination for 10 s (Fig. 5.7b). After this measurement the pattern is erased by illuminating the sample with white light homogeneously for 30 minutes. No OPD can be measured with respect to Fig. 5.7a after white light illumination. Then the heating-and-illumination experiment is repeated, in this case the illumination time is 90 s (Fig. 5.7c). It is important to note that it is not possible to place the crystal exactly at the same position in the illumination setup and the Zygo interferometer in every measurement. Therefore Fig. 5.7 shows slightly different crystal positions.

Figure 5.7a shows that no change in optical path length is observed without heating. This reveals that illumination itself does not cause thickness or refractive index variations. From Fig. 5.7a it becomes also obvious that the crystal surfaces are curved; this effect can also be seen in Figs. 5.7b and c. However, even though the surfaces are curved, one can clearly see in Fig. 5.7b that after heating and subsequent illumination for 10 s the optical path length is changed positively in the beam center. After heating and 90 s of illumination a shape similar to a flat-top profile develops as is shown in Fig. 5.7c. One can also see that the

change in optical path length cannot be attributed to a change in crystal thickness since it is an order of magnitude larger than the crystal thickness change measured before. The observed OPD in the illuminated area can solely be attributed to refractive index changes Δn_{ill} (according to Eq. 5.11). Thickness variations, e.g. due to temperature variations or the converse piezoelectric effect, can be excluded. Another remarkable feature is that a local negative refractive index change seems to develop in a lobe-like shape in regions along \mathbf{z} next to the positive refractive index changes in Figs. 5.7b and c.

In another experiment the crystal is slightly cooled. Although the temperature excursion in this case cannot be evaluated quantitatively, a refractive index measurement can be performed after illumination, using the same beam parameters as in Fig. 5.7. The refractive index profile looks very similar to Figs. 5.7b and c, but in this case the refractive index change in the beam center is negative and the side lobes are positive.

In order to quantify the z -dependence of the non-uniform refractive index change Δn_{ill} going through the beam center, the experiment is repeated varying the illumination times and intensities for sample CTIMgOLN₄. The same experimental routine of heating and illumination is used again with $\Delta T = 3$ °C and $P = 150$ mW. Maps of OPD as in Fig. 5.7 are obtained and not only corrected for tilts, but also for surface curvature of the crystal, surface roughness etc. From these data we determine $\Delta n_{\text{ill}}(y = 0, z, t)$ which is depicted in Fig. 5.8. The accuracy of the measured refractive index changes is estimated to be about 20%, due to a number of parameters that are not well controlled. In particular, although the crystal z -surfaces are electrically insulated from each other, screening of the pyroelectric field by external charges could not be inhibited, e.g. it is not possible to control how well the surface is cleaned, it is also not possible to control the humidity and other environmental factors which could lead to surface charge screening. Furthermore, temperature gradients are probably present near the crystal surfaces, and their influence on the pyroelectric field cannot be controlled. Another error source is the Zygo interferometer, which suffers from room temperature fluctuations that can easily be detected.

Figure 5.8 shows that with increasing illumination time a positive flat-top refractive index profile develops with negative side lobes in $+z$ and $-z$ directions. It also shows that there is a maximum refractive index change in the beam center. In Fig. 5.9 the normalized refractive index change in the beam center $\Delta n_{\text{ill}}(y = 0, z = 0, t)$ from Fig. 5.8 is plotted versus illumination time t (squares). The solid line represents the result of the FDTD simulations from Sect. 5.2.3 for $\tau_{\text{di}} = 14$ s. Note that, in contrast to the case of one-dimensional illumination (Sect. 5.2.2), the time dependence of the refractive index-change is not an exponential function, as was also seen to be the case for two-dimensional bulk-photovoltaic PRD in CLN [130].

In Fig. 5.10 the refractive index change $\Delta n_{\text{ill}}(y = 0, z, t = 20\text{s})$ is shown for different intensities but fixed illumination time $t = 20$ s. The developing flat-top refractive index

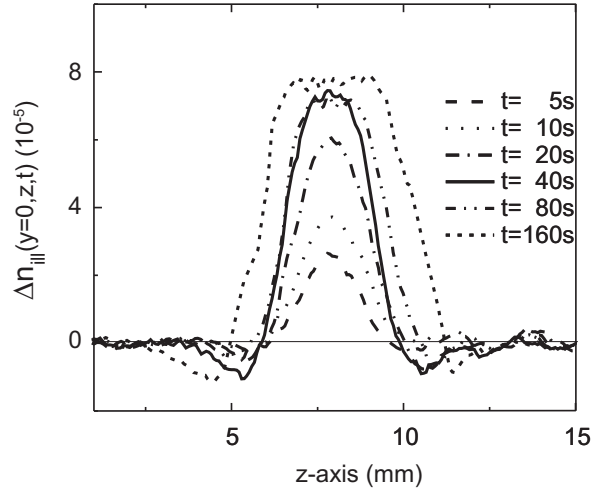


Figure 5.8: Non-uniform refractive index change $\Delta n_{\text{ill}}(y = 0, z, t)$ in CTIMgOLN_4 for different illumination times $t = 5, 10, 20, 40, 80, 160$ s. Experimental parameters are $\Delta T = 3$ °C and $P = 150$ mW.

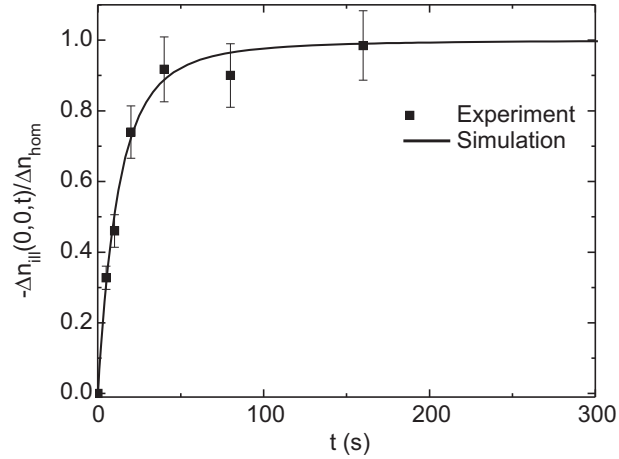


Figure 5.9: Normalized maximum refractive index change $\Delta n_{\text{ill}}(y = 0, z = 0, t)$ versus illumination time t (squares) in sample CTIMgOLN_4 . The solid line represents the result of the numerical simulation for $\tau_{\text{di}} = 14$ s.

profile can be seen again as well as the negative refractive-index side lobes.

The above experiments are also performed with sample CTIMgOLN_3 , and the same qualitative behavior is seen as was depicted in Figs. 5.7, 5.8, and 5.10 for sample CTIMgOLN_4 .

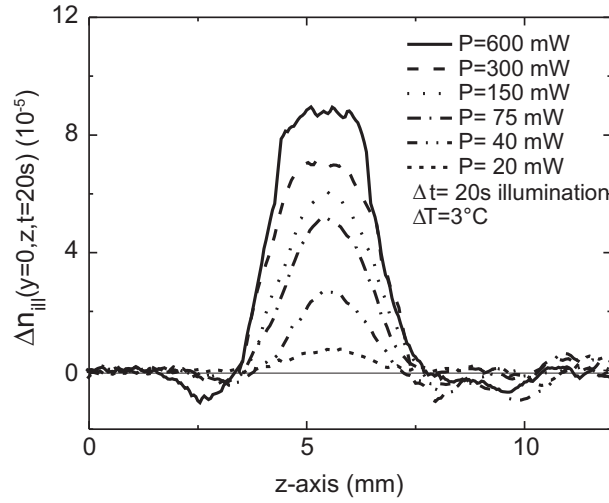


Figure 5.10: $\Delta n_{\parallel}(y=0, z, t=20\text{s})$ of sample CTIMgOLN_4 for different laser powers $P = 600, 300, 150, 75, 40, 20 \text{ mW}$ (largest to smallest refractive index change). Experimental parameters are $\Delta T = 3 \text{ }^\circ\text{C}$ and the illumination time $t = 20 \text{ s}$.

In contrast, in CLN_1 no refractive index change profile can be measured with the Zygo interferometer within the sensitivity limit of about 2×10^{-6} and a maximum illumination time of 160 s. This also is consistent with the observation that in CLN no beam distortion is observed after heating and illumination with low light intensity.

5.3.3 Determination of the specific photoconductivity and the bulk-photovoltaic coefficient

In the previous theoretical description it has been pointed out that knowledge of β , σ_{photo} (or the specific photoconductivity κ), and σ_{d} is crucial for the understanding of the pyroelectrically-induced PRD. Experimental data about σ_{photo} and β in CLN and $\text{MgO}:\text{LN}$ already exist [84], however crystals grown 10 years or more ago had different impurity levels than the ones grown recently, and quantities like κ strongly depend on impurity levels. In a more recent study, σ_{photo} and β were determined over a wide intensity range for CLN, but not for $\text{MgO}:\text{LN}$ crystals [134]. Hence it is necessary to measure these quantities on crystals that have been grown under the same conditions as the crystals used in the PRD damage experiments described in Sect. 5.3.2.2. By determining κ and σ_{d} one can calculate τ_{di} (Eq. 5.16) and compare it to the τ_{di} determined in Fig. 5.9.

5.3.3.1 Setup

For these measurements we use a setup similar to an electric-field-poling cell. The setup is depicted in Fig. 5.11 [137].

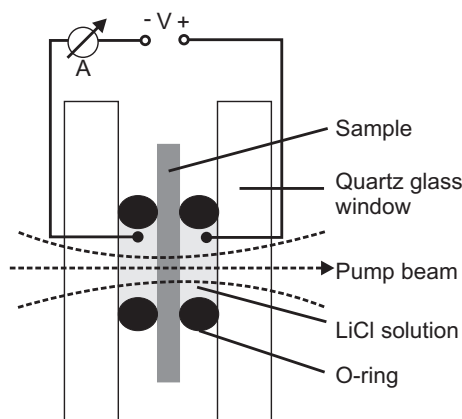


Figure 5.11: *Schematic of the apparatus for measurement of photoconductivity and bulk-photovoltaic current.*

This apparatus is constructed to allow electrical contacting of the surfaces without significant absorption of the incident laser power in the electrical contacts, thereby minimizing heating and the interference from the concomitant pyroelectric currents. Typical photocurrents in these samples are on the order of pA, so care must be taken to minimize these and other interfering currents. In this setup the crystal sample (typical dimension $10 \times 10 \times 1 \text{ mm}^3$) is clamped with two silicone rubber o-rings between two quartz-glass plates. An electrolyte, saturated lithium chloride (LiCl) solution, is filled between the gaps inside the o-rings. The two LiCl-filled chambers are electrically connected with platinum wires to a Keithley 618 programmable picoammeter which measures the electrical current flowing through the sample in the z -direction and which could also apply a voltage in order to measure conductivity. The 514-nm-wavelength output of an argon-ion laser is focused through the quartz-glass windows, the electrolyte, and the sample. Since no 532-nm source is available for these measurements, we choose the 514-nm Ar-laser line. This wavelength is chosen to be the strongest Ar-ion laser line that is closest to $\lambda = 532 \text{ nm}$, which was the writing wavelength in the experiments described in Sect. 5.3.2.2. The light intensity is varied over the range $10^1\text{-}10^4 \text{ W/cm}^2$ by translating the focusing lens on a translation stage, thus only intensity changed but not the power of the laser beam. With this arrangement the heat input due to residual absorption in the crystal is constant, minimizing pyroelectric current artifacts associated with absorption-induced temperature changes in the crystal. The following currents are measured

- Bulk-photovoltaic current I_{pv} : laser on, voltage off
- Dark current I_{d} : laser off, voltage on, i.e. 10 V for MgO:LN and 80 V for CLN
- Total current I_{tot} : laser on and voltage on, 10 V for MgO:LN and 80 V for CLN

Then the following quantities are determined with E being the applied electric field:

- Photoconductive current $I_{\text{photo}} = I_{\text{tot}} - I_{\text{d}} - I_{\text{pv}}$
- $I_{\text{photo}}/(EP)$. If this ratio is constant, then it is $\kappa = I_{\text{photo}}/(EP)$.
- I_{pv}/P . If this ratio is constant, then it is $\beta = I_{\text{pv}}/P$.

5.3.3.2 Results and discussion of the electric current measurements

In this section measurement results are presented for samples CLN_2 and CTIMgOLN_1 . It is not possible to measure I_{tot} and I_{d} for samples CTIMgOLN_4 , CTIMgOLN_3 , and CLN_1 directly because of their crystal dimensions. However, sample CTIMgOLN_1 was produced under comparable crystal growth conditions as CTIMgOLN_4 and CTIMgOLN_3 , and sample CLN_2 is comparable to CLN_1 .

The ratio $I_{\text{photo}}/(PE)$ for samples CLN_2 and CTIMgOLN_1 is shown in Fig. 5.12. The error for $I_{\text{photo}}/(PE)$ is about $\pm 20\%$ (repeated measurements) because the measurements are extremely sensitive to various parameters, e.g. vibrations, temperature changes and leakage currents. In both, MgO:LN and CLN crystals, $I_{\text{photo}}/(PE)$ can be seen as nearly constant, i.e. $I_{\text{photo}}/(PE)$ varies by less than a factor of ≈ 3 over an intensity range of three orders of magnitude. Hence $\kappa = I_{\text{photo}}/(PE)$ can be determined for MgO:LN and CLN. Figure 5.12 also clearly shows that κ is about 30 times smaller in CLN than in MgO:LN.

The photocurrents at light intensities in the range $I = 0.1 - 10 \text{ W/cm}^2$ are smaller than our resolution limit of 10 fA for the beam diameters available here, so we assume from the near-constancy of the results for κ over the measured range of $10^1 - 10^4 \text{ W/cm}^2$ that the same values are applicable at lower intensities. The specific photoconductivity κ of MgO:LN and CLN is also determined for many other MgO:LN and CLN samples that are not listed here and which came from various vendors and different crystal growth runs. It turns out that the values for κ for various MgO:LN crystals (5-mol % MgO-doped) vary between 0.1 and 0.5 pS cm/W. For different CLN crystals values for κ are in the range 0.001-0.008 pS cm/W.

It is not feasible to determine σ_{d} . The minimum resolvable current in our apparatus, 10 fA, exceeds the dark currents in both CLN and MgOLN, so it is not possible to measure the

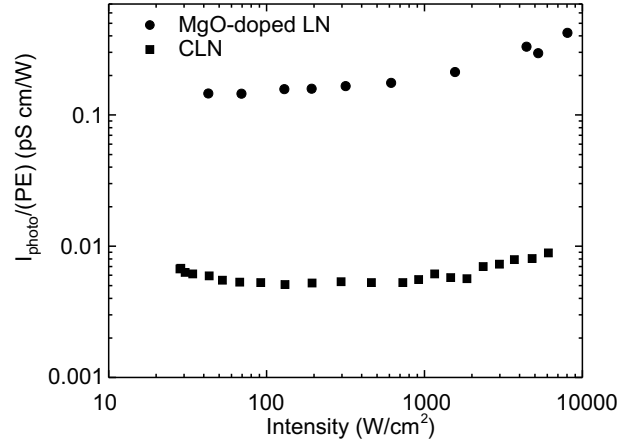


Figure 5.12: Ratio $I_{\text{Photo}}/(PE)$ vs. intensity for CLN (squares) and MgO:LN (circles). In the case $I_{\text{Photo}}/(PE)$ is constant, the specific photoconductivity κ is given by $\kappa = I_{\text{Photo}}/(PE)$.

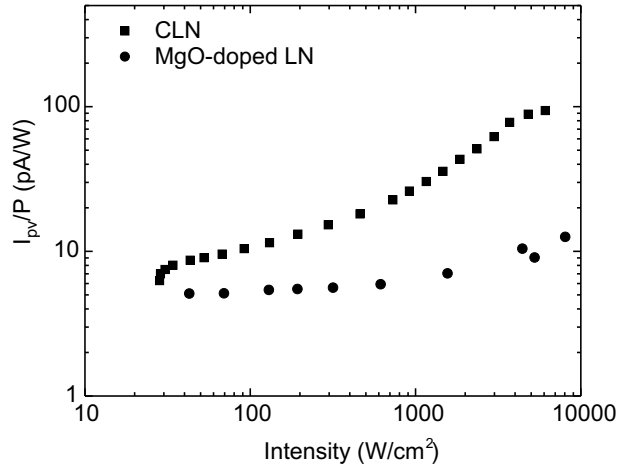


Figure 5.13: Ratio I_{pv}/P versus intensity for CLN (squares) and MgO:LN (circles). In the case I_{pv}/P is constant, the bulk-photovoltaic coefficient β is given by $\beta = I_{\text{pv}}/P$.

dark conductivities with the maximum bias voltages available. The upper limit for σ_d in our measurements is $\sigma_d \leq 5 \times 10^{-16} (\Omega\text{cm})^{-1}$. This observation is consistent with other measurement results of σ_d in MgO:LN [128].

The intensity dependence of I_{pv}/P is depicted in Fig. 5.13. The error for I_{pv}/P is about

$\pm 10\%$ (repeated measurements). Figure 5.13 shows that I_{pv}/P is constant for MgO:LN, hence $\beta = I_{\text{pv}}/P$. In the case of CLN I_{pv}/P is not constant for higher light intensities, and thus $\beta = I_{\text{pv}}/P$ is only valid for small light intensities. This is in agreement with [134]. For higher light intensities a nonlinear intensity dependence has to be taken into account [138]. Figure 5.13 also shows that I_{pv}/P is up to one order of magnitude smaller in MgO:LN than in CLN.

As already mentioned, we are not able to make reliable photocurrent measurements in the intensity range $I = 0.1 - 10 \text{ W/cm}^2$, but can again assume that the value for β at $I = 0.1 - 10 \text{ W/cm}^2$ is similar to the closest β -data point in Fig. 5.13.

5.4 Discussion

The experimental results clearly show that pyroelectrically-induced PRD exists in MgO:LN . We concluded that the observed PRD reported in Sect. 5.3.1 and Sect. 5.3.2 are induced by the pyroelectric effect, because the refractive index changes only when the sample is heated and when the sample z -facets are electrically insulated from each other. It is also shown that the sign of the refractive index change depends on the sign of the temperature change. In contrast, the sign and magnitude of the changes in the refractive index due to the bulk photovoltaic effect do not depend on small temperature changes.

The result shown in Fig. 5.7 depicts the OPD along the x -axis, hence it is a projection from 3D to 2D, and refractive index inhomogeneities along the x direction can in principle lead to misinterpretation, but the experimental results shown in Figs. 5.7 and 5.8 agree well with the FDTD simulations in Fig. 5.2 and in Fig. 5.3 within measurement accuracy. Even the side lobes can be identified both, in simulations and experimental results. Simulations and experimental results also agree for the time-dependence of the refractive index change Fig. 5.9. The theoretical curve with $\tau_{\text{di}} = 14$ s fits the data very well. And as a cross check according to Eq. 5.16, this value of τ_{di} corresponds to a specific photoconductivity $\kappa = 0.27$ pS cm/W which agrees with obtained data in Fig. 5.12. Figure 5.10 shows why it seems as if at higher laser intensities there is no PRD. Indeed there is a refractive index change, the higher intensity just leads to a faster build-up of the flat-top profile so that the beam is not disturbed. This also explains the observations reported in Sect. 5.3.1.2 that PRD seems not to occur at higher laser powers. So far it was widely assumed that suppression of PRD in MgO:LN also means that there are not any light-induced refractive index changes. Our measurements show that this assumption does not longer hold. Even if a laser beam is not distorted, writing permanent refractive index channels into MgO:LN can be an obstacle for nonlinear-optical application, because as soon as the beam shape is slightly changed, e.g. due to a setup change, these changes can at least temporarily limit the performance of the device.

Maximum refractive index change The expected theoretical maximum refractive index change of $\Delta n_{\text{ill}}(y=0, z=0)_{\text{max}} = -\Delta n_{\text{hom}} = 1.3 \times 10^{-4}$ for $\Delta T = 3$ °C (Eq. 5.12) is similar to the experimentally observed $\Delta n_{\text{ill}}(y=0, z=0)_{\text{max}} = 0.8 \times 10^{-4}$; the origin of the discrepancy of a factor 1.5 is not clear. Since $\Delta n_{\text{hom}} \propto \mathbf{E}_{\text{pyro}}$, this result indicates that the actual $|\mathbf{E}_{\text{pyro}}|$ is smaller than expected. This observation is a common issue with pyroelectric fields, since external charge screening and other effects can lower the measured $|\mathbf{E}_{\text{pyro}}|$ [114,123]. It also has to be taken into account that in our apparatus the top always is a bit cooler than the bottom of the crystal, hence the actual ΔT in the area of the beam might be lower than the temperature change measured at the bottom. For the 0.4 °C degree temperature difference discussed in Sect. 5.3.2, this effect would induce a difference

in the refractive index change between top and bottom by about 2×10^{-5} . Thus this might at least partly explain the discrepancy in the refractive index changes. Although $|\mathbf{E}_{\text{pyro}}|$ is smaller than expected, effects such as partial surface screening or temperature errors do not affect the time dependence, which is consistent with time constants calculated from transport measurements described in Sect. 5.3.3.2.

The refractive index inhomogeneity due to heating and illumination of MgO:LN crystals is correlated with the beam distortions in Fig. 5.6b. Similar to conventional bulk-photovoltaic PRD, it appears that the refractive index inhomogeneity in the illuminated area acts as an initial light scatterer that seeds subsequent holographic amplification [78] which in turn leads to the diffuse and distorted beam shapes shown in Fig. 5.6b. Quantitative analysis of the dynamics of this process remains a topic for future research. After the flat-top refractive index profile develops, the refractive index inhomogeneity is located in the wings of the beam, reducing the seed power available for the holographic amplification so that the far-field scattering is reduced and the beam shape is restored after some time.

Comparison between MgO:LN and CLN Note that pyroelectrically-induced PRD does not occur in our experiments with CLN crystals under the same experimental conditions. In fact our results show that the behavior of MgO:LN is more similar to that of a medium having no bulk-photovoltaic effect, such as SBN [114], than to CLN which has a strong bulk-photovoltaic effect. From Figs. 5.12 and 5.13 the differences in transport properties between CLN and MgO:LN becomes clear: The bulk photovoltaic field E_{pv} can be calculated from the measured values of β and κ in Sect. 5.3.3.2 according to $E_{\text{pv}} = -\beta/\kappa$. This leads to the observation that $|E_{\text{pv}}|$ in MgO:LN is about two orders of magnitude smaller than $|E_{\text{pv}}|$ in CLN and also two orders of magnitude smaller than $|\mathbf{E}_{\text{pyro}}|$ under typical conditions in these experiments. This observation reconfirms the assumption made in Sect. 5.2.2 that $|E_{\text{pv}}| \ll |\mathbf{E}_{\text{pyro}}|$ for MgO:LN and the parameters used in these experiments, and justifies the neglect of bulk-photovoltaic effects in our analysis of the observed beam scattering in MgO:LN. Another difference between MgO:LN and CLN is the magnitude of the dielectric time constant τ_{di} , which according to Eq. 5.16 is correlated to the specific photoconductivity κ . The pyroelectric field in MgO:LN is screened rapidly in the illuminated parts of the crystal, $\tau_{\text{di}} = 14$ s (Fig. 5.9). In contrast, in CLN screening of \mathbf{E}_{pyro} is much slower than in MgO:LN because of the more than 30 times smaller κ (Fig. 5.12). Hence, it is possible that pyroelectrically-induced PRD also occurs in CLN, but cannot be measured in the observation time window due to the much longer characteristic time constant.

5.5 Outlook and conclusion

Outlook Although pyroelectrically-induced PRD is an obstacle for any application that depends on homogeneous refractive indices such as OPOs, we showed a path to avoid build-up of pyroelectrically-induced PRD. In Sect. 5.2.4.2 it was shown that periodic poling should reduce E_{pyro} up to a factor of 140, for the experimental parameters used there. This suppression strongly depends on the duty cycle of the poling. Thus one way to reduce the damage is to ensure that the PPMgLN duty cycle is as close to 50 % as possible, and that there are no parts in the crystal where the light does not go through the PPLN grating. Additionally one can increase the conductivity by illuminating the whole crystal from above with intense blue light which increases the conductivity of the crystals as our intensity-dependent experiments on the photoconductivity in CLN and $\text{MgO}:\text{LN}$ show in Fig. 5.12, thus electric fields cannot build up. The illumination scheme has already successfully been applied for Q-Switch devices where pyroelectric fields also are an obstacle [135]. A schematic of the short-circuit setup is shown in Fig. 5.14.

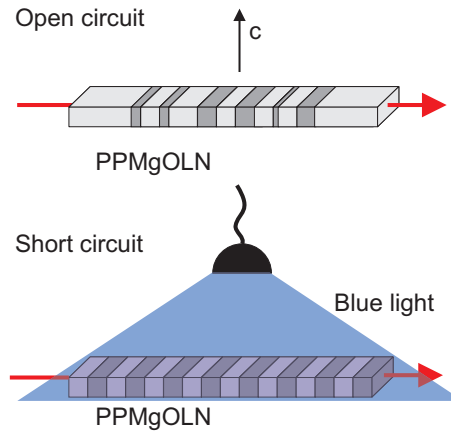


Figure 5.14: Schematic for insufficient electric short-circuiting of the PPLN crystals (upper picture) and proposed schematic to avoid pyroelectrically-induced PRD (lower picture).

There might also be a positive aspect of being able to change the refractive index in $\text{MgO}:\text{LN}$ due to pyroelectrically-induced PRD, e.g. it provides a way of writing holograms in $\text{MgO}:\text{LN}$ with visible light, because the light intensities used to create PRD in an externally heated crystal are rather low. Furthermore, instead of using \mathbf{E}_{pyro} , one might simply apply an external field \mathbf{E}_0 which makes the experiment more controllable. If it is also possible to fix the holograms it would be possible to write Bragg gratings into $\text{MgO}:\text{LN}$ crystals and use them for optical applications and combine them with the frequency conversion applications of $\text{MgO}:\text{LN}$.

Conclusion It was demonstrated, theoretically and experimentally, that 5 mol.% MgO-doped LiNbO_3 , which is widely believed to be optical-damage resistant, can indeed suffer from photorefractive damage due to the pyroelectric effect if the crystal is heated and illuminated at the same time. Heating led to the formation of a pyroelectric field, and illumination screened this field in the illuminated region so that an inhomogeneous total electric field and, hence, an inhomogeneous refractive index change was created. We showed that the beam recovery that was observed after some time with illumination could not be attributed to a recovery of the refractive index inhomogeneity, in fact long illumination times or increasing the light intensity lead to the formation of a flat-top refractive index profile. Our experiments and simulations have also proven that, with respect to pyroelectrically-induced PRD, the behavior of MgO:LN is more similar to that of a medium having no bulk-photovoltaic effect, such as SBN [114], than to CLN which has a large bulk-photovoltaic effect. This supposition was confirmed by measurements of the specific photoconductivity κ and the bulk-photovoltaic field E_{pv} : The specific conductivity κ was found to be more than 30 times smaller and E_{pv} is up to two orders of magnitude larger in CLN than in MgO:LN. This difference in transport properties partly explained why the same beam distortion could not be measured in CLN, because in CLN the small photoconductivity cannot screen \mathbf{E}_{pyro} in experimentally relevant time scales. Finally we showed theoretically that beam self heating from absorption of optical beams also causes pyroelectrically induced photorefractive effects and that they can be suppressed by two orders of magnitude if the MgO:LN crystal is periodically poled and the duty cycle of the poling is 50 %.

Chapter 6

Summary

One of the most important mechanisms of light-matter interaction is photon absorption, so-called optical absorption. There are fields in technology and science where photon absorption is detrimental, e.g. nonlinear-optical applications are very sensitive to absorption, especially in cases where a pump power threshold has to be overcome as is the case for optical parametric oscillation. Furthermore, heat accumulation and charge excitation due to photon absorption lead to refractive index changes which cause beam distortion and therefore disturb the phase-matching condition.

One of the most attractive non-linear optical materials is congruent lithium niobate (LiNbO_3). However, the achievable output power in nonlinear-optical devices using congruent LiNbO_3 crystals (CLN) is limited due to photorefractive damage (PRD) that is caused by the bulk-photovoltaic effect. One way to suppress bulk-photovoltaic PRD is to dope LiNbO_3 with at least 5 mol% magnesium oxide (MgO:LN), but doping does not solve the problem of optical absorption. Calculations show that an absorption coefficient of 0.0001 cm^{-1} can already be a serious obstacle for nonlinear-optical applications. However, absorption spectroscopic data of CLN and MgOLN reported in literature were limited to detect absorption coefficients on the order of 0.01 cm^{-1} only, so that absorption bands smaller than that could not be resolved.

In this thesis we present absorption measurements with optical-grade CLN and MgO:LN using a conventional grating spectrophotometer. We show that it is feasible to resolve absorption coefficients in CLN and MgO:LN that are on the order of 0.0001 cm^{-1} which is an improvement of about two orders of magnitude in comparison to literature data.

First we study the spectral range 350-800 nm. Comparison of spectra from CLN and MgO:LN crystals to absorption spectra of intentionally transition-metal doped LiNbO_3 and MgO:LN crystals and cross-check with mass spectroscopy data clearly indicates the

characteristic absorption bands to be caused by Cr impurities. The amplitudes of the observed Cr^{3+} absorption bands have amplitudes on the order of $0.001 - 0.01 \text{ cm}^{-1}$ and decrease from the top to the bottom of a crystal boule. Further impurities contributing to absorption are Fe, Cu, Ni, and, to some extent, Mn.

In the range 800-2000 nm the spectrophotometric accuracy cannot be improved, however, spectra of intentionally transition-metal codoped MgO:LN crystals show that impurity concentrations of Ni, Cu, and Fe on the order of 0.1 – 1 wt. ppm respectively can cause absorption bands in the spectral range 1000-1500 nm that are larger than 0.0001 cm^{-1} .

Absorption measurements in MgO:LN and CLN in the range 2000-2950 nm reveal so-far unknown absorption bands between 2350-2800 nm for ordinary and extraordinary light polarization, with amplitudes on the order of $\alpha = 0.0005 - 0.0015 \text{ cm}^{-1}$. Application of a high-temperature annealing procedure reduces the hydrogen content of MgO:LN and CLN by one order of magnitude and decreases the absorption bands by up to an order of magnitude as well, indicating that the newly-discovered bands are related to the hydrogen impurities. Successful application of annealed periodically poled CLN in a 1550-nm pumped singly-resonant CW OPO, which crucially depends on low optical absorption in the spectral range 2500 – 2800 nm, is demonstrated .

Finally it is theoretically and experimentally demonstrated that MgO:LN suffers from PRD if a pyroelectric field is created by homogenous heating of the crystal and the crystal is illuminated with visible, spatially inhomogeneous radiation at the same time or directly after heating. The reason is that the illumination leads to an increased photoconductivity in the illuminated area which causes fast screening of the pyroelectric field there. This creates an inhomogeneous electric field and, due to the electro-optic effect, an inhomogeneous refractive index change. After some time with illumination a flat-top refractive index profile develops which partly reverses the beam distortion. Pyroelectrically-induced PRD does not occur in CLN within the time span of the experiment. We show theoretically that pyroelectrically-induced PRD also results from the spatially inhomogeneous thermal fields associated with beam self heating from absorption of optical beams. This effect makes pyroelectrically-induced PRD so important for nonlinear-optical applications using MgO:LN: If there is a strong pump laser beam which heats the crystal due to absorption and which also inevitably produces some parasitic visible radiation, pyroelectrically-induced PRD can occur. The effect can be avoided by inducing a volume-screening mechanism such as flood illumination with blue light or periodic poling with near-perfect 50 % duty cycle, which reduces the pyroelectric field up to two orders of magnitude.

Both, optical absorption and pyroelectrically-induced PRD, limit the usability of MgO:LN crystals in high-power applications. The solutions to suppress residual absorption and pyroelectrically-induced PRD, that are shown in this thesis, make new and more efficient high-power nonlinear applications feasible.

Bibliography

- [1] A. A. Lacis and J. E. Hansen, “A parameterization for the absorption of solar radiation in the earth’s atmosphere”, *J. Atmosph. Sci.* **31**, 118 (1973).
- [2] M. Calvin, “The path of carbon in photosynthesis”, *Science* **165**, 879 (1962).
- [3] Govindjee, J. T. Beatty, H. Gest, and J. Allen, eds. *Discoveries in photosynthesis*. Springer Netherlands, 2006.
- [4] M. Gratzel, “Photoelectrochemical cells”, *Nature* **414**, 338 (2001).
- [5] E. I. Moses, R. N. Boyd, B. A. Remington, C. J. Keane, and R. Al-Ayat, “The National Ignition Facility: Ushering in a new age for high energy density science”, *Physics of Plasmas* **16**, 041006–1 (2009).
- [6] C. W. Carr, H. B. Radousky, and S. G. Demos, “Wavelength dependence of laser-induced damage: Determining the damage initiation mechanism”, *Phys. Rev. Lett.* **91**, 127402–1 (2003).
- [7] S. B. Sutton, A. E. Erlandson, R. A. London, K. R. Manes, C. D. Marshall, C. S. Petty, R. Pierce, L. K. Smith, L. E. Zapata, J. Beullier, and B. Birel, “Thermal recovery of the NIF amplifiers”, in *Proceeding of SPIE*, 1999.
- [8] K. K. Wong *Properties of lithium niobate*. INSPEC, 2002.
- [9] D. A. Bryan, R. Gerson, and H. E. Tomaschke, “Increased optical damage resistance in lithium niobate”, *Appl. Phys. Lett.* **44**, 847 (1984).
- [10] O. F. Schirmer, O. Thiemann, and M. Wöhlecke, “Defects in LiNbO₃ - I. Experimental aspects”, *J. Phys. Chem. Solids* **52**, 185 (1991).
- [11] M. G. Pullen, J. J. Chapman, and D. Kielpinski, “Efficient generation of > 2 W of green light by single-pass frequency doubling in PPMgLN”, *Appl. Opt.* **47**, 1397 (2008).

- [12] H. Furuya, A. Morikawa, K. Mizuuchi, and K. Yamamoto, “High-beam-quality continuous wave 3 W green-light generation in bulk periodically poled MgO:LiNbO₃”, *Jap. J. Appl. Phys.* **45**, 6704 (2006), no. 8B.
- [13] O. A. Louchev, N. E. Yu, S. Kurimura, and K. Kitamura, “Nanosecond pulsed laser energy and thermal field evolution during second harmonic generation in periodically poled LiNbO₃ crystals”, *J. Appl. Phys.* **98**, 113103;1 (2005).
- [14] A. Henderson and R. Stafford, “Intra-cavity power effects in singly resonant cw OPOs”, *Appl. Phys. B* **85**, 181 (NOV 2006).
- [15] L. Chaoyan, B. Yong, Y. Feng, W. Zhichao, X. Yiting, W. Yuanbin, G. Hongwei, C. Dafu, and X. Zuyan, “106.5 W high beam quality diode-side-pumped Nd:YAG laser at 1123 nm”, *Opt. Express* **18**, 7923 (2010).
- [16] J. C. Maxwell *A Treatise of electricity & magnetism*. Dover Publications, 1873.
- [17] F. Träger, ed. *Springer Handbook of Lasers and Optics*. Springer, 2007.
- [18] L. Kovacs, G. Ruschhaupt, K. Polgar, G. Corradi, and M. Wöhlecke, “Composition dependence of the ultraviolet absorption edge in lithium niobate”, *Appl. Phys. Lett.* **70**, 2801 (1997).
- [19] R. W. Boyd *Nonlinear Optics*. Academic Press, 2008.
- [20] J. A. Armstroing, N. Bloembergen, J. Ducuing, and P. S. Pershan, “Interactions between light waves in a nonlinear dielectric”, *Phys. Rev.* **127**, 1918 (1962).
- [21] M. M. Fejer, G. A. Magel, D. H. Jundt, and R. L. Byer, “Quasi-phase-matched second harmonic generation: Tuning and tolerances”, *IEEE J. Quantum Electr.* **28**, 2631 (1992).
- [22] K. Nakamura, J. Kurz, K. Parameswaran, and M. M. Fejer, “Periodic poling of magnesium-oxide-doped lithium niobate”, *J. Appl. Phys.* **91**, 4528 (2002).
- [23] A. M. Prokhorov and Y. S. Kuz’minov *Physics and chemistry of crystalline lithium niobate*. Adam Hilger, 1990.
- [24] T. Volk and M. Wöhlecke *Lithium Niobate*. Springer, 2008.
- [25] R. S. Weis and T. K. Gaylord, “Lithium niobate: Summary of physical properties and crystal structure”, *Appl. Phys. A* **37**, 191 (1985).
- [26] R. L. Byer, “Quasi-phasesmatched nonlinear interactions and devices”, *J. Nonlinear Optical Physics & Materials* **4**, 549 (1997).

-
- [27] D. A. Roberts, "Simplified characterization of uniaxial and biaxial nonlinear optical crystals: A plea for standardization and nomenclature and conventions", *IEEE J. Quantum Electr.* **28**, 2057 (1992).
- [28] M. Yamada, N. Nada, M. Saitoh, and K. Watanabe, "First-order quasi-phase matched LiNbO₃ waveguide periodically poled by applying an external field for efficient blue second-harmonic generation", *Appl. Phys. Lett.* **62**, 435 (1993).
- [29] G. D. Miller, R. G. Batchko, W. M. Tulloch, D. R. Weise, M. M. Fejer, and R. L. Byer, "42%-efficient single-pass cw second-harmonic generation in periodically poled lithium niobate", *Opt. Lett.* **22**, 1834 (1997).
- [30] T. Bartholomäus, K. Buse, C. Deuper, and E. Krätzig, "Pyroelectric coefficients of LiNbO₃ crystals of different compositions", *Phys. Stat. Sol. A* **142**, 55 (1994).
- [31] K. Nassau, H. J. Levinstein, and G. Loiacono, "Ferroelectric lithium niobate. 1. Growth, domain structure, dislocations and etching", *J. Phys. Chem. Solids* **27**, 983 (1966).
- [32] G. Dhanaraj, K. Byrappa, V. Prasad, and M. Dudley, eds. *Springer handbook of crystal growth*. Springer Verlag, 2010.
- [33] D. Berben, K. Buse, S. Wevering, M. Herth, P. Imlau, and T. Woike, "Lifetime of small polarons in iron-doped lithium-niobate crystals", *J. Appl. Phys.* **87**, 1034 (2000).
- [34] O. F. Schirmer, M. Imlau, C. Merschjann, and B. Schoke, "Electron small polarons and bipolarons in LiNbO₃", *J. Phys. Cond. Matt.* **21**, 29 (2009).
- [35] C. Merschjann, D. Berben, M. Imlau, and M. Wöhlecke, "Evidence for two-path recombination of photoinduced small polarons in reduced LiNbO₃", *Phys. Rev. Lett.* **96**, 186404 (2006).
- [36] C. Merschjann, B. Schoke, D. Conradi, M. Imlau, G. Corradi, and K. Polgar, "Absorption cross sections and number densities of electron and hole polarons in congruently melting LiNbO₃", *J. Phys.: Cond. Matter* **21**, 1 (2009).
- [37] O. F. Schirmer and D. Von der Linde, "Two-photon- and x-ray-induced Nb⁴⁺ and O⁻ small polarons in LiNbO₃", *Appl. Phys. Lett.* **33**, 35 (1978).
- [38] J. Koppitz, O. F. Schirmer, and A. I. Kuynetsov, "Thermal dissociation of Bipolarons in reduced undoped LiNbO₃", *Europhys. Lett.* **4**, 1055 (1987).
- [39] G. E. Peterson, A. M. Glass, A. Carnevale, and P. M. Bridenbaugh, "Control of laser damage in LiNbO₃", *J. Am. Ceram. Soc.* **56**, 278 (1973).

- [40] P. Günter and J.-P. Huignard, eds. *Photorefractive materials and their applications*. Springer Verlag, 1988.
- [41] M. Kösters, B. Sturman, P. Werheit, D. Haertle, and K. Buse, “Optical cleaning of congruent lithium niobate crystals”, *Nature Photonics* **3**, 510 (2009).
- [42] A. M. Glass, “Optical spectra of Cr³⁺ impurity ions in ferroelectric LiNbO₃ and LiTaO₃”, *J. Chem. Phys.* **50**, 1501 (1969).
- [43] J. Díaz-Caro, J. García-Solé, D. Bravo, J. A. Sanz-García, F. J. López, and F. Jaque, “MgO codoping-induced change in the site distribution of Cr³⁺ ions in LiNbO₃”, *Phys. Rev. B* **54**, 13042 (1996).
- [44] G. Boulon, “Optical transitions of trivalent neodymium and chromium centres in LiNbO₃ crystal host materials”, *Structure and Bonding* **107**, 1 (2004).
- [45] H. Kurz, E. Krätzig, W. Keune, H. Engelmann, U. Gonser, B. Dischler, and A. Rüber, “Photorefractive centers in LiNbO₃, studied by optical-, Moessbauer- and EPR-Methods”, *Appl. Phys.* **12**, 355 (1977).
- [46] M. G. Clark, F. J. DiSalvo, A. M. Glass, and G. E. Peterson, “Electronic structure and optical index damage of iron-doped lithium niobate”, *J. Chem. Phys.* **59**, 6209 (1973).
- [47] L. Arizmendi, J. M. Cabrera, and F. Agulló-López, “Optical absorption spectra of nickel doped lithium niobate”, *Ferroelectrics* **26**, 823 (1980).
- [48] U. Hartwig, K. Peithmann, B. Sturman, and K. Buse, “Strong permanent reversible diffraction gratings in copper-doped lithium niobate crystals caused by a zero-electric-field photorefractive effect”, *Appl. Phys. B* **80**, 227 (2005).
- [49] N. N. Sirota and V. P. Yarunichev, “Absorption spectra of lithium niobate with transition metal impurities in the region 0.3-2.0 μm ”, *Zhurnal Prikladnoi Spektroskopii* **25**, 650 (1975).
- [50] Y. Yang, D. Psaltis, M. Luennemann, D. Berben, and K. Buse, “Photorefractive properties of lithium niobate crystals doped with manganese”, *J. Opt. Soc. Am. B* **20**, 1491 (2003).
- [51] H. J. Levinstein, A. A. Ballmann, R. T. Denton, A. Ashkin, and J. M. Dziedzic, “Reduction of the susceptibility to optically induced index inhomogeneities in LiTaO₃ and LiNbO₃”, *J. Appl. Phys.* **38**, 3101 (1967).

-
- [52] G. Malovichko, V. Grachev, E. Kokanyan, and O. Schirmer, “Axial and low-symmetry centers of trivalent impurities in lithium niobate: Chromium in congruent and stoichiometric crystals”, *Phys. Rev. B* **59**, 9113 (1999).
- [53] C. Zaldo, C. Prieto, H. Dexpert, and P. Fessler, “Study of the lattice sites of Ti and Ni impurities in LiNbO single crystals, by means of x-ray absorption spectroscopy”, *J. Phys.: Condens. Matter* **3**, 4135 (1991).
- [54] M. Paul, M. Tabuchi, and A. R. West, “Defect structure of Ni, Co-doped LiNbO₃ and LiTaO₃”, *Chem. Mater.* **9**, 3206 (1997).
- [55] J. R. Herrington, B. Dischler, A. Rauber, and J. Schneider, “Optical study of the stretching absorption band near 3 microns from OH[−] defects in LiNbO₃”, *Solid State Commun.* **12**, 351 (1973).
- [56] J. Cabrera, J. Olivares, M. Carrascosa, J. Rams, R. Muller, and E. Dieguez, “Hydrogen in lithium niobate”, *Adv. Phys.* **45**, 349 (1996).
- [57] W. Bollmann and H. Stohr, “Incorporation and mobility of OH-ions in LiNbO₃ crystals”, *Phys. Stat. Sol. A* **39**, 477 (1977).
- [58] R. G. Smith, D. B. Fraser, R. T. Denton, and T. C. Rich, “Correlation in reduction in optically induced refractive-index inhomogeneity with OH content in LiTaO₃ and LiNbO₃”, *J. Appl. Phys.* **39**, 4600 (1968).
- [59] L. Kovacs, M. Wohlecke, A. Jovanovic, K. Polgar, and S. Kapphan, “Infrared-absorption study of the OH vibrational band in LiNbO₃ crystals”, *J. Phys. and Chem. of Solids* **52**, 797 (1991).
- [60] A. Forster, S. Kapphan, and M. Wohlecke, “Overtone spectroscopy of the OH and OD stretch modes in LiNbO₃”, *Phys. Stat. Sol. B* **143**, 755 (1987).
- [61] A. Grone and S. Kapphan, “Higher vibrational states of OH/OD in the bulk of congruent LiNbO₃ and in proton/deuteron exchanged layers at the surface of LiNbO₃”, *J. Phys.: Condens. Matter* **7**, 6393 (1995).
- [62] A. Grone and S. Kapphan, “Direct OH and OD librational absorption bands in LiNbO₃”, *J. Phys. and Chem. of Solids* **57**, 325 (1996).
- [63] M. Wohlecke and L. Kovacs, “OH[−] ions in oxide crystals”, *Crit. Rev. in Solid State Commun. State and Mater. Sci.* **25**, 1 (2001).
- [64] L. Kovacs, K. Polgar, R. Capelletti, and C. Mora, “Diffusion of hydrogen isotopes in pure and Mg-doped LiNbO₃”, *Phys. Stat. Sol. A* **120**, 97 (1990).

- [65] R. Müller, L. Arizmendi, M. Carrascosa, and J. M. Cabrera, “Determination of H concentration in LiNbO₃ by photorefractive fixing”, *Appl. Phys. Lett.* **60**, 3212 (1992).
- [66] J. L. Ketchum, K. L. Sweeney, L. E. Halliburton, and A. F. Armington, “Vacuum annealing effects in lithium niobate”, *Phys. Lett. A* **94**, 450 (1983).
- [67] K. Buse, S. Breer, K. Peithmann, S. Kapphan, M. Gao, and E. Krätzig, “Origin of thermal fixing in photorefractive lithium niobate crystals”, *Phys. Rev. B* **56**, 1225 (1997).
- [68] G. Panatopoulos, M. Luennemann, K. Buse, and D. Psaltis, “Temperature dependence of absorption in photorefractive iron-doped lithium niobate crystals”, *J. Appl. Phys.* **92**, 793 (2002).
- [69] A. M. Glass, D. Von der Linde, and T. J. Negran, “High-voltage bulk-photovoltaic effect and the photorefractive process in LiNbO₃”, *Appl. Phys. Lett.* **25**, 233 (1974).
- [70] K. Buse, “Light-induced charge transport processes in photorefractive crystals II: Materials”, *Appl. Phys. B* **64**, 391 (1997).
- [71] V. M. Fridkin and B. I. Sturman *The photovoltaic and photorefractive effects in noncentrosymmetric materials*. Gordon and Breach Science Publishers, 1992.
- [72] K. Buse, “Light-induced charge transport process in photorefractive crystals I: Models and experimental methods”, *Appl. Phys. B* **64**, 273 (1997).
- [73] G. T. Niitsu, H. Nagata, and A. C. M. Rodrigues, “Electrical properties along the x and z axes of LiNbO₃ wafers”, *J. Appl. Phys.* **95**, 3116 (2004).
- [74] B. Sturman, M. Aguilar, F. Agulló-López, V. Pruneri, and P. G. Kazansky, “Photorefractive nonlinearity of periodically poled ferroelectrics”, *J. Opt. Soc. Am. B* **14**, 2641 (1997).
- [75] S. Sochava, K. Buse, and E. Krätzig, “Non-steady-state photocurrent technique for the characterization of photorefractive BaTiO₃”, *Opt. Comm.* **98**, 265 (1993).
- [76] U. Dörfler, T. Granzow, T. Woike, M. Wöhlecke, M. Imlau, and R. Pankrath, “Intensity and wavelength dependence of the photoconductivity in Cr-doped Sr_{0.61}Ba_{0.39}Nb₂O₆”, *Euro. Phys. J. B* **38**, 19 (2004).
- [77] L. Kanaev, V. Malinovsky, and B. Sturman, “Investigation of photoinduced scattering in LiNbO₃ crystals”, *Optics Comm.* **34**, 95 (1980).
- [78] M. Ellabban, R. Rupp, and M. Fally, “Reconstruction of parasitic holograms to characterize photorefractive materials”, *Appl. Phys. B* **72**, 635 (2001).

-
- [79] I. Breunig, M. Falk, B. Knabe, R. Sowade, K. Buse, P. Rabiei, and D. H. Jundt, "Second harmonic generation of 2.6 W green light with thermoelectrically oxidized undoped congruent lithium niobate crystals below 100 °C", *Appl. Phys. Lett.* **91**, 221110 (2007).
- [80] N. Iyi, Y. Kitamura, and S. Kimuar, "Defect structure model of MgO-doped LiNbO₃", *J. Solid State Chem.* **118**, 148 (1995).
- [81] Y. Furukawa, K. Kitamura, S. Takekawa, T. Hatanaka, H. Ito, and V. Gopalan, "Non-stoichiometric control of LiNbO₃ and LiTaO₃ in ferroelectric domain engineering for optical devices", *Ferroelectrics* **257**, 235 (1998).
- [82] Y. Furukawa, K. Kitamura, S. Takekawa, K. Niwa, Y. Yajima, N. Iyi, I. Mnushkina, P. Guggenheim, and J. M. Martin, "The correlation of MgO-doped near-stoichiometric LiNbO₃ composition to the defect structure", *J. Cryst. Growth* **211**, 230 (2000).
- [83] D. Georgiev, V. P. Gapontsev, A. G. Dronov, M. Y. Vyatkin, A. B. Rulkov, S. V. Popov, and J. R. Taylor, "Watts-level frequency doubling of a narrow line linearly polarized raman fiber laser to 589 nm", *Opt. Express* **13**, 6772 (2005).
- [84] Y. Furukawa, K. Kitamura, S. Takekawa, A. Miyamoto, M. Terao, and N. Suda, "Photorefraction in LiNbO₃ as a function of [Li]/[Nb] and MgO concentrations", *Appl. Phys. Lett.* **77**, 2494 (2000).
- [85] Y. Watanabe, T. Sota, K. Suzuki, N. Iyi, K. Kitamura, and S. Kimura, "Defect structure in LiNbO₃", *J. Phys.: Condens. Matter* **7**, 3627 (1995).
- [86] L. Polgár, L. Kovács, I. Földvári, and I. Cravero, "Spectroscopy and electrical-conductivity investigation of Mg-doped LiNbO₃ single-crystals", *Solid State Comm.* **59**, 375 (1986).
- [87] J. Koppitz, O. F. Schirmer, M. Wöhlecke, A. I. Kuznetsov, and B. C. Grabmaier, "Threshold effects in LiNbO₃:Mg caused by change of electron-lattice coupling", *Ferroelectrics* **92**, 233 (1989).
- [88] B. Faust, H. Müller, and O. F. Schirmer, "Free small polarons in LiNbO₃", *Ferroelectrics* **153**, 297 (1994).
- [89] D. Conradi, C. Merschjann, B. Schoke, M. Imlau, G. Corradi, and K. Polgár, "Influence of Mg doping on the behaviour of polaronic light-induced absorption in LiNbO₃", *Phys. Stat. Sol. RRL* **2**, 284 (2008).

- [90] L. Moretti, M. Iodice, F. G. Della Corte, and I. Rendina, “Temperature dependence of the thermo-optic coefficient of lithium niobate, from 300 to 500 K in the visible and infrared regions”, *J. Appl. Phys.* **98**, 1 (2005).
- [91] W. Koechner *Solid-State Laser Engineering*. Springer, 1999.
- [92] L. E. Myers and W. R. Bosenberg, “Periodically poled lithium niobate and quasi-phase-matched optical parametric oscillators”, *IEEE J. Quantum Electronics* **33**, 1663 (1997).
- [93] J. J. Amodei, W. Phillips, and D. L. Staebler, “Improved electrooptic materials and fixing techniques for holographic recording”, *Appl. Opt.* **11**, 390 (1972).
- [94] D. Zelmon, D. Small, and D. Jundt, “Infrared corrected Sellmeier coefficients for congruently grown lithium niobate and 5 mol. % magnesium oxide-doped lithium niobate”, *J. Opt. Soc. Am. B* **12**, 3319 (1997).
- [95] J. J. Workman and et al. *Applied Spectroscopy*. Academic Press, 1998.
- [96] D. H. Jundt and M. C. C. Kajiyama, “Axial stoichiometry variations in lithium niobate crystals grown from near-congruent melts”, *J. Crystal Growth* **310**, 4280 (2008).
- [97] K. Peithmann, J. Hukriede, K. Buse, and E. Krätzig, “Photorefractive properties of LiNbO₃ crystals doped by copper diffusion”, *Phys. Rev. B* **61**, 4615 (2000).
- [98] A. Feisst and A. Räuber, “The influence of growth parameters and electrical fields on the distribution coefficient of chromium in LiNbO₃”, *J. Crystal Growth* **63**, 337–342 (1983).
- [99] D. Von der Linde, A. M. Glass, and K. F. Rodgers, “Optical storage using refractive index changes induced by two-step excitation”, *J. Appl. Phys.* **47**, 217 (1976).
- [100] Y. Ming, E. Krätzig, and R. Orlowski, “Photorefractive effects in LiNbO₃:Cr induced by two-step excitation”, *Phys. Stat. Sol. A* **92**, 221 (1985).
- [101] J. M. Almeida, G. Boyle, A. P. Leite, R. M. De La Rue, C. N. Ironside, F. Caccavale, P. Chakraborty, and I. Mansour, “Chromium diffusion in lithium niobate for active optical waveguides”, *J. Appl. Phys.* **78**, 2193 (1995).
- [102] M. Falk, T. Woike, and K. Buse, “Charge compensation mechanism for thermo-electric oxidization of lithium niobate crystals”, *J. Appl. Phys.* **102**, 063529 (2007).
- [103] M. Falk, T. Woike, and K. Buse, “Reduction of optical damage in lithium niobate crystals by thermo-electric oxidization”, *Appl. Phys. Lett.* **90**, 251912 (2007).

-
- [104] M. H. Dunn, "Parametric generation of tunable light from continuous-wave to femtosecond pulses", *Science* **286**, 1513 (1999).
- [105] L. E. Myers, R. C. Eckardt, M. M. Fejer, R. L. Byer, W. R. Bosenberg, and J. W. Pierce, "Quasi-phase-matched optical parametric oscillators in bulk periodically poled LiNbO₃", *J. Opt. Soc. Am. B* **12**, 2102 (1995).
- [106] K. M. Haught and J. A. Dowling, "Long-path high-resolution field measurements of absolute transmission in the 3.5- to 4.0- μm atmospheric window", *Opt. Lett.* **1**, 121 (1977).
- [107] S. Du, Y. Kaneda, and M. Yarborough, "Absorption measurement of a 50-mm-long periodically poled lithium niobate optical parametric oscillator pumped at 1064 nm by a Nd:YAG laser", *Laser Physics* **18**, 968 (2008).
- [108] E. De Miguel-Sanz, M. Carrascosa, and L. Arizmendi, "Effect of the oxidation state and hydrogen concentration on the lifetime of thermally fixed holograms in LiNbO₃:Fe", *Phys. Rev. B* **65**, 165101 (2002).
- [109] O. Gayer, Z. Sacks, E. Galun, and A. Arie, "Temperature and wavelength dependent refractive index equations for MgO-doped congruent and stoichiometric LiNbO₃", *Appl. Phys. B* **91**, 343 (2008).
- [110] G. K. Kitaeva, K. A. Kuznetsov, and A. V. Penin, A. N. Shepelev, "Influence of small polarons on the optical properties of MgO:LiNbO₃ crystals", *Phys. Rev. B* **65**, 054304-1 (2002).
- [111] A. L. Alexandrovski, M. M. Fejer, R. P. Route, and R. L. Byer, "Photothermal absorption measurements in optical materials", in *Lasers and Electro-Optics, 2000. (CLEO 2000)*, 320, 2000.
- [112] A. Gröne and S. Kapphan, "Sharp, temperature dependent OH/OD IR-absorption bands in nearly stoichiometric (VTE) LiNbO₃", *J. Phys. Chem. Solids* **56**, 687 (1995).
- [113] K. Lengyel, L. Kovacs, A. Peter, K. Polgar, G. Corradi, A. Baraldi, and R. Capelletti, "Thermal kinetics of OH⁻ ions in LiNbO₃:Mg crystals above the photorefractive threshold", *Appl. Phys. Lett.* **96**, 191907-1 (2010).
- [114] W. W. Clark, G. L. Wood, M. J. Miller, E. J. Sharp, G. J. Salamo, B. Monson, and R. R. Neurgaonkar, "Enhanced photorefractive beam fanning due to internal and external fields", *Appl. Opt.* **29**, 1249 (1990).
- [115] K. Buse, R. Pankrath, and E. Krätzig, "Pyroelectrically induced photorefractive damage in Sr_{0.61}Ba_{0.39}Nb₂O₆:Ce", *Opt. Lett.* **19**, 260 (1994).

- [116] K. Buse and K. H. Ringhofer, “Pyroelectric drive for light-induced charge transport in the photorefractive process”, *Appl. Phys. A.* **57**, 161 (1993).
- [117] K. Buse, “Thermal gratings and pyroelectrically produced charge redistribution in BaTiO₃ and KNbO₃”, *J. Opt. Soc. Am. B* **10**, 1266–1275 (1993).
- [118] M. Luennemann, U. Hartwig, and K. Buse, “Improvements of sensitivity and refractive-index changes in photorefractive iron-doped lithium niobate crystals by application of extremely large external electric fields”, *J. Opt. Soc. Am. B* **20**, 1643 (2003).
- [119] A. A. Zozulya and D. Z. Anderson, “Propagation of an optical beam in a photorefractive medium in the presence of a photogalvanic nonlinearity or an externally applied electric field”, *Phys. Rev. A* **51**, 1520 (1995).
- [120] M. Mitchell and M. Segev, “Self-trapping of incoherent white light”, *Nature* **387**, 880 (1997).
- [121] F. Johann and E. Soergel, “Quantitative measurement of the surface charge density”, *Appl. Phys. Lett.* **95**, 232906 (2009).
- [122] J. Safioui, F. Devaux, and M. Chauvet, “Pyroliton: pyroelectric spatial soliton”, *Opt. Express* **17**, 22209 (2009).
- [123] N. Korneev, D. Mayorga, S. Stepanov, A. Gerwens, K. Buse, and E. Krätzig, “Enhancement of the photorefractive effect by homogeneous pyroelectric fields”, *Appl. Phys. B* **66**, 393 (1998).
- [124] E. Fazio, F. Renzi, R. Rinaldi, M. Bertolotti, M. Chauvet, W. Ramadan, A. Petris, and V. I. Vlad, “Screening-photovoltaic bright solitons in lithium niobate and associated single-mode waveguides”, *Appl. Phys. Lett.* **85**, 2193 (2004).
- [125] M. Taya, M. C. Bashaw, and M. M. Fejer, “Photorefractive effects in periodically poled ferroelectrics”, *Opt. Lett.* **21**, 857 (1996).
- [126] S. Gronenborn, B. Sturman, M. Falk, D. Haertle, and K. Buse, “Ultraslow shock waves of electron density in LiNbO₃ crystals”, *Phys. Rev. Lett.* **101**, 116601–1 (2008).
- [127] C. M. Gómez Sarabia, P. A. Márquez Aguilar, J. J. Sánchez Mondragón, S. Stepanov, and V. Vysloukh, “Dynamics of photoinduced lens formation in a photorefractive Bi₁₂TiO₂₀ crystal under an external dc electric field”, *J. Opt. Soc. Am. B* **13**, 2767 (1996).

-
- [128] M. C. Wengler, U. Heinemeyer, E. Soergel, and K. Buse, "Ultraviolet light-assisted domain inversion in magnesium-doped lithium niobate crystals", *J. Appl. Phys.* **98**, 064104 (2005).
- [129] W. Huafu, S. Guotong, and W. Zhongkang, "Photovoltaic effect in $\text{LiNbO}_3\text{:Mg}$ ", *Phys. Stat. Sol. (a)* **89**, K211 (1985).
- [130] M. Koesters, B. Sturman, D. Haertle, and K. Buse, "Kinetics of photorefractive recording for circular light beams", *Opt. Lett.* **34**, 1036 (2009).
- [131] D. Kip, E. Krätzig, V. Shandarov, and P. Moretti, "Thermally induced self-focusing and optical beam interactions in planar strontium barium niobate waveguides", *Opt. Lett.* **23**, 343 (1998).
- [132] J. S. Pelc, C. Langrock, Q. Zhang, and M. M. Fejer, "Influence of domain disorder on parametric noise in quasi-phase-matched quantum frequency converters.", *Opt. Lett.* **35**, 2804 (2010).
- [133] J. P. Gordon, R. C. C. Leite, R. S. Moore, S. P. S. Porto, and J. R. Whinnery, "Long-transient effects in lasers with inserted liquid samples", *J. Appl. Phys.* **36**, 3 (1965).
- [134] M. Koesters, C. Becher, D. Haertle, B. Sturman, and K. Buse, "Charge transport properties of undoped congruent lithium niobate crystals", *Appl. Phys. B* **97**, 811 (2009).
- [135] B. Cole, L. Goldberg, V. King, and L. Leach, "Influence of UV illumination on the cold temperature operation of a LiNbO_3 Q-switched Nd:YAG laser", *Opt. Express* **18**, 9622 (2010).
- [136] S. Odoulov, T. T., A. Shumelyuk, I. I. Naumova, and T. O. Chaplina, "Photorefractive response of bulk periodically poled $\text{LiNbO}_3\text{Y:Fe}$ at high and low spatial frequencies", *Phys. Rev. Lett.* **84**, 3294 (2000).
- [137] D. S. Hum, R. K. Route, G. D. Miller, V. Kondilenko, A. Alexandrovski, J. Huang, K. Urbanek, R. L. Byer, and M. M. Fejer, "Optical properties and ferroelectric engineering of vapor-transport-equilibrated, near-stoichiometric lithium tantalate for frequency conversion", *J. Appl. Phys.* **101**, 093108 (2007).
- [138] F. Jermann and J. Otten, "Light-induced charge transport in $\text{LiNbO}_3\text{:Fe}$ at high light intensities", *J. Opt. Soc. Am. B* **10**, 2085 (1993).

BIBLIOGRAPHY

Acknowledgements

This thesis would not have been possible without the support and help of many individuals who accompanied me through my doctorate, but even more, who accompanied me through life and to whom I am deeply and sincerely grateful.

First of all I would like to thank my thesis adviser Prof. Dr. Karsten Buse for giving me the opportunity to work in his group and supporting me through all the years including my diploma thesis. He provided a scientific environment which was exceptional. He always helped and guided me in words and deeds, and he was a great mentor to me. I am deeply grateful for the opportunities he gave me, e.g. the research stay at Stanford University.

I am very thankful to Prof. Dr. Martin M. Fejer from Stanford University, USA for giving me the opportunity to join his group in order to conduct the major parts of my experiments for my thesis. He challenged me scientifically like I could never imagine. From him I learnt that it is as important to ask the right questions as it is to answer some. I enjoyed working in his group very much and I had a lot of freedom to develop new thoughts, but there was always his silent guidance which never let me feel lost.

I thank Prof. Dr. Karl Maier for the primary review of my thesis. I also thank PD Dr. Bernard Metsch and Prof. Dr. Werner Mader for the secondary reviews.

Furthermore, I would like to take the opportunity to thank Crystal Technology, Inc. for supporting my research by covering my tuition expenses at Stanford University and providing the lithium niobate crystals for my studies. My sincere gratitude goes to Dr. Dieter Jundt, Dr. Claudia Kajiyama, and Dr. Matthias Falk from Crystal Technology, Inc. who I worked closely together with and who supported my research.

Special thanks go to Dr. Carsten Langrock and Dr. Roger Route from Stanford University who are the heart of the Fejer group, and who always helped me in words and deeds. I am deeply grateful to Chris R. Phillips from the Fejer group with whom I worked closely together on several projects, e.g. the development of the theory on the pyroelectrically-induced photorefractive damage, and he also conducted numerical simulations.

I would also like to thank Dr. Katerina Ioakeimidi who performed the OPO experiments. Special thanks go to Derek Chang from the Fejer group. He has always been a great colleague and he has become a close friend to me. I also enjoyed working together with Jason Pelc, Dr. Joseph Schaar, Prof. Dr. Ashot Markosyan in the Fejer group. Furthermore, I would like to thank Prof. Dr. Robert L. Byer and his group from Stanford University for welcoming me as part of the joint Byer-Fejer group. I am thankful to the entire staff of the E. L. Ginzton Laboratory at Stanford University, especially Vivian Drew, the Fejer group administrator. She always helped me with administrative and visa issues.

I thank the entire Buse group. In particular, I would like to thank Dr. Dominik Maxein and Dr. Michael Kösters who were doctoral students in the Buse group as well. Both were great colleagues and became friends to me. I would also like to thank Dipl. Phys. Anne Zimmermann and Dipl. Phys. Tobias Beckmann. I supervised their diploma thesis in the Buse group, and it was a pleasure to work closely together with them. Special thanks go to Raja Bernard. She was always helpful whenever there was an administrative issue. I thank Prof. Dr. Boris Sturman and PD Dr. Dr. Theo Woike, who were regular visiting scholars in the Buse group, for fruitful discussions.

I am very thankful to the Deutsche Telekom Stiftung that provided a doctoral scholarship. My stay at Stanford University would not have been possible without this exceptional scholarship. Specially thanks go to Christiane Frense-Heck from the Deutsche Telekom Stiftung. She was always very helpful. I also appreciate support of the Bonn-Cologne Graduate School of Physics and Astronomy.

I would like to express my deep sense of gratitude to Tamer Bulut. He has always believed in me and given me support, and I would not have taken the paths I have taken without that. He has never let me down. *Tamer, you will always be a unique friend to me!*

I am deeply grateful to my mother Renate Schwesyg and my father Lothar Schwesyg. They are incredibly strong and they dedicated their life to provide me with the best education and opportunities that I can think of. Their unlimited love and support through all the years has been incredible. *Danke!* I would also like to thank my uncle Volker Hillebrandt and my grandmother Martha Hillebrandt. They always provided me a second home.

Last, but not least, I would like to express my deepest sense of love and gratitude to my spouse Dr. Matthias Falk. He is not only my partner, but also a great mentor. I can truly share everything with him. His scientific and emotional support has significantly contributed to the success of my work. He is incredibly smart, patient, and loving, but more so, he is the most positive person I have ever met. He also initiated my stay at Stanford University, and our joint time in the U.S. was an incredible experience. He accompanies me through all the ups and downs of life and I could not have conducted my thesis without his unlimited support. It is true to say that I am the happiest person on earth to have him in my life. *Matthias, I love you!*

List of publications

Parts of this thesis have been published in publications marked in bold type.

- J. R. Schwesyg, H. A. Eggert, K. Buse, E. Śliwinska, S. Khalil, M. Kaiser, and K. Meerholz, "Fabrication and optical characterization of stable suspensions of iron- or copper-doped lithium niobate nanocrystals in heptane", *Appl. Phys. B* **89**, 15 (2007)
- J. R. Schwesyg, H. A. Eggert, J. A. Adleman, and K. Buse, "Spatially resolved holographic measurement of the thermal diffusivity in liquids", *Appl. Phys. B* **92**, 79 (2008)
- J. R. Schwesyg, T. Beckmann, A. S. Zimmermann, K. Buse, and D. Haertle, "Fabrication and characterization of whispering-gallery-mode resonators made of polymers", *Optics Express* **17**, 2573 (2009)
- **J. R. Schwesyg, C. R. Phillips, K. Ioakeimidi, M. C. C. Kajiyama, M. Falk, D. H. Jundt, K. Buse, M. M. Fejer, "Suppression of mid-infrared light absorption in undoped congruent lithium niobate crystals", *Opt. Lett.* **35**, 1070 (2010)**
- **J. R. Schwesyg, M. C. C. Kajiyama, M. Falk, D. H. Jundt, K. Buse, M. M. Fejer, "Light absorption in undoped congruent and magnesium-doped lithium niobate crystals in the visible wavelength range", *Appl. Phys. B* **100**, 109 (2010)**
- **J. R. Schwesyg, M. Falk, C. R. Phillips, D. H. Jundt, K. Buse, and M. M. Fejer, "Pyroelectrically induced photorefractive damage in magnesium-doped lithium niobate crystals", *submitted to J. Opt. Soc. Am. B***

Conference proceedings:

- J. R. Schwesyg, M. M. Fejer, M. Falk, C. Langrock, R. K. Route, C. R. Phillips, M. C. C. Kajiyama, D. H. Jundt, K. Buse, "Light absorption and pyroelectrically induced optical damage in nominally undoped and magnesium-doped lithium niobate crystals", in *Advances in Optical Materials*, OSA Technical Digest (CD) (Optical Society of America, 2009), paper AWC2
- K. Ioakeimidi, J. R. Schwesyg, C. R. Phillips, K. L. Vodopyanov, and M. M. Fejer, "Singly resonant cw mid-IR optical parametric oscillator pumped by a tunable C-band source for free space coherent optical communications", in *Conference on Lasers and Electro-Optics*, OSA Technical Digest (CD) (Optical Society of America, 2010), paper CThH1
- J. R. Schwesyg, A. Markosyan, M. C. C. Kajiyama, M. Falk, D. H. Jundt, K. Buse, and M. M. Fejer, "Optical loss mechanisms in magnesium-doped lithium niobate crystals in the 300 to 2950 nm wavelength range", in *Advances in Optical Materials*, OSA Technical Digest (CD) (Optical Society of America, 2011), paper AIThE3